Structural defects in CdTe and related materials

Watson, C.C.R.

STRUCTURAL DEFECTS IN CdTe and RELATED MATERIALS

by

C.C.R. Watson

This thesis is presented in canditature for the degree of
Doctor of Philosophy

in the

University of Durham

September 1993

ABSTRACT

This work is concerned with the characterisation and observation of structural defects in bulk crystals of CdTe and $Cd_{0.96}Zn_{0.04}Te$ and epitaxial layers of $Cd_{0.24}Hg_{0.76}Te$, and the validation of appropriate characterisation techniques. The driving force behind this project being the use of $Cd_xHg_{1-x}Te$ as an infra-red detector material.

The cathodoluminescence technique has been shown to be an excellent technique for both the qualitative and quantitative identification of structural defects in bulk CdTe and (Cd,Zn)Te. The temperature dependent CL contrast technique is developed and is used to quantitatively distinguish dislocations and precipitates which are represented by a qualitatively similar contrast in CL micrographs. The contrast variations at both type of defect are discussed, and the temperature dependence of the contrast at dislocations is compared with contrast theories derived for the complementary electron beam induced current (EBIC) technique.

The action of a saturated ferric chloride solution as a defect revealing etch for CdTe has also been investigated. The etch was found to reliably develop pits on a range of crystal orientations including the technologically important $(\bar{1}\bar{1}\bar{1})$B face of both CdTe and $Cd_{0.96}Zn_{0.04}Te$. Direct correlations with CL and infra-red microscopy has shown the etch to successfully reveal twin boundaries, dislocations and precipitates. The etchant is also shown to reliably develop pits in (Cd,Hg)Te epilayers.

The structural quality of boules of CdTe grown by the vertical Bridgman technique with and without the accelerated crucible rotation technique (ACRT) have been assessed by CL microscopy, ferric chloride defect etching and triple axis X-ray diffraction. The use of the ACRT modification is shown to decrease the dislocation and precipitate content, and the mosaic tilt, within CdTe boules. ACRT CdTe is also shown to contain a comparable dislocation density, and a lower precipitate density, to that observed in boules of non-ACRT $Cd_{0.96}Zn_{0.04}Te$. The lowest mosaic tilt however is seen to occur in $Cd_{0.96}Zn_{0.04}Te$.

Dislocation rosettes observed in ACRT CdTe grown from a Cd rich source are shown to be a result of Cd precipitates and the crystal quality of melt grown CdTe is compared with the quality of boules of CdTe grown from the vapour using the 'Durham' technique.

Defect etching and triple axis X-ray studies on epitaxial films of LPE $Cd_{0.24}Hg_{0.76}Te$ have indicated a reduction in the dislocation density with increasing thickness, for layer thicknesses $< 6\mu m$. In thicker regions the film dislocation density is observed to maintain a constant (or background) level, the magnitude of which varies from layer to layer. For growth on CdTe and $Cd_{0.96}Zn_{0.04}Te$ substrates, both containing a similar dislocation density (i.e $< 5 \times 10^4 cm^{-2}$), the constant (thick film) dislocation density is seen to be higher than the dislocation density in the corresponding substrate, with its magnitude being dependent on the lattice misfit in the system. These observations are discussed with reference to Mattthews-Blakeslee, and dislocation half-loop, strain relief mechanisms.

The fall in the dislocation density from the interface value to the constant (thick layer) value is seen to show a good fit to a strain relief model which predicts the depth dependence of dislocation densities within epitaxial films.

DECLARATION

I declare that, with the exception of the triple axis x-ray data which was obtained on my behalf by John Hudson, all the work reported in this thesis was carried out by the candidate. I also declare that none of this work has been previously submitted for any degree and that it is not currently being submitted for any other degree.

Dr. K. Durose
Supervisor

Candidate

ACKNOWLEDGEMENTS

I wish to firstly express my thanks to my supervisor Dr. Ken Durose for his help, encouragement and enthusiasm throughout the course of this project. I even forgive him for showing me the excellent CL image he obtained of sub-grain boundaries in bulk CdTe using the department's new SEM. This was the first CL image obtained in the department for a year, after the sad demise of the Cambridge 180 SEM, and it was shown to me one week before I submitted this thesis. My thanks also go to the rest of the II-VI group for their help throughout my work and especially to Ruth Port who had the unenviable task of sharing an office with me.

I am extremely grateful to Norman Thompson, Chris Pearson and David Pattinson for for their attempts to keep the obviously dying S180 SEM alive for as long as they did. My thanks also go to John Hudson for obtaining the triple axis x-ray data, and to Professor Page and Sarah Hainsworth for allowing and helping me to use the Camscan SEM in the Materials Department of Newcastle University.

I am indebted to my CASE sponsors GEC Marconi Infra-red of Southampton, and especially my industrial supervisor Dr. Eoin O' Keefe, for providing me with samples and allowing me to use their facilities. The collaboration between Durham and Southampton has proved extremely fruitful.

Finally, on a more personal note I wish to thank my wife Lesley for her love, prayers and encouragement, and also my parents for the love and support they have given me during my time at Durham.

This thesis is dedicated to

mum and dad

CONTENTS

CHAPTER ONE	page
Introduction	1
References for Chapter One	5

CHAPTER TWO

Crystal Growth and Structural Defects in CdTe and Related Materials

2.1	Introduction	7
2.2	Crystal Growth and Structural Defects in Bulk CdTe and (Cd,Zn)Te	7
	2.2.1 Growth of CdTe and (Cd,Zn)Te from the Melt	
	2.2.1.1 Bridgman Technique	9
	2.2.1.2 The ACRT Modification to the Bridgman Technique	9
	2.2.1.3 Bridgman Growth under a Cd Overpressure	10
	2.2.2 Growth of CdTe from the Vapour using the 'Durham Technique	11
	2.2.3 Structural Defects in CdTe	13
	2.2.3.1 The Sphalerite Lattice and CdTe	13
	2.2.3.2 Dislocations	13
	2.2.3.3 Sub-grain Boundaries	15
	2.2.3.4 Precipitates	17
	2.2.3.5 Twinning	17
2.3	Growth and Structural Properties of (Cd,Hg)Te	18
	2.3.1 Epitaxial Growth of (Cd,Hg)Te	18
	2.3.1.1 LPE Growth of (Cd,Hg)Te on CdTe and Related Substrates	19
	2.3.1.2 Growth of (Cd,Hg)Te on non-CdTe Based Substrates	21
	2.3.1.3 Comparisons of Growth Strategies for (Cd,Hg)Te Epilayers	22
	2.3.2 Structural Defects in Epitaxial (Cd,Hg)Te	23
	2.3.2.1 Dislocations	23
	2.3.2.2 Twinning	26
	2.3.2.3 Pin-Holes	26
2.4	Fabrication of Infra-Red Detectors	26
References for Chapter Two		28

CHAPTER THREE

Characterisation Techniques

3.1	Introduction	30
3.2	Scanning Electron Microscope Techniques	30
	3.2.1 Cathodoluminescence	31
	3.2.2 EBIC	36
	3.2.3 Cathodoluminescence and EBIC Contrast at a Dislocation	36
	3.2.4 Temperature Dependent EBIC Contrast Theories	38
	3.2.4.1 Wilshaw Model	38
	3.2.4.2 Other Models	40
3.3	Triple Axis X-ray Diffraction	41
3.4	Other Characterisation Techniques	42
3.5	Chemical Polishing and Bevel Etching	42
References for Chapter Three		45

CHAPTER FOUR

Cathodoluminescence Studies of Defects in Bulk CdTe

4.1	Introduction	47
4.2	Previous Cathodoluminescence and EBIC Microscopy of CdTe	47
4.3	Qualitative and Quantitative Analysis of Contrast at Defects in as-grown CdTe	49
	4.3.1 Twin Boundaries	51
	4.3.2 Precipitates	53
	4.3.3 Dislocations	58
4.4	Discussion	62
4.5	Conclusions	68
References for Chapter Four		70

CHAPTER FIVE

Qualification of a Saturated $FeCl_3$ Solution as Defect Etchant for CdTe and (Cd,Zn)Te

5.1	Introduction	72
5.2	Review of Etching Solutions Commonly used for CdTe	72

5.3 The Ferric Chloride Etching Reagent 74
5.4 Results and Discussion 75
5.4.1 Twin Boundaries 75
5.4.2 Precipitates 78
5.4.3 Dislocations 83
5.5 Chemistry of Etching Reaction 87
5.6 Conclusions 88
References for Chapter Five 90

CHAPTER SIX
Structural Defects in Bulk CdTe

6.1 Introduction 91
6.2 Structural Defects in Bridgman Grown CdTe and (Cd,Zn)Te 91
6.2.1 Dislocations and Sub-Grain Boundaries 92
6.2.2 Precipitates 101
6.2.3 Discussion 105
6.3 Vapour grown CdTe 109
6.3.1 Structural defects in CdTe Grown by the 'Durham' Technique 110
6.3.2 Discussion 110
6.4 Conclusions 112
References for Chapter Six 115

CHAPTER SEVEN
Structural Defects in Epitaxial (Cd,Hg)Te

7.1 Introduction 116
7.2 Defect Etching Studies 116
7.3 Triple Axis X-ray Diffraction Studies 121
7.4 EBIC Studies 122
7.5 Discussion 126
7.6 Conclusions 132
References for Chapter Seven 134

CHAPTER EIGHT

Summary of Conclusions 135
References for Chapter Eight 141

CHAPTER ONE

Introduction

Single crystals of CdTe have applications as radiation detectors [1], in research solar cells [2], electro-optic cells and infra-red windows [3,4]. However the the major use of CdTe and related Cd rich alloys is as crystal substrates for the epitaxial growth of the infra-red detector material, $Cd_xHg_{1-x}Te$ [4,5]. The band gaps of CdTe and HgTe are 1.45eV and -0.3eV respectively (at room temperature), and hence by varying the alloy composition in $Cd_xHg_{1-x}Te$, a bandgap range spanning both the 3-5μm and 8-14 μm infra-red atmospheric transmission windows may be obtained. For example, at 77K, $Cd_{0.3}Hg_{0.7}Te$ detects infra-red radiation of wavelength 4.5μm, and $Cd_{0.2}Hg_{0.8}Te$ detects at 12.5μm. Thin films of (Cd,Hg)Te have been grown using Vapour Phase Epitaxy (VPE), Metal Organic Vapour Phase Epitaxy (MOVPE) and Molecular Beam Epitaxy (MBE) [6] on a range of substrates including GaAs, Si and sapphire [7,8,9], however the current standard industrial growth technique [10] is Liquid Phase Epitaxy [6] onto $(\bar{1}\bar{1}\bar{1})$B oriented CdTe or (Cd,Zn)Te substrates [11].

CdTe has three major advantages as a substrate for the epitaxial growth of (Cd,Hg)Te;

1) Small lattice mismatch, ~ 0.3 % for $x \cong 0.3$. If $Cd_{1-y}Zn_yTe$ (where $y \cong 0.04$) is used exact (0.01%)lattice matching may be obtained.
2) Both materials have a similar thermal coefficient of expansion (i.e $4.1 \times 10^{-6} + 3.3 \times 10^{-9}$ T K^{-1} for CdTe and $4.1 \times 10^{-6} + 3.6 \times 10^{-9}$ T K^{-1} for $Cd_{0.25}Hg_{0.75}Te$, where T is the absolute temperature in Kelvins [12]).
3) No foreign impurity atoms are introduced.

Nevertheless CdTe and (Cd,Zn)Te have the major drawback of containing a high density of as-grown extended structural defects, namely grain boundaries, twins, precipitates, dislocations and sub-grain boundaries. These have a detrimental effect on the performance of imaging devices fabricated on (Cd,Hg)Te layers. Substrate defects may induce inhomogenieties in growing layers, and electrically active defects propagating into the layer will introduce non-radiative recombination centres, therefore degrading the opto-electronic properties of the film [13]. This is especially

important in focal plane arrays of diodes [14] where good material homogeniety is required.

The objectives of this project are threefold. Firstly techniques for the comprehensive characterisation of structural defects in CdTe and (Cd,Zn)Te are examined, developed and qualified. This work is centred on CL microscopy and etching with ferric chloride solutions. These methods are used with others to assess the crystal quality of substrates. Finally the influence of CdTe and (Cd,Zn)Te substrate quality on the quality of LPE grown (Cd,Hg)Te epitaxial films is assessed.

The majority of the CdTe and (Cd,Zn)Te substrates examined in this work were provided by GEC Marconi Infra-red of Southampton. These substrates were all grown from the melt using variations to the standard vertical Bridgman technique [15]. For bulk CdTe melt growth the effect of incorporating the accelerated crucible rotation technique (ACRT) [5] into the growth process has been examined. In this modification to the Bridgman technique stirring within the melt may be introduced and optimised, and it is hoped that this will enhance the crystallinity and stoichiometry of the growing crystals. To provide a comparison, the structural quality of boules of non-ACRT CdTe have been examined. Furthermore the structural quality of non-ACRT (Cd,Zn)Te has also been assessed. These were grown with the addition of a separate Cd source to the Bridgman arrangement, hence giving growth under Cd rich conditions. A Cd rich growth process enhances the formation of a stoichiometric melt, which in turn inhibits the nucleation of Te inclusions [16]. As an alternative to melt grown bulk CdTe, substrates grown from the vapour using the 'Durham' technique have also been examined. The vapour growth of CdTe has potential advantages over melt techniques, the most important being a reduction in the required growth temperature [17]. Films of epitaxial (Cd,Hg)Te were also provided by GEC Marconi Infra-red of Southampton, the layers being grown by Liquid Phase Epitaxy (LPE) onto $(\bar{1}\bar{1}\bar{1})$B (Bridgman grown) CdTe or (Cd,Zn)Te. In chapter 2 all these growth techniques are described, common structural defects in bulk and epitaxial material are reviewed and the infra-red detector fabrication process is also summarised.

The crystal assessment techniques employed in this project included scanning electron microscopy, defect etching, double and triple axis triple axis diffraction and infra-red (IR) microscopy. The scanning electron microscope modes used were cathodoluminescence, secondary electron imaging, energy dispersive analysis by x-ray (EDAX) and electron beam induced current (EBIC) microscopy. Of these

techniques the primary ones used were cathodoluminescence microscopy (CL) and defect etching. The characterisation techniques used in this work are described in chapter 3.

The cathodoluminescence microcharacterisation technique provides a versatile, non-destructive, contactless method for examining the influence of extended defects in the opto-electronic properties of semiconductors. As-grown defects may be observed with a resolution of ~1μm and spatially resolved spectral acquisition is also possible [18]. Furthermore all CL studies may be adapted to provide depth resolved and temperature dependent information. In this work the use of temperature dependent CL contrast analysis has been developed, in order to enable the quantitative identification of localised structural defects. The concept of CL contrast at a defect is introduced in chapter 3, and chapter 4 describes the characterisation of extended defects in boules of CdTe using both qualitative and quantitative CL microscopy.

Defect selective chemical etching provides a quick and cheap characterisation technique and several etching solutions have been reported for use on CdTe [19-24]. However few of these etchants have been shown to reproducibly develop pits at the locations of defects on the $(\bar{1}\bar{1}\bar{1})$B orientation, the LPE growth surface for (Cd,Hg)Te. In Chapter 5 the action of a saturated aqueous ferric chloride solution as a defect etchant for CdTe is examined. Particular attention is given to the ability of the etchant in developing pits on the $(\bar{1}\bar{1}\bar{1})$B orientation, and to the correlation between such pits and defects revealed by complementary characterisation techniques, notably CL microscopy and infra-red microscopy.

The use of triple axis X-ray diffraction allows the tilt and lattice dilation components of standard double crystal X-ray rocking curves to be distinguished. This is essential for the meaningful characterisation of alloys and the triple axis X-ray analysis of the (Cd,Hg)Te epilayers examined in this work is described in chapter 7. In chapter 6 the technique is used in conjuncture with CL and ferric chloride etching to assess the structural quality of boules of bulk CdTe and (Cd,Zn)Te.

The occurrence and nature of extended defects in the CdTe and (Cd,Zn)Te substrates examined in this work is described in Chapter 6. The ability of the ACRT modification to enhance the structural quality of melt grown boules is assessed by comparing the dislocation, sub-grain and precipitate content in ACRT CdTe with

non-ACRT CdTe and (Cd,Zn)Te. Comparisons are also made between the crystal quality of CdTe boules grown from the melt and the vapour.

The importance of CdTe as a substrate for (Cd,Hg)Te growth is stressed throughout this thesis and in Chapter 7 the structural quality of epitaxial (Cd,Hg)Te layers grown on both CdTe and (Cd,Zn)Te substrates are examined. The dislocation density in the layers is assessed using both defect selective etching and triple axis X-ray diffraction. By defect etching bevelled samples the threading dislocation density in the epilayers is investigated as a function of distance from the the layer / substrate interface. The relationship between the dislocation density measured in the epilayers and that measured in the corresponding substrate is examined , and the influence of the lattice misfit on the epitaxial threading dislocation density is also considered.

REFERENCES FOR CHAPTER ONE

1. M. Ohmori, Y. Iwase and R. Ohno, Mat. Sci. Eng **B16** (1993) 283.
2. R.W. Miles, M.T. Bhatti, K.M. Hynes, A.E. Baumann and R. Hill, Mat. Sci. Eng. **B16** (1993) 250.
3. F.V. Wald, Rev. Phys. Appl.**12** (1977) 277.
4. K. Zanio, in: Semiconductors and Semimetals Vol. 13 'Cadmium Telluride', (Eds.) R.K. Willardson and A.C. Beer, (Academic Press, New York, 1978).
5. P. Capper, J.E. Harris, E. O'Keefe, C.L. Jones, C.K. Ard, P. Mackett and D. Dutton, Mats. Sci. Eng. **B16** (1993) 29.
6. see for example: J.W. Matthews, (Ed.), Epitaxial Growth Part A, (Academic Press, New York, 1975).
7. J.P. Faurie, R. Sporken, Y.P. Chen, M.D. Lange and S. Sivananthan, Mat. Sci. Eng. **B16** (1993) 51.
8. L.O. Bublac and D.D. Edwall, J. Vac. Sci. Technol. **B9** (1991) 1695.
9. S. Johnston, E. R. Blazejenski, J. Bajaj, J.S. Chen and G. Williams, J. Vac. Sci. Technol. **B9** (1991) 1661.
10. C.F. Freeman, J. Vac. Sci. Technol. **B9** (1991) 1613.
11. P.D. Brown, K. Durose, G.J. Russell and J.Woods, J.Crystal Growth **101** (1990) 211.
12. J. Brice and P. Capper (Eds.), 'Properties of Mercury Cadmium Telluride', (Institution of Electrical Engineers, 1987), p. 11.
13. see for example: T. Yamamoto, Y. Miyamoto and K. Tanikawa, J. Crystal Growth **72** (1985) 270.
14. C.T. Elliott, Proc. Jap. Soc. I.R. Sci.Technol. **1** (1991) 1.
15. see for example: O. Oda, K. Hirata, K.Matsumoto and I. Tsuboya, J. Crystal Growth **71** (1985) 273.
16. P. Rudolph and M. Mühlberg, Mats. Sci. Eng **B16** (1993) 14.
17. K. Durose, A. Turnbull and P.B. Brown, Mats. Sci. Eng. **B16** (1993) 96.
18. B.G. Yacobi and D.B. Holt,' Cathodoluminescence Microscopy of Inorganic Solids', (Plenum, New York, 1990).
19. K. Nakagawa, K. Maeda and S.Takeuchi, Appl. Phys. Lett. **34** (1979) 574.
20. M. Inoue, I. Teramoto and S. Takayanagi, J. Appl. Phys. **33** (1962) 2578.
21. J-S. Chen, United States Patent No. 4,897,152, Etchant for Revealing Dislocations in II - VI compounds, (1990).

22. I. Hähnert and M. Schenk, J. Crystal Growth. **101** (1990) 251.
23. E.L. Polisar, N.M. Boinikh, G.V. Indenbaum, A.V. Vanyukov and V.P. Shastlivin, Izv. Vyshch. Uchebn. Zaved. Fiz. **6** (1988) 81.
24. K.Durose, Ph.D Thesis, University of Durham, 1986.

CHAPTER TWO

Crystal Growth of, and Structural Defects in, CdTe and Related Materials

2.1 Introduction

This chapter gives details of the growth and structural properties of all the materials examined in this work. The growth of substrates from the melt, using modifications to the standard Bridgman technique, and growth from the vapour using the 'Durham' technique are both described. A review of the nature and occurrence of structural defects commonly observed in bulk CdTe is also given. For epitaxial (Cd,Hg)Te, the liquid phase epitaxy (LPE) growth technique is described and, as a comparison with nearly lattice matched epitaxial growth, the use of non-CdTe related, high lattice mismatched, substrates is also examined. As for bulk crystals, a short summary of the structural defects observed in epitaxial films is included. Finally the fabrication of infra-detectors from (Cd,Hg)Te films is briefly discussed.

2.2 Growth of, and Structural Defects in, Bulk CdTe and (Cd,Zn)Te

2.2.1 Growth of CdTe and (Cd,Zn)Te from the Melt

Most of the CdTe and (Cd,Zn)Te boules examined in this work were grown from the melt using growth processes based on the Bridgman technique, and were provided by GEC Marconi Infra-red of Southampton. Bridgman growth, using a vertical configuration, has been used from the earliest days of CdTe development and remains the commonest industrial growth technique [1,2]. The CdTe boules examined in this work were grown at GEC by both the conventional Bridgman technique and the accelerated crucible rotation modification to the Bridgman technique (ACRT) [3], whereas the (Cd,Zn)Te samples were cut from boules grown (under a Cd overpressure) by the Nippon Mining Co. using the Bridgman technique.

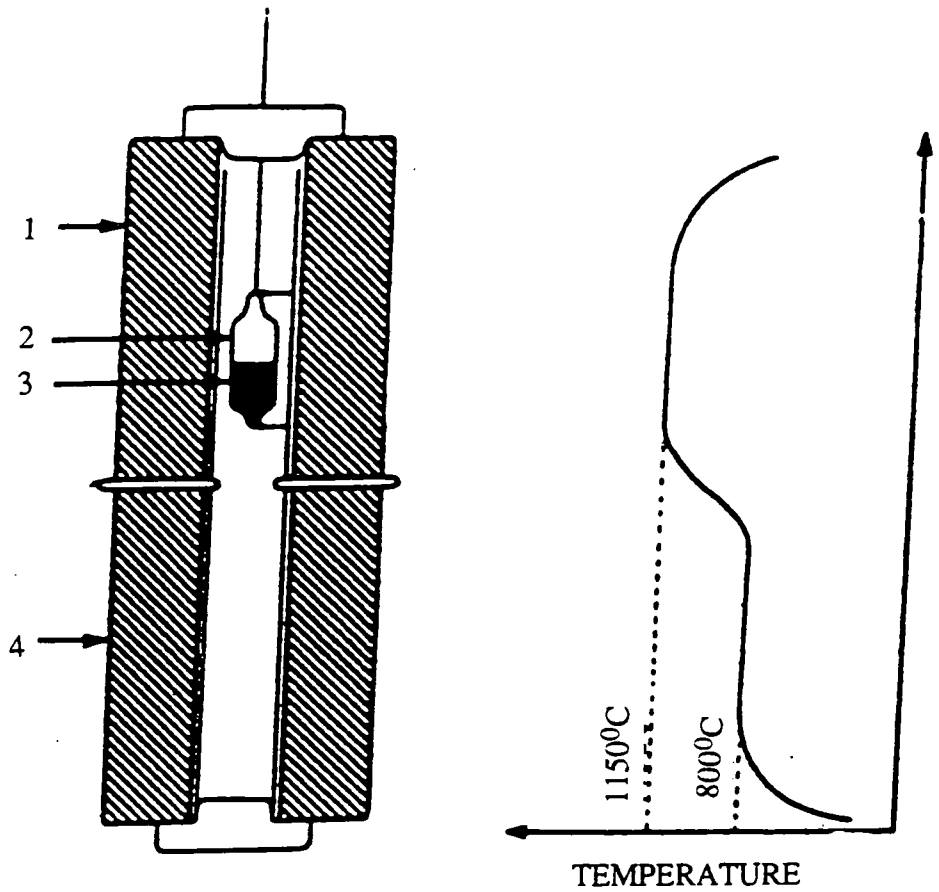

Figure 2.1 Standard Bridgman Growth Arrangement
The typical temperature profile is shown in the figure: (1) upper furnace, (2) carbon coated silica ampoule, (3) CdTe, (4) reflection plate

2.2.1.1 Bridgman Technique

Elemental Cd and Te (plus Zn for (Cd,Zn)Te crystals) are loaded into a silica ampoule, which has been previously coated with carbon to prevent the charges sticking to the ampoule wall. The charge is heated to 820°C, at which temperature Te and Cd react to form CdTe, and held there for 24 hours, to ensure a complete reaction. The temperature of the furnace is then ramped up to above 1150°C (i.e above the maximum melting point of CdTe, 1092°C, and after holding at this temperature for a few hours growth proceeds by lowering the ampoule through a temperature gradient at 1mm h^{-1}. A schematic of a typical growth apparatus and temperature profile are shown in figure 2.1. Growth is performed using microprocessor - controlled equipment and the temperature profile is closely monitored to enable the establishment of a no-mixing temperature profile, in which the temperature increases monotonically. The use of shallow temperature gradients within the furnace has been reported to improve the crystallinity of growing crystals [2].

Growth of the crystals was typically performed from initial stoichiometric weights of Cd and Te, although some crystals were grown from a small Te or Cd excess. This conventional Bridgman method was used to grow some of the CdTe boules examined in this work.

2.2.1.2 The ACRT Modification to the Bridgman Technique

In an attempt to improve the purity, stoichiometry and crystallinity of as-grown boules of CdTe the accelerated crucible rotation technique (ACRT) has been employed at GEC Marconi Infra-red [3]. Originally developed by Wald and Bell [4], the ACRT technique involves the rotation of the growing crystal in such a manner that a maximised mixing of the melt is obtained. A typical rotation sequence is shown in figure 2.2. this sequence being;

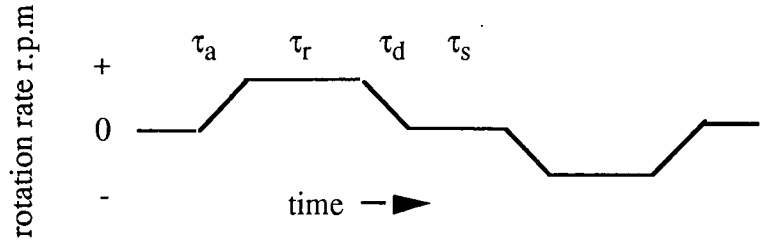

Figure 2.2 ACRT rotation sequence

1. Accelerate (spin -up) the rotation of the ampoule (containing the melt) from rest (for time, τ_a) until a required constant rotation rate is obtained.
2. Rotate the ampoule at this rate for time,τ_r.
3. Decelerate (spin-down) the rotation (time, τ_d) back to zero rpm..
4. Hold rotation rate at zero rpm for the stop time, τ_s
5. Repeat 1-3, but with rotation in opposite direction.

Maximised mixing is achieved, while at the same time maintaining a stable flow of liquid in the growth solution. If the flow becomes unstable, too much mixing may be induced, and a deterioration in crystal quality may ensue [3]. To meet these criteria the ACRT parameters used in the growth of crystals examined in this work were a rotation rate of 4 revmin^{-1} and start / stop times of 50 seconds.

2.2.1.3 Bridgman Growth under a Cd Overpressure

Due to the maximum melting point of CdTe lying on the Te side of the phase diagram [5] (figure 2.3), the evaporation of Cd and Te from a nearly stoichiometric melt occurs incongruently. At 1100°C the vapour composition of the gaseous phase over the Cd-Te melt, is 96% Cd [6]. Therefore the Te_2 partial pressure may be neglected, and the number of Cd atoms evaporating into the gaseous phase is equal to the number of additional Te atoms in the melt. Hence melts obtained from nearly stoichiometric starting conditions are Te rich. Such a situation has consequences for the formation of Te precipitates (section 2.2.3.4) and therefore the formation of Te rich melts is undesirable.

Stoichiometric melts may be obtained by the incorporation of a Cd reservoir into the Bridgman growth apparatus [6,7]. By controlling the temperature of the Cd reservoir a constant Cd overpressure may be obtained above the growing crystal thus inhibiting the evaporation of Cd from the melt and hence allowing the

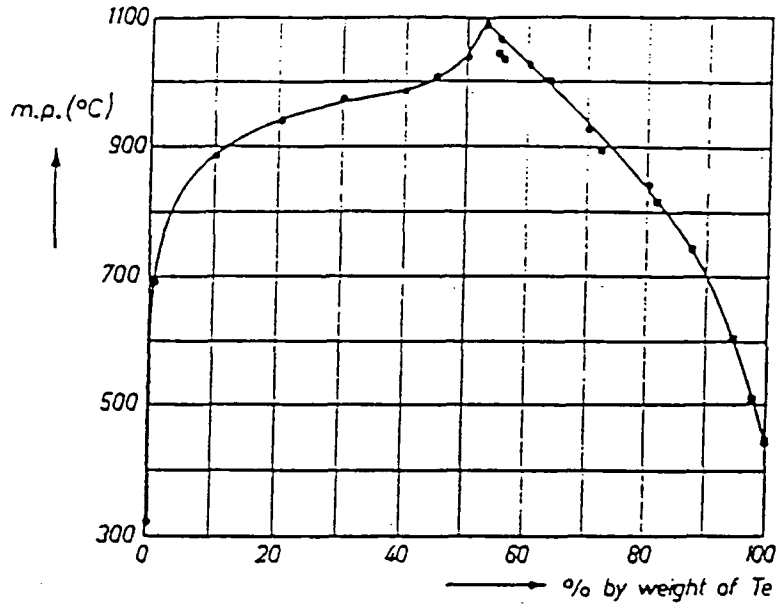

Figure 2.3 Melting Points in the Cd-Te System (see ref. [5])

formation of a stoichiometric melt. The (Cd,Zn)Te boules examined in this work were grown using this technique.

2.2.2 Growth of CdTe from the Vapour by the 'Durham' Technique

To provide a comparison to the structural quality of melt grown material, a boule of CdTe grown from the vapour using the 'Durham' method [8] has also been examined. In this technique a CdTe charge is loaded into the bottom of a silica capsule, and on growth material is transported to the conical growth tip by sublimation in a temperature gradient, as shown in figure 2.4. During growth the temperature difference between the growing crystal and the charge is maintained by pulling the crystal through a temperature gradient. The stoichiometry of the vapour is controlled by use of a Te containing reservoir maintained at a constant temperature. Growth and subsequent cooling was performed over a time scale of 10-14 days.

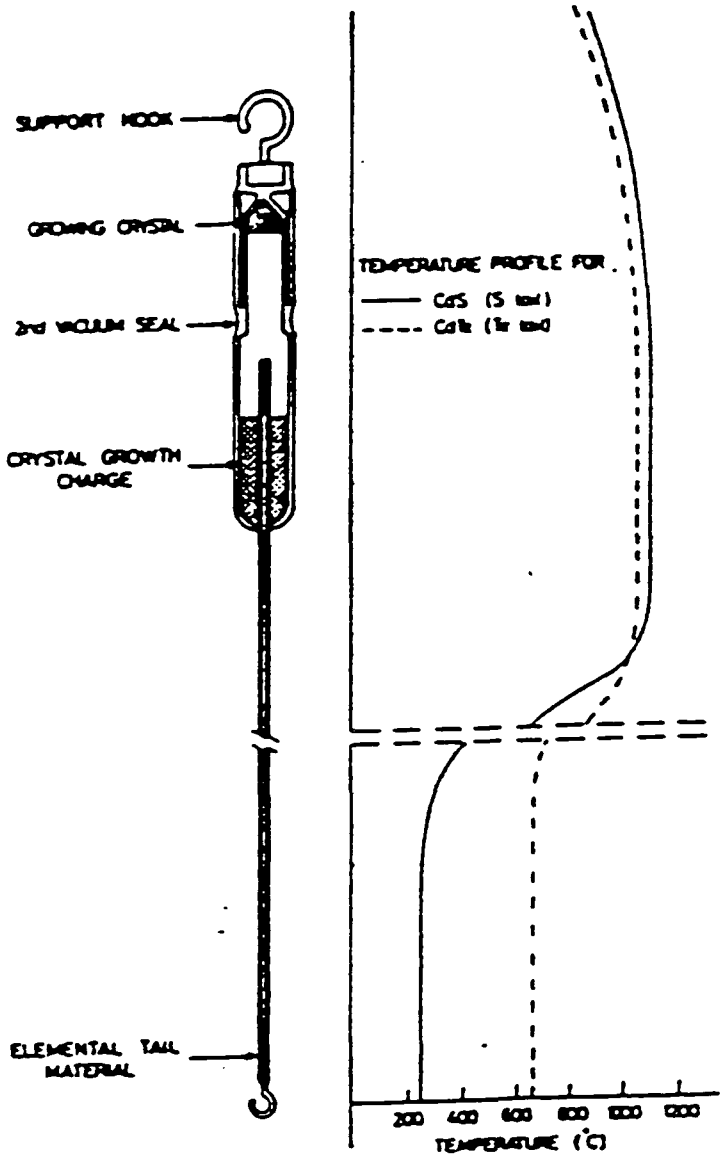

Figure 2.4 'Durham' Vapour Growth technique

2.2.3 Structural Defects in CdTe

In this section a brief review of the occurrence and nature of structural defects encountered in bulk CdTe is provided, the defects covered being dislocations, sub-grain boundaries, precipitates and twins. Firstly however the structure of the CdTe lattice is described.

2.2.3.1 The Sphalerite Lattice and CdTe

CdTe is a II-VI semiconductor with a direct band gap of 1.5eV at 300K, and at room temperature the stable crystalline configuration of CdTe is the sphalerite (or zincblende) lattice. Such a structure consists of two interpenetrating face centred cubic (f.c.c) lattices, one of which comprises of metal atoms and the other, non-metal atoms. The structure may be also described by the packing sequence of {111} planes, with Roman and Greek letters representing metal and non-metal atoms respectively. With this notation the sphalerite lattice is represented by the close packed stacking sequence AαBβCγAα...., (figure 2.5) where atoms α,β,γ are located vertically above A,B,C. The consequence of this sequence is the lack of a centre of symmetry, with the result that (hkl) and $(\bar{h}\bar{k}\bar{l})$ planes are non equivalent. Close packed {111} surfaces bounded by metal (Cd) atoms are referred to as {111}A planes whereas those surfaces terminating with non-metal (Te) atoms are {111}B planes. The non-equivalence of {111} A and B planes has consequences for epitaxial growth. Growth on (111)A and $(\bar{1}\bar{1}\bar{1})$B surfaces gives widely differing results, that on $(\bar{1}\bar{1}\bar{1})$B typically producing films with a higher quality surface morphology compared with films grown on the (111)A orientation [9]. The difference in orientation is also apparent in defect etching experiments, there being few defect revealing etchants reported to reveal defects on $(\bar{1}\bar{1}\bar{1})$B, whereas a number of etching solutions develop etch pits on the (111)A orientation. A full review of defect etching is given in chapter 5.

2.2.3.2 Dislocations

The shortest lattice vector and therefore the most likely Burgers vector for dislocations in materials with the f.c.c structure are of the type a/2<110> [10], where a is the lattice constant of the unit cell. In f.c.c crystals, Burgers vectors of

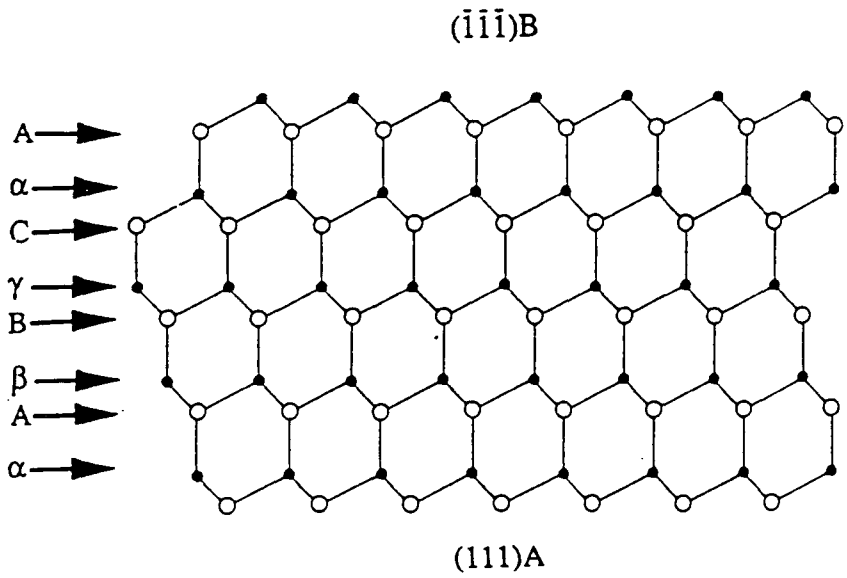

Figure 2.5 Polar surfaces in the Sphalerite Structure

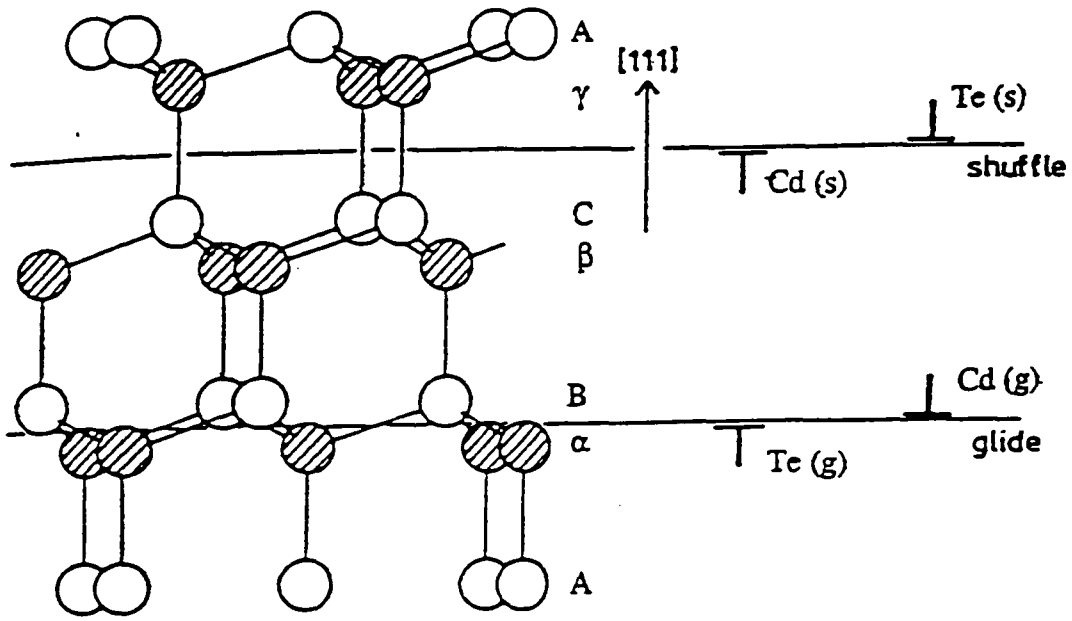

Figure 2.6 Dislocation Types in the Sphalerite Structure (ref 13)

this type lie perpendicular to the dislocation direction (i.e edge dislocations) however in the sphalerite lattice the lowest energy dislocation line is rotated from the a/2<110> Burgers vector by 60°, and hence is referred to as a 60° dislocation [11]. 60° dislocations may dissociate into two partial dislocations with Burgers vectors a/6 <21$\bar{1}$> and a/6 <11$\bar{2}$>, this dissociation being energetically favourable due to the energy of a dislocation being proportional to the square of its Burgers vector [10]. The region bounded by the two partial dislocations is a stacking fault.

Depending on whether the dislocation formation leads to the breaking of bonds between atoms in two narrowly spaced or two widely spaced {111} planes, 60° dislocations may be classed as belonging to the glide (g) or shuffle (s) set respectively [12,13]. Furthermore depending on whether the extra half plane of atoms terminates at a row of metal or non-metal atoms, 60° dislocations in CdTe may be classed as Cd(s), Cd(g) , Te(s) or Te (g). Examples of each are shown in figure 2.6.

Although the commonest dislocation in CdTe is the 60° type other dislocation types, such as edge and screw, are also observed in the material [11]. The presence of high dislocation densities in CdTe is common due to its low critical resolved shear stress (C.R.S.S) , ~ 5MPa at 300K [14], this being the stress required to initiate slip between adjacent crystal planes which is relieved by the formation of dislocations. At near melting point temperatures this value is greatly reduced.

For a more detailed review of dislocations the reader is also referred to the texts of Cottrell [15], Hirth and Lothe [16] and Read [17].

2.2.3.3 Sub-grain Boundaries

If a crystal is plastically bent then dislocations form on a number of parallel slip planes to accommodate the strain. However such dislocations have their lowest energy configuration when they lie one above another [15] and therefore by a process of slip and climb (i.e polygonisation) the dislocations will re-arrange themselves in order to form this stable distribution. In the resultant configuration (figure 2.7) the distance D between adjacent dislocations is defined as $D = b / \theta$ where b is the dislocation Burgers vector and θ is the mis-orientation between adjacent grains. Such tilt boundaries are known as low-angle or sub-grain boundaries.

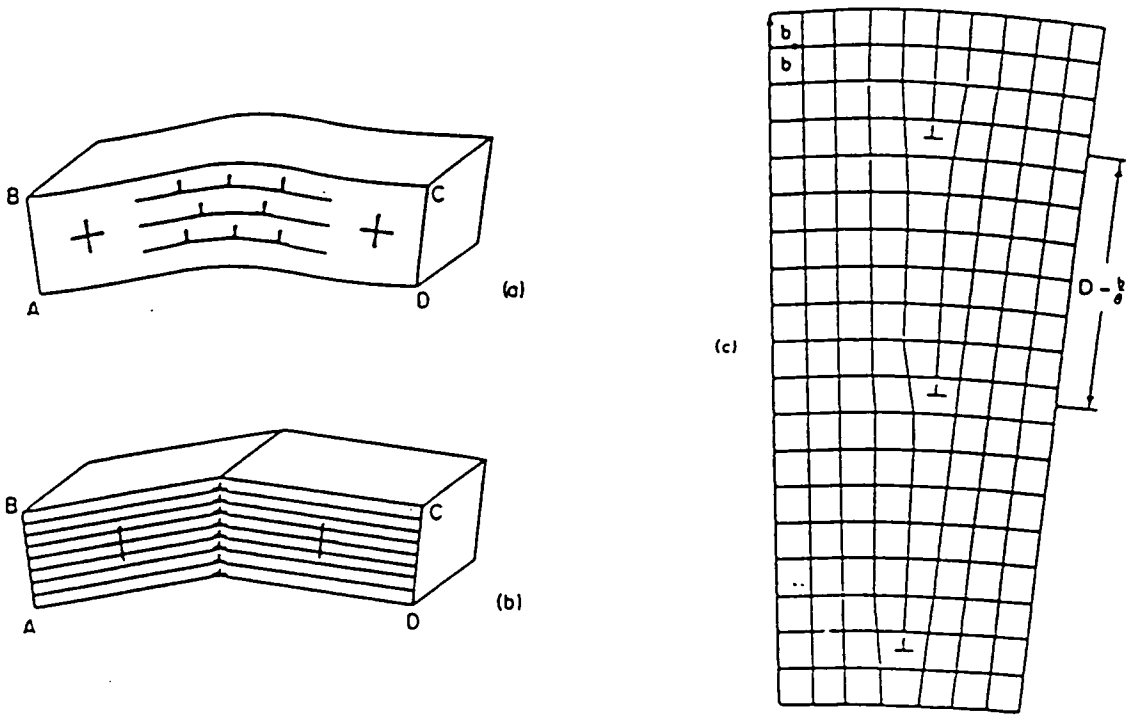

Figure 2.7 Schematic diagram of a Sub-grain Boundary
(a) Deformed crystal with random dislocations, (b) Rearrangement of dislocations to form symmetrical tilt boundary, (c) Schematic of tilt boundary

During growth, the strain required to form dislocations and hence sub-grain boundaries may be induced by either temperature gradients within the melt (i.e thermal strain), the sticking of the melt to the ampoule wall during freezing, or by the proximity of other growth defects such as precipitates and grain boundaries.

2.2.3.4 Precipitates

Solidification from melts (or sublimation from vapour) rich in either Cd or Te will lead to the formation of two kinds of crystal imperfection [6].

1.Morphological instabilities in the growth interface may lead to the capture of Te or Cd droplets, from the boundary layer ahead of the interface, which on freezing form Te or Cd inclusions.

2. Due to their retrograde solid solubility in CdTe [5], both Cd and Te nucleate homogeneously on freezing to form precipitates

Growth by the Bridgman technique, from stoichiometric starting conditions, leads to melts rich in Te (see section 2.2.1.3), and hence crystals grown under these conditions are characterised by a high Te precipitate and inclusion content. Typical sizes for Te inclusions and precipitates are 2-20 μm and 10-30nm respectively [6]. At this point it is important to clarify the terminology used in this thesis. Although correctly the terms inclusions and precipitates refer to different kinds of defects, in this work the terms are used interchangeably and refer to all Te (or Cd) concentrations within the CdTe lattice, regardless of size.

2.2.3.5 Twinning

A twin is characterised by a highly symmetric relationship between atomic sites across a boundary. In crystals with the sphalerite lattice, the twinning plane is {111} and the twinning relationship between twin and matrix may be described as either a 180° rotation in a {111} plane or equivalently as a tilt of 250°32' about a <110> axis [18]. The stacking sequence of planes in a twin in the sphalerite lattice is shown in figure 2.8. The planes at AB and CD are coherent twin planes and the nearest neighbour atomic distances are unchanged across these planes. However the line BC forms an incoherent (or lateral) twin boundary. Across such planes the twin and matrix lattices do not fit exactly, and consequently a considerable local atomic misfit is introduced. Durose [18,19], has predicted the atomic bonding at lateral and coherent twin boundaries in CdTe by use of coincidence site lattice models. The

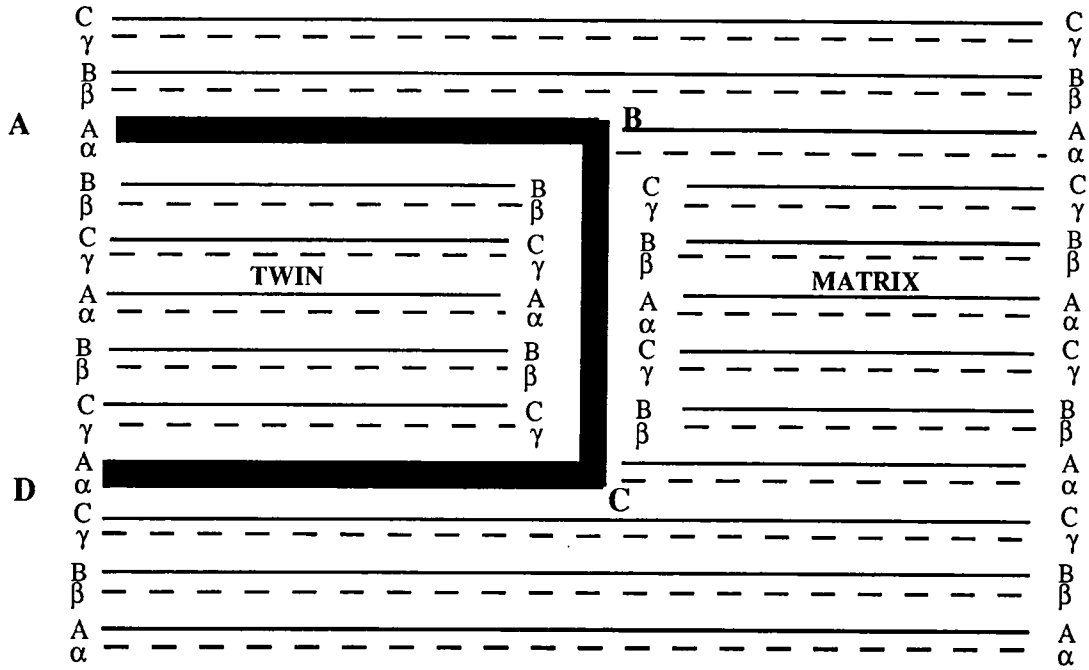

Figure 2.8 Stacking sequence at a First Order Twin Boundary. AB and CD are coherent boundaries, BC is an incoherent lateral twin boundary.

boundaries in figure 2.8 are of a first order nature however boundaries delineating the intersection of two or more twin lamellae are classed as higher (eg 2nd order and above) order twin boundaries. Although twinning can result from deformation in metals, the preferred mechanism in semiconductors is slip. Hence twinning is prevalent in some semiconductors as a growth defect. Indeed attempts to induce deformation twinning in CdTe, by Vere [20], have failed. Growth twins have an especially low energy in CdTe on account of its high ionicity (74% [21]) and hence a low stacking fault energy [20].

2.3 Growth and Structural Properties of Epitaxial (Cd,Hg)Te

2.3.1 Epitaxial Growth of (Cd,Hg)Te

In this section the epitaxial growth of (Cd,Hg)Te is examined. At GEC growth is performed by use of the Liquid Phase Epitaxy (LPE) technique on nearly lattice matched CdTe and (Cd,Zn)Te substrates [22]. LPE growth is preferred, in production, to other epitaxial techniques such as Molecular Beam Epitaxy (MBE) and Molecular Organic Chemical Vapour Deposition (MOCVD) because of the high purity, compositional uniformity and compositional controlability obtainable in LPE

films [23]. (The MBE and MOCVD growth techniques are described by Matthews [24]).

In addition to LPE growth on nearly lattice matched substrates, the epitaxy of (Cd,Hg)Te by MBE and MOCVD onto mismatched foreign substrates is also briefly reviewed.

2.3.1.1 LPE Growth of (Cd,Hg)Te on CdTe and Related Substrates

The experimental apparatus used for LPE growth is shown in figure 2.9. It consists of a two zone reactor, with a low temperature region containing a pure Hg bath which is used as a Hg source, and a high temperature region containing a graphite boat. Growth is performed within a silica tube with stainless steel end plates sealed with 'O' rings. The (Cd,Hg)Te charge is prepared by loading calculated weights of CdTe, HgTe and Te into the growth boat, which is then sealed under a hydrogen atmosphere and heated at 496°C until equilibrium is obtained, at which point the boat is cooled to produce a solid charge. A $(\bar{1}\bar{1}\bar{1})$B CdTe or (Cd,Zn)Te substrate is then placed into a well drilled into the growth boat which is isolated from the previously prepared charge by a graphite slider. The graphite boat containing both substrate and charge is then loaded into the furnace. To prevent Hg loss from the charge a H_2 stream is passed over the Hg reservoir, held at 250-260°C in order to provide a Hg overpressure. The furnace temperature is increased to 496°C (i.e the temperature at which the charge was prepared), at which point the slider is removed, the substrate comes into contact with the molten charge and growth is performed by cooling the boat and Hg reservoir at a rate of 7.5-15°C h^{-1}.

In order to compare LPE grown (Cd,Hg)Te with material grown using other techniques, typical film dislocation densities and X-ray rocking curve widths of LPE (Cd,Hg)Te films reported in the literature are now given. For LPE growth on CdTe related substrates, epilayer dislocation densities of 10^5 cm^{-2} and lowest rocking curve widths of ~20 arcseconds have been reported [23,25]. Epitaxial films of (Cd,Hg)Te grown on lattice matched (Cd,Zn)Te substrates by different epitaxial techniques have been reported to to be characterised by similar dislocation densities and FWHM's, e.g MBE films on (Cd,Zn)Te have been reported to contain a dislocation density of 1.3 x 10^5 cm^{-2} and have a FWHM of 34" [26] whereas a minimum FWHM of 24" has been reported for MOCVD growth of (Cd,Hg)Te [27].

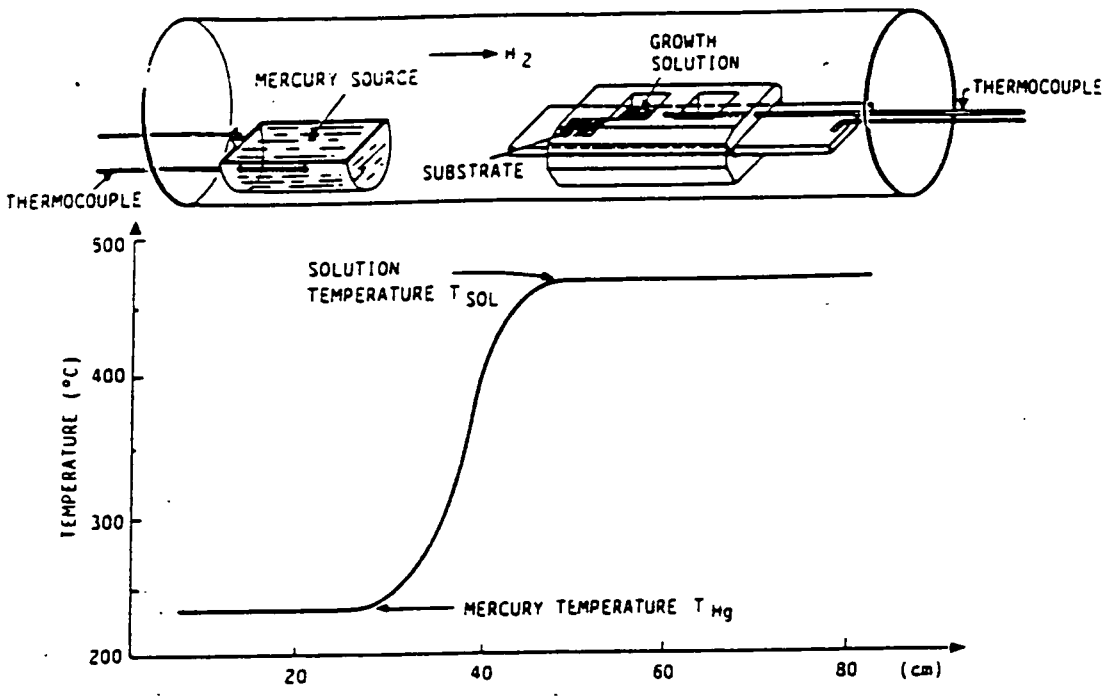

Figure 2.9 LPE Growth Apparatus

Electrical measurements on the (Cd,Hg)Te layers grown at GEC revealed the films to be p-type [3], this being accounted for by the occurrence of Hg vacancies within the material.

2.3.1.2 Growth of (Cd,Hg)Te on non- CdTe Based Substrates

Although LPE growth onto closely latticed matched CdTe related substrates remains the benchmark growth technique [28] for (Cd,Hg)Te, such a growth technique has inherent limitations due to the difficulty in growing large area high quality CdTe substrates. Large area substrates of GaAs and Si with a high crystal quality however are readily available, and at fraction of the cost of CdTe (0.5% and 2% of the cost per unit area of CdTe respectively [29]), GaAs and Si also having the advantage of being less fragile and easier to process than CdTe. Furthermore the use of silicon substrates could enable the direct coupling of the infra-red detector with electronic circuitry (i.e electronic displays), thus enabling the production of large arrays with fully integrated device fabrication. Hence the heteroepitaxy of (Cd,Hg)Te onto GaAs, Si [29] and composite GaAs/Si [30] substrates has been widely reported in the literature, growth also being reported on sapphire [31]. The epitaxy of (Cd,Hg)Te onto such substrates usually proceeds by growth onto a buffer layer of CdTe, epitaxially grown on to the substrate. Such epitaxial growth of (Cd,Hg)Te and CdTe is typically performed using the MBE and MOCVD techniques. CdTe however has a lattice mismatch of 14.5% and 19% with GaAs and Si respectively, thus the epitaxy of CdTe and hence (Cd,Hg)Te onto these substrates is difficult [29].

For MBE growth on GaAs the highest quality films of CdTe have been obtained on the CdTe(211) / GaAs (211) and CdTe (331) / GaAs (211) orientations [32-34]. CdTe films of this orientation are twin free and give typical double crystal X-ray diffraction (DCXRD) full width half maximum (FWHM) values of 90 and 80 arcseconds respectively.The subsequent MBE growth of (Cd,Hg)Te has been reported to produce films containing an average dislocation density of $5 \times 10^6 - 10^7$ cm^{-2} [32]. MOCVD growth of (Cd,Hg)Te via a CdTe buffer is typically performed on (100) GaAs substrates misoriented 2^o in the <110> direction [35,36]. Growth on a misoriented substrate eliminates the severe twinning observed in (111) oriented CdTe films [29]. On such a CdTe / GaAs substrate MOCVD films of (Cd,Hg)Te have been reported with a dislocation density of 2×10^6 cm^{-2} and a DCXRD FWHM of 72 arcseconds [37]. Similar growth on GaAs /

Si substrates [37] has produced (Cd,Hg)Te films with a dislocation density in the range mid 10^6 - 10^7 cm^{-2}.

By careful control of the substrate orientation the large (19%) lattice mismatch between Si and CdTe may be reduced [29,38]. If a substrate orientation of Si (100) is employed, epitaxial CdTe grows with a (111) orientation and the lattice mismatch along the CdTe [$\bar{2}11$] axis is reduced to 3.4%. MBE growth of (Cd,Hg)Te on CdTe (111) / Si (100) has resulted in films with a DCXRD FWHM of 200 arcseconds [38], a slight misorientation of the Si substrate away from Si (100) being reported to help the growth of twin free CdTe layers [29]. Epitaxial CdTe has also been grown by the MOCVD technique onto Si (100) substrates, the lowest reported DCXRD FWHM of 400 arcseconds was reported in CdTe films grown with an increased VI : II ratio [39]. Such an increase in the ratio had the effect of rotating the CdTe epilayer by 30^o about its [111] axis, so reducing the lattice mismatch to 3.4% in the [$11\bar{2}$] direction.

2.3.1.3 Comparison of Growth Strategies for (Cd,Hg)Te Epilayers

Although MBE and MOCVD epitaxial growth on GaAs and Si enables the growth of large areas of CdTe and hence (Cd,Hg)Te films, the quality of these films is generally inferior to that of LPE (Cd,Hg)Te grown on latticed matched substrates. Typical values of dislocation densities of mid 10^6 - 10^7 cm^{-2} for the (Cd,Hg)Te / CdTe / GaAs system (few dislocation densities have been reported for (Cd,Hg)Te / CdTe /Si) and lowest double crystal rocking curve FWHM's of 70" and 200" for (Cd,Hg)Te grown on GaAs and Si respectively, compare unfavourably with results reported in nearly lattice matched systems. The LPE growth of (Cd,Hg)Te films on CdTe based substrates resulted in typical dislocation densities of ~$10^5 cm^{-2}$ and FWHM's of 20-50". It is also of note that similar dislocation densities and FWHM's have been reported for (Cd,Hg)Te films grown by both the MBE and MOCVD techniques on lattice matched (Cd,Zn)Te substrates. The structural quality of LPE films examined in this work is discussed in Chapter 7 and a detailed description of defect types common in (Cd,Hg)Te epilayers follows in the next section.

2.3.2 Structural Defects in Epitaxial (Cd,Hg)Te

In this section crystal defects and imperfections in epitaxial films are briefly described, the formation of dislocations, twins and pinholes being discussed. A full review of structural defects in epitaxial films is given by Matthews [40].

2.3.2.1 Dislocations

Dislocations in epitaxial films are usually classed as having either a misfit or threading nature. Misfit dislocations lie parallel to the interface and are a result of the lattice mismatch at film / substrate interfaces, whereas threading dislocations propagate through epitaxial layers and are formed by either the propagation of a dislocation from the substrate into the layer, or by the creation of dislocation half loops within the films [41].

Misfit dislocations are formed due to a breakdown in the coherency of the lattice parameter (a) at the substrate - layer interface. The resulting tensile or compressive strain in the film is relieved by the nucleation of misfit dislocations. The formation of misfit dislocations is energetically favourable when the critical film thickness of a system (h_c) is reached, where h_c is defined by,

$$h_c = \frac{b}{2\pi f} \frac{(1 - \upsilon \cos^2\alpha)}{(1 + \upsilon) \cos \lambda} \ln \left[\frac{h_c}{b} + 1 \right] \qquad [41]$$

where υ is the poisson ratio, λ is the angle between the slip direction and that direction in the film plane which is perpendicular to the line of the intersection of the slip plane, α is the angle between the dislocation line and its Burgers vector, b is the Burgers vector of the dislocation and f is the misfit. The misfit at an interface (f) is shared between interfacial dislocations (δ) and residual strain within the layer (ε), thus $f = \delta + \varepsilon$. Interfacial dislocations are produced by either the turning over of threading dislocations propagating from the substrate so that a segment of the dislocation lies in the plane of the interface (i.e Matthews-Blakeslee model [41]), or by the gliding of dislocations, (on {111} planes in the (Cd,Hg)Te / CdTe system), into the layer to produce dislocation loops, which contain resolved Burgers vector components in the interfacial plane (i.e half-loop model [42]). Both types of dislocation are shown in figure 2.10. Dislocations may also arise from the coalescence of islands (discussed later in this section).

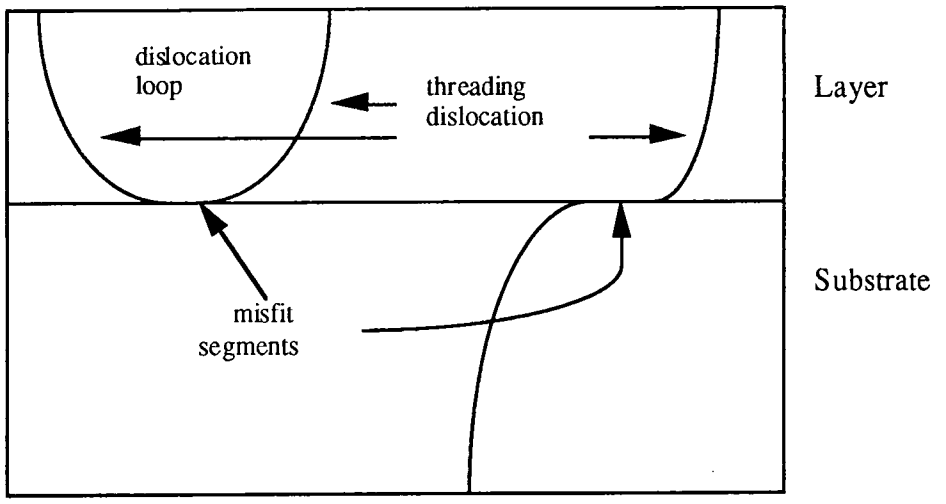

Figure 2.10 Dislocations in Epitaxial Films

The residual strain (δ) is a result of a differential thermal expansion coefficient in the layer or from deviations in the relationship $a_{layer} / a_{substrate} = l / m$ (i.e a deviation from an integer ratio).Tatsuoka [43] has shown experimentally that this residual stress is not homogeneous but is a function of film thickness, the strain falling at increasing distances from the interface. The depth dependence of the residual strain has been used in theories modelling the variation in threading dislocation density in epitaxial films as a function of film thickness [42,43]. Since it is the threading dislocation density which must account for the relief of residual strain it is reasonable to invoke as many threading dislocations as is necessary to yield the observed inhomogeneous residual strain. By considering the resolved component of an inclined threading dislocation, in a plane parallel to the interface, a fraction of the residual strain may be assumed to be removed on moving from one layer to the next. If it is assumed that the driving force behind the annihilation of threading dislocations is the removal of strain, then such a fractional reduction of the strain will implicitly lead to a fractional elimination of dislocations on moving from layer to layer away from the interface. By employing such a theory, Durose [44] predicts a fall in the threading dislocation density at increasing distances from the interface, of the form

$$D(n) = D(1) (1 - Ab_{eff})^n + D_\infty$$

where $D(1)$ is the dislocation density in the first layer, Ab_{eff} is the fractional reduction of the dislocation density, n is the number of layers, and D_∞ is the

dislocation density remaining after the strain has reached a background level. Thus graphs plotting ln (D(n) - D∞) versus n (where n = (a/2)h, and h is the film thickness) are predicted to be linear with gradient ln (1 - Ab_{eff}) and an intercept D(1), i.e the interface dislocation density.

Ayers et al [45] have proposed a different theory to account for the thickness dependence of threading dislocations. In this case threading dislocations with opposing Burgers vectors are assumed to attract one another and coalesce. Upon coalescing a dislocation half-loop, similar to that shown in figure 2.10 is formed, which contains a misfit segment in the plane of the interface. By considering the forces on both the threading dislocations and the misfit segment, an equilibrium half-loop length may be determined, from which the threading dislocation density may be calculated. Using this model Ayers derives a threading dislocation density (Dh) dependency of the form;

$Dh \propto f / h$

where f is the misfit in the system and h is the layer thickness. Thus a 1/ thickness relationship is predicted. It is of note however that this model was derived for thick highly mismatched epitaxial layers and may not be valid for systems containing a small lattice mismatch, i.e systems examined in this work.

The dependence of the threading dislocation density on film thickness therefore makes comparisons between (DCXRD) rocking curve widths of layers of unknown, or different thicknesses, (as reported commonly in the literature) invalid.

Dislocations may also be nucleated in films during epitaxial growth. Possible sources for such nucleation include [40], the accommodation of translational and rotational displacements between islands that are close to epitaxial orientation, the formation of dislocation loops by the aggregation of point defects and the plastic deformation of films, both during growth and subsequent cooling.

2.3.2.2 Twins

As for bulk crystals disruption of the stacking sequence of crystal planes in epitaxial films may lead to the formation of twins, twins being previously reported in MOVPE grown (Cd,Hg)Te layers grown on {111} oriented CdTe substrates [9]. Such twins are of the double positioning type arising from nucleation events. Importantly the incidence of twinning in {111} epitaxial growth by LPE is rare, so making device fabrication on this orientation feasible. Although no double positioning twins occur in LPE (Cd,Hg)Te, due to the difference in the nucleation mechanism compared with MOVPE growth, inclined twin lamellae are observed. In extreme cases lamellae several millimetres wide and extending over the full width of the wafer are encountered. More often however such twins are entirely absent or present in low numbers.

2.3.2.3 Pinholes

Pinholes in LPE epilayers are regions where epitaxial growth has not occurred, thus leaving a void or a hole in the layer. Pinholes are often associated with the presence of precipitates near the substrate surface [46].

2.4 Fabrication of Infra-red Detectors

Thin films of (Cd,Hg)Te have been utilised in the fabrication of two types of infra-red detectors, the older SPRITE detector and new generation staring array detectors. This section briefly describes the manufacture of both, however a more comprehensive review is given by Elliott [47,48].

SPRITE detectors consist of parallel strips of bulk (Cd,Hg)Te (typically 500μm x 63μm in size), along and down which the image under view is scanned. The image is scanned horizontally and vertically by a rotating and 'flapping' mirror respectively. The infra-red image is formed by the production of photogenerated carriers in the (Cd,Hg)Te as photons of infra-red radiation impinge on the detector.i.e the detector is based on the photoconduction principle. The formation of an image depends on matching the scan-rate to the carrier drift velocity.

Staring array detectors however consist of a 2-D focal plane array of photovoltaic (p-n junction) detectors, which are addressed electronically, and do not require

mirrors or scanning. This gives the advantage of the elimination of mechanical scanning which in turn reduces the complexity and size of the system. Furthermore an increase in the integration period is possible in staring arrays compared to scanning detectors therefore giving a longer detection range. Prior to the fabrication of the detector array the (Cd,Hg)Te layer is removed from its (growth) substrate and is mounted onto a silicon integrated circuit, which also contains contact pads. The fabrication process then proceeds by the ion-beam milling of a matrix of holes (typically 128 x 128) into the layer. The holes are typically 5μm in diameter and penetrate through to the silicon contact pads. Type conversion, from p-type to n-type also occurs in the ion beam milling process, hence a p-n junction is formed around each of the holes. The junctions are then connected to the silicon contact pads by the back filling of the holes with a metallic conductor. A schematic of the 'loophole' structure is shown in figure 2.11.

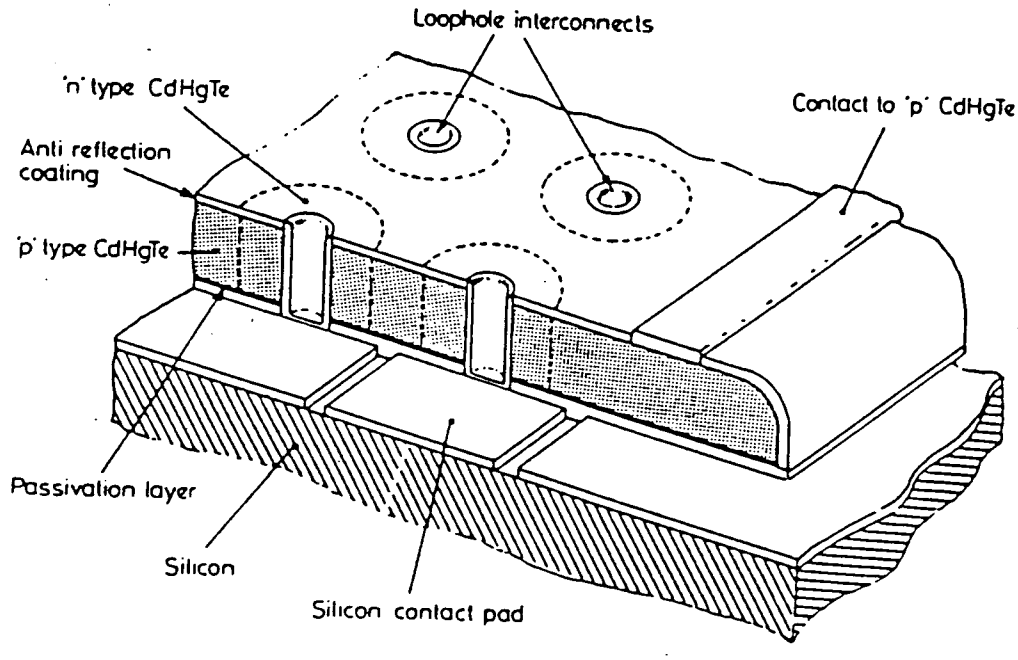

Figure 2.11 Fabrication of p-n Junctions in epitaxial (Cd,Hg)Te (from [48])

REFERENCES FOR CHAPTER TWO

1. C.J. Johnson, S.P.I.E. **1106** (1989) 56.
2. O. Oda, K. Hirata, K.Matsumoto and I. Tsuboya, J. Crystal Growth **71** (1985) 273.
3. P. Capper, J.E. Harris, E. O'Keefe, C.L. Jones, C.K. Ard, P. Mackett and D. Dutton, Mats. Sci. Eng. **B16** (1993) 29.
4. F.V Wald and R.O. Bell, J. Crystal Growth **30** (1975) 29.
5. D. de Nobel, Philips Res. Repts. **14** (1959) 361.
6. P. Rudolph and M. Mühlberg, Mats. Sci. Eng. **B16** (1993) 14.
7. S.L. Bell and S.Sen, J. Vac. Sci. Technol. **A3** (1985) 112.
8. G.J. Russell, N. Thompson and J. Woods, J. Crystal Growth **71** (1985) 671.
9. P.D. Brown, J. E. Hails, G.J. Russell and J. Woods, Appl. Phys. Lett. **50** (1987) 1144.
10. D. Hull, 'Introduction to Dislocations', (Permagon Press (2nd Ed.), 1975).
11. see for example: D.B. Holt, J. Phys. Chem. Solids **23** (1967) 1353.
12. P.J. Van der Wel, J. te Nijenhuis, E.R.H. Van Eck and E. J. Giling, Semicond. Sci. Technol. **7** (1992) A63.
13. Yu-A. Osip'yan, V.F. Petrenko and A.V. Zaretskii, Adv. Phys.**35** (1986) 115.
14. R. Balasubramanian and W.R. Wilcox, Mats. Sci. Eng **B16** (1993) 1.
15. A.H. Cottrell,'Dislocations and Plastic Flow in Crystals', (Clarendon Press, Oxford, 1953).
16. J.P. Hirth and J. Lothe, 'Theory of Dislocations', (McGraw-Hill , London, 1968).
17. W.T. Read,'Dislocations in Crystals', (McGraw-Hill, London, 1953).
18. K. Durose and G.J. Russell, J. Crystal Growth **101** (1990) 246.
19. K. Durose and G.J. Russell in, : Microscopy of Semiconducting Materials 1987, Inst. Phys. Conf. Ser. **87**, (Eds.) A.G. Cullis and P.D. Augustus (Inst. Phys., Bristol, 1987), p.327.
20. A.W. Vere, S. Cole and D.J. Williams, J. Elect. Mat. **12** (1987) 551.
21. K. Zanio , in: Semiconductors and Semimetals, Vol. 13 'Cadmium Telluride', (Eds.) R.K. Willardson and A.C. Beer, (Academic Press, New York, 1978), p. 62.
22. J.C Brice, P. Capper, B.C. Easton, J.L. Page and P.A.C. Whiffen, Semicond. Sci. Technol. **2** (1987) 710.
23. M. Yoshikawa, J. Appl. Phys. **63** (1989) 1533.
24. J.W. Matthews, (Ed.), Epitaxial Growth Part A, (Academic Press, New York,1975).

25. S. Bernardi, J. Crystal Growth **87** (1988) 365.
26. J.M. Arias, S.H. Shin, J.G. Pasko and E.R. Gertner, J. Appl. Phys. **65** (1989) 1747.
27. M.J., Bevan, N.J. Doyle, J. Gregsi and D. Snyder, J. Vac. Sci. Technol. **A8** (1990) 1049.
28. C.F. Freeman, J. Vac. Sci. Technol. **B9** (1991) 1613.
29. J.P. Faurie, R. Sporken, Y.P. Chen, M.D. Lange and S. Sivananthan, Mat. Sci. Eng. **B16** (1993) 51.
30. L.O. Bublac and D.D. Edwall, J. Vac. Sci. Technol. **B9** (1991) 1695.
31. S. Johnston, E. R. Blazejenski, J. Bajaj, J.S. Chen and G. Williams, J. Vac. Sci. Technol. **B9** (1991) 1661.
32. J.M. Arias, R.E. DeWames, S.H. Shin, J.G. Pasko, J.S. Chen and E.R. Gertner, Appl. Phys. Lett. **54** (1989) 1025.
33. M.D. Lange, R. Sporken, K.K. Mahavadi, J.P. Faurie, Y. Nakamura and N. Otsuka, Appl. Phys. Lett. **58** (1991) 1978.
34. A. Tromson-Carli, G. Patriarche, R. Druilke, A. Lusson, Y. Marfaing, R. Triboulet, P.D. Brown and A.W. Brinkman, Mat. Sci. Eng. **B16** (1993) 145.
35. R. Korenstein, P. Hallock and B. MacLeod, J. Vac. Sci. Technol. **B9** (1991) 1630.
36. B.C. Easton, C.D. Maxey, P.A.C. Whiffen, J.A. Roberts, I.G. Gale, F. Grainger and P. Capper, J. Vac. Sci. Technol. **B9** (1991) 1682.
37. D.D Edwall, J. Bajaj and E.R. Gertner, J. Vac. Sci. Technol. **A8** (1990) 1045.
38. R. Sporken, M. D. Lange, J.P Faurie and J. Petruzzello, J. Vac. Sci. Technol. **B9** (1991) 1651.
39. H. Ebe and H. Takigawa, Mat. Sci. Eng. **B16** (1993) 57.
40. J.W. Matthews, (Ed.), Epitaxial Growth Part B, (Academic Press, New York, 1975).
41. J.W. Matthews and A.E. Blakeslee, J. Crystal Growth **27** (1974) 118.
42. E.A. Fitzgerald, G.P. Watson, R.E. Proano, D.G. Ast, P.D. Kirchener, G.D. Pettit and J.M. Woodall, J. Appl. Phys. **65** (1989) 2220.
43. H. Tatsuoka, H. Kuwubara and H. Fujiyasu, Thin Solid Films **59** (1991) 201.
44. K. Duose and H. Tatsuoka, in : Microscopy of Semiconducting Materials 1993, Inst. Phys. Conf. Ser., in press.
45. J.E. Ayers, L.J. Schowalter and S.K. Ghandhi, Mat. Res. Soc. Symp. Proc. **220** (1991) 661.
46. E. O'Keefe, private communication.
47. C.T. Elliott, J. Crystal Growth **77** (1985) 453.
48. C.T. Elliott, Proc. Jap. Soc. I.R. Sci.Technol. **1** (1991) 1.

CHAPTER THREE

Characterisation Techniques

3.1 Introduction

In this chapter the experimental techniques employed in the characterisation of the structural quality of both CdTe (and (Cd,Zn)Te) substrates and (Cd,Hg)Te layers are described. Special attention is drawn to the use of scanning electron microscopy (S.E.M), and the cathodoluminescence (CL) mode is described in depth. The temperature dependent CL contrast analysis technique for the quantitative identification of different types of defect is described, and models predicting the electron beam induced current (EBIC) and CL contrast at an identical dislocation, and the variation in EBIC contrast at dislocations with temperature are briefly reviewed.

Details of the triple axis X-ray diffraction technique are also provided but the use of defect selective etching as a characterisation tool is delayed until chapter 5.

3.2 Scanning Electron Microscope Techniques

In this work secondary electron images have been utilised to examine the nature of etch pits developed by defect etching solutions (chapter 5) and energy dispersive characteristic X-ray analysis (EDAX) has been employed to examine the nature of precipitation (chapters 4 and 6) in CdTe. Details of these techniques may be found in standard electron microscopy texts [1,2]. In order to examine the influence of crystal defects on the electro-optic properties of CdTe the cathodoluminescence and (to a lesser extent) EBIC micro-characterisation techniques have been employed, and these are described in the following sections.

3.2.1 Cathodoluminescence

Cathodoluminescence (CL) is the emission of light from a material as a result of electron bombardment. Luminescence in semiconductors is generally described in terms of radiative recombination of electron-hole pairs. This recombination may be due to transitions between states in the conduction or valence band or band-gap states such as excitons, donors and acceptors. (A book review of CL luminescence transitions, and the technique in general is given by Yacobi and Holt [3]). Examples of transitions between these states are shown in figure 3.1.

Photons are emitted due to the transition of excited electrons from an initial state E_i to a final state E_f, the energy and wavelength of the photon being given by;

$$h\upsilon = hc / \lambda = E_f - E_i$$

For CdTe, with a direct band gap of 1.5eV at room temperature, band gap emission corresponds to luminescence of wavelength 850nm and therefore lies in the infra-red region of the electromagnetic spectrum. On cooling to 77K the band gap increases to 1.6eV and an intrinsic luminescence of 775nm results.

CL analysis performed in an electron microscope falls into one of two categories, microscopy or spectroscopy. In the former a luminescence map of a sample region may be displayed. Electrically active crystal defects act as electron-hole recombination centres, due to either (or both) the presence of dangling bonds (i.e at a dislocation core) or by the decoration of defects by impurities [4,5]. Therefore structural defects are typically revealed in luminescence maps by regions of dark contrast, and hence the CL technique provides an excellent method for analysing the structural quality of opto-electronic materials. The numerical contrast (i.e degree of darkness) of a defect (C) is defined by the relationship;

$$C = \frac{I_0 - I_D}{I_0}$$

where I_0 is the luminescence away from a defect (i.e background luminescence) and I_D is the reduced luminescence at the defect. CL contrast is discussed further in section 3.2.3.

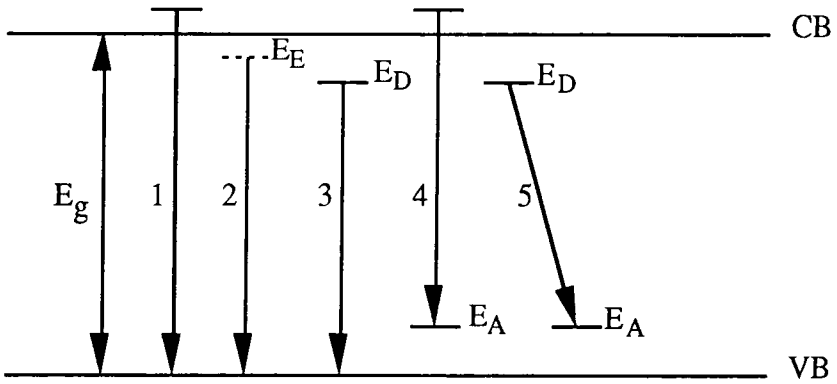

Figure 3.1 Radiative Transitions in a semiconductor.

1. Interband transition, from near bandgap states

2. Exciton decay, from exciton level E_e. Exciton may be free or bound to an impurity. Free exciton recombination is traditionally denoted X; recombination of an exciton bound to a neutral donor is denoted D^0X, recombination to neutral acceptor is denoted A^0X and excitons bound to ionized impurities are denoted D^+X and A^-X.

3,4 and 5. Transitions that start and/or finish on localised impurities (e.g. donors (E_D) and acceptors (E_A)). Process 3, a donor to free hole transition, is denoted A^0h; process 4, a free electron to acceptor transition, is denoted eA^0 and process 5, a donor-acceptor pair recombination, is denoted DAP.

CL spectroscopy involves taking a spectrum of the luminescence wavelengths emitted from a single point within a sample. CL analysis performed in a scanning electron microscope enables spatially resolved spectra to be obtained, thus giving an advantage over the complementary photoluminescence (PL) technique (PL of CdTe is reviewed briefly in chapter 4). Therefore CL spectra acquisition enables the spatial impurity distribution within a material may be examined. For example, by comparing CL spectra obtained in the vicinity of, and away from, crystal defects, the segregation of impurities to defects may be examined. In this work however no systematic CL spectra studies were performed and the CL results described in this work were all obtained using CL microscopy.

The spatial resolution of the CL technique is affected by the electron beam size, the size of the generation volume and the minority carrier diffusion length. However for high probe currents the incident beam size is generally comparable to that of the generation volume, and as the minority carrier distribution is large only in the vicinity of the generation volume [6] the CL resolution is not significantly influenced by the minority carrier diffusion length of the material under investigation. Hence the spatial resolution in most cases is approximately equal to the size of the generation volume and in most inorganic solids a resolution of ~1μm is obtained [7]. The absolute limit of the spatial resolution however is the wavelength of the emitted luminescence, which for CdTe at 77K corresponds to ~775nm.

CL has the advantages of being both contactless (c.f EBIC, section 3.2.1.2) and versatile. By variation of the energy and hence penetration of the primary electron beam, depth resolved CL is obtainable and by use of a cold stage, temperature dependent microscopy is also possible. An expression for the penetration depth (or range) of an electron beam in semiconductors has been derived by Kanaya and Okayama [8], the range being given by;

$$R_e = (0.0276A/\rho Z^{0.889}) E_b^{1.67} \quad (\mu m)$$

where E_b is the beam voltage in keV, A is the atomic weight in $gmol^{-1}$, ρ is in gcm^{-2} and Z is the atomic number. Using this relationship for CdTe gives penetration depths of 3.65, 2.5 and 1.55μm for beam voltages 25, 20 and 15 keV respectively.

Temperature dependent CL provides a technique for the quantitative identification of crystal defects. By measuring defect and background CL signals, either from linescans across localised defects or by employing a frame store data capture system (in this work both were utilised), the contrast of a defect may be plotted over a range of temperatures, and thus different types of structural defects may be identified by a characteristic temperature dependent contrast graph, i.e defect contrast fingerprinting. This is of special importance in distinguishing between structural defects which are revealed in micrographs by a qualitatively similar CL contrast. Such a technique has been previously reported for EBIC [9] but is as yet unreported for CL. A theoretical expression for the CL contrast at dislocations in semiconductors is discussed in section 3.2.3.

The experimental CL arrangement utilised in this work is shown schematically in figure 3.2. The S.E.M electron beam is focussed through a hole in a parabolic mirror located directly above the sample under investigation. The emitted luminescence is reflected along an optical path and is detected by a photomultiplier tube. The (Hammamatsu) photomultiplier employed in this work has an S1 response (i.e detection range 400 - 1200 nm) and is therefore suitable for detecting luminescence from CdTe and (Cd,Zn)Te samples. However the luminescence emitted from $Cd_xHg_{1-x}Te$ (where x = 0.2 - 0.3) is beyond the range of this detector and hence no CL of (Cd,Hg)Te was performed in the course of this project. By use of an Oxford instruments CL302/1 light collector and an Oxford instruments cold stage (cooled by liquid nitrogen or helium) CL experiments were performed in the range 20-300K. In Durham the CL system was housed in a Cambridge S180 S.E.M. CL analysis was also performed using a Camscan 4-80 microscope in the Materials Department at Newcastle University.

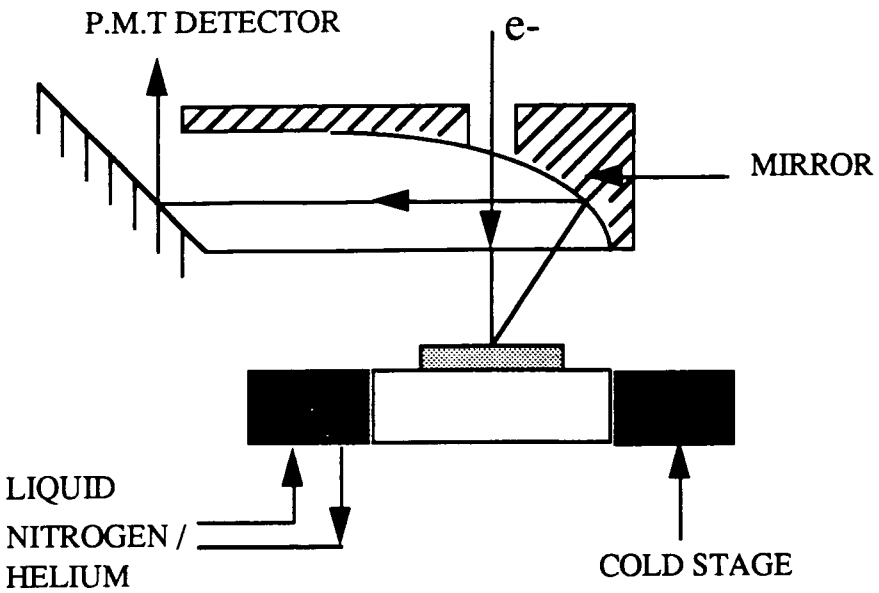

Figure 3.2 CL System

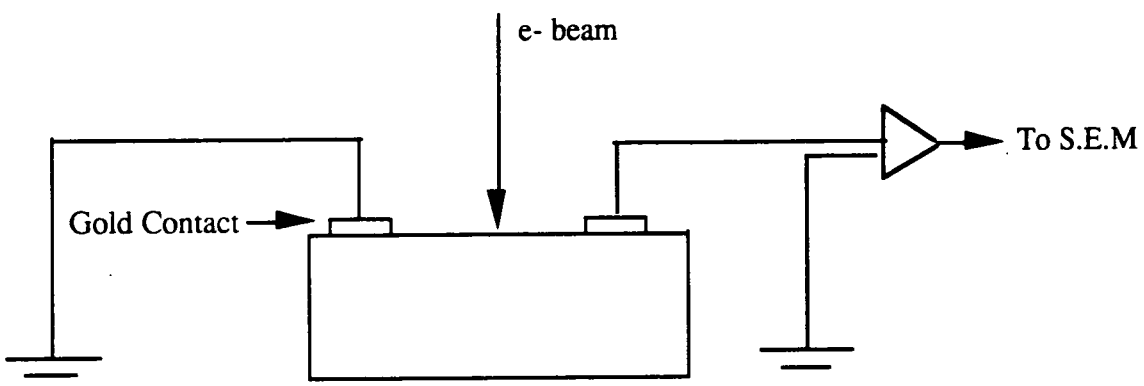

Figure 3.3 Schematic of REBIC Arrangement

3.2.2 EBIC

Electron bombardment induced current (EBIC) involves the separation of electron - hole pairs by an internal electric field (if an external field is applied, β conductivity results [10]). Such electric fields are created at p-n junctions or Schottky barriers, and EBIC is typically performed in materials which include one of these features in their structure. However crystal defects are also associated with regions of energy band bending (see section 3.3), and this may also be utilised to separate carriers and form an EBIC image [11]. In this arrangement the induced current is collected via two ohmic contacts fabricated on the sample surface, as shown in figure 3.3, and this form of the EBIC technique is usually referred to as Remote EBIC or REBIC [9]. REBIC has the advantage of not requiring the fabrication of a contact over the entire semiconductor surface (c.f Schottky barrier fabrication) so enabling simultaneous EBIC / CL investigations to be performed. Such an arrangement was utilised in the present work. Gold ohmic contacts were produced by the evaporation of $AuCl_3$ solution droplets from the sample surfaces. (The contact wires were connected via silver conducting paint). The EBIC investigations were performed using a Cambridge S600 scanning electron microscope and a Matelect ISM5 specimen current amplifier. Unlike CL, which was employed only in the characterisation of substrates, the EBIC technique described above is suitable for both bulk CdTe and epitaxial (Cd,Hg)Te.

3.2.3 EBIC and CL Contrast at a Dislocation

The EBIC contrast at dislocations in semiconductors has been modelled by Donolato [12-14]. Donolato considers a localised dislocation to be represented by a volume F, and characterised by a minority carrier lifetime τ', where $\tau' < \tau$ and τ is the minority carrier lifetime in the absence of a defect. By initially considering the diffusion (or continuity) equation which describes the relationship between the electron-hole generation function and the excess minority carrier concentration, the EBIC contrast at a dislocation in a semiconductor is shown to be;

$$C_{EBIC} = \frac{\gamma}{I_0} \int_F p_0(\underline{r}) \exp\left(\frac{-Z}{L}\right) dV \qquad (3.1)$$

where I_0 is the EBIC signal away from the defect, $p_0(r)$ is the excess minority carrier concentration, Z is the depth of the defect, L is the minority carrier diffusion

length, V is the semiconductor volume and γ is the defect recombination strength per unit volume which is defined by;

$$\gamma = \left(\frac{1}{D}\right)\left[\frac{1}{\tau'} - \frac{1}{\tau}\right]$$

where D is the minority carrier diffusion coefficient.

The CL contrast at an identical dislocation has also been theoretically modelled [15] using the Donolato EBIC model as a basis. For CL however the radiative carrier lifetimes τ_r and $\tau_{r'}$ need also to be included, where $\tau_{r'}$ is the radiative carrier lifetime within the defect ,τ_r is the radiative lifetime away from the defect and $\tau_{r'} < \tau_r$. Using this model the CL contrast at a dislocation may be shown to be;

$$C_{CL} = \frac{\gamma}{I_0 \tau_r} \int_F p_0(\underline{r}) g_{CL} dV - \left(\frac{1}{\tau_{r'}} - \frac{1}{\tau_r}\right) \int_F p(\underline{r}) F(z) dV$$

where

$$g_{CL} = \int_V G(\underline{r},\underline{r}') F(z) dV'$$

and G(r,r) is a Green's function [12] (where G(r,r) is a function of L), p(r) is the excess carrier concentration within the defect and F(z) is the optical losses in the system. Mathematical modelling of the CL contrast [15] has demonstrated that differences in the radiative lifetimes at and away from the defect have little effect on the contrast and thus the CL contrast may be approximated to;

$$C \cong \frac{\gamma}{I_0 \tau_r} \int_F p_0(\underline{r}) g_{CL} dV \qquad (3.2)$$

Thus the equation modelling CL contrast at a dislocation has a similar form to that derived for EBIC, therefore indicating that the CL contrast at a dislocation is primarily a function of the reduced radiative recombination probability, rather than a change in the radiative recombination mechanism [16]. The CL contrast has a functional dependence of the form;

$$C = f(\gamma, I_0, \tau_r, L, g(r), F(z), F) \quad (3.3)$$

i.e the CL contrast at a dislocation is a function of the defect recombination strength, background luminescence, minority carrier radiative lifetime and diffusion length, electron-hole generation function, optical efficiency of the system and the defect geometry.

The similarity in the recombination models for EBIC and CL indicates also that models predicting the EBIC contrast temperature variation are applicable to CL.

3.2.4 Temperature Dependent EBIC Contrast Theories

3.2.4.1 Wilshaw Model

The temperature dependence of the EBIC contrast at dislocations in Si and GaAs has been modelled by Wilshaw et al. [17-20]. In the Wilshaw model (based on an n-type semiconductor, but equally applicable to p-type as grown Bridgman CdTe) a dislocation is assumed to create a number of states within the semiconductor band gap, of which some are initially occupied by electrons and hence the dislocation is negatively charged. This negative charge increases the energy of an electron in the vicinity of the dislocation and a bending up of the conduction and valence band results. The band bending (φ) for a n-type semiconductor is shown in figure 3.4. It is also assumed that the dislocation initially lies below the Fermi level and that dislocation states above the Fermi level remain unoccupied. Wilshaw describes hole capture in the bent band region of the valence band in terms of the defect recombination strength (γ), electron capture in terms of transitions over the potential barrier in the conduction band and furthermore it is assumed that the hole capture rate is always equal to the electron capture rate, i.e a steady state condition. Wilshaw also considers the band bending to vary approximately proportionally to the dislocation charge. Therefore as the temperature increases, the enhanced thermal activation of electrons over the potential barrier increases both the dislocation charge, which has the effect of increasing the band bending, and the hole capture rate. The hole capture rate is assumed to be proportional to γ, and therefore the recombination strength increases nearly linearly with T, i.e; $\gamma \propto T$.

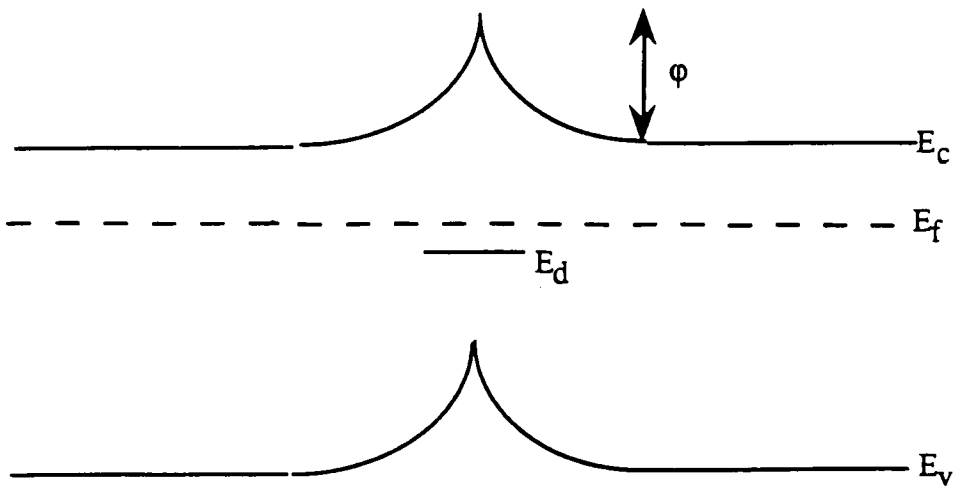

Figure 3.4 Band bending at a dislocation in an n-type semiconductor

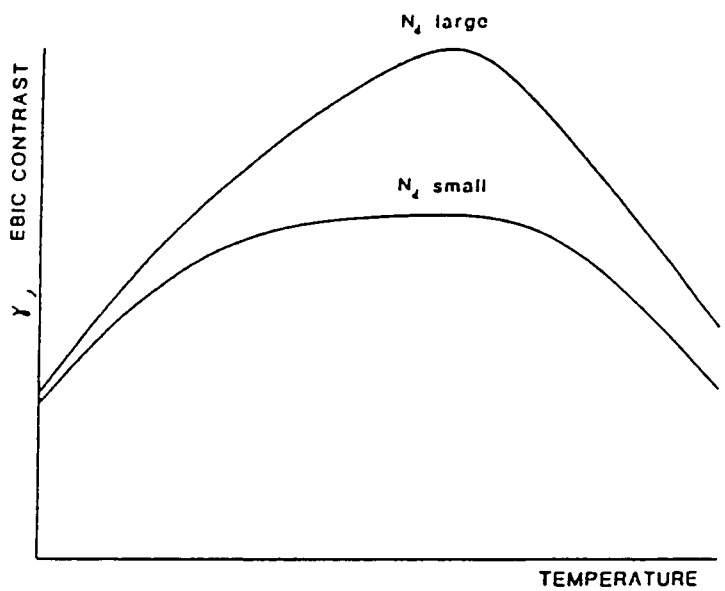

Figure 3.5 Theoretical curves for E.B.I.C Contrast at a Dislocation (from Wilshaw [17-20]). The parameter N_d is the density of dislocation states.

From Donolato's EBIC contrast model [12], where $C \propto \gamma$, Wilshaw predicts that the EBIC contrast has the temperature dependence (at low temperatures) of the form; $C \propto T$, i.e. contrast increases with increasing temperature.

As the charge on the dislocation rises with increasing temperature, Wilshaw describes the situation where the band bending is such that the dislocation level intersects the Fermi level. If at this point, not all the dislocation states are occupied then the dislocation becomes pinned to the Fermi level. As the temperature rises the Fermi level moves towards the centre of the band gap, and hence in order for the dislocation to remain pinned to the Fermi level the dislocation is required to lose charge. This in turn leads to a reduction in the defect recombination strength and hence at high temperatures a fall in contrast is predicted. Theoretical curves for the variation in EBIC contrast with temperature based on Wilshaw's model are shown in figure 3.5.

The Wilshaw model also predicts the dependence of the contrast on the beam current and for a detailed mathematical treatment the reader is referred to refs.[17-20]. The dependence of the contrast on γ, indicates that the Wilshaw model is also applicable to CL results, as the CL contrast at a dislocation has previously been shown to be also a function of γ.

3.2.4.2 Other Contrast Models

A similar band bending description was also used as the basis of an EBIC temperature dependent contrast model by Ourmazd [21]. In Ourmazd's model the hole capture rate and electron capture rate are assumed to be different, this difference being a function of the temperature. Such a differential capture rate will lead to a variation in the size of the band bending, as either a negative or positive charge builds up at the dislocation. However Ourmazd assumes that the band bending is constant and thus the model is inconsistent and therefore flawed [22].

Jakubowicz has described EBIC and CL contrast using a different description [23,24]. A spherical defect of radius a is replaced by an equivalent sphere with radius γa ($0<\gamma<1$), where γ is the defect strength. The contrast is then found to be a non-linear function of γa, thus defects with radii $\gamma(T)a_i$ will correspond to normalised contrasts $C_i(T) / C_i(T_0)$ (i.e contrast normalised to contrast occurring at temperature T_0). However the Jakubowicz model was derived for a point defect

and may therefore not be applicable for a line defect (i.e a dislocation) and also the expression for the contrast becomes singular as the electron beam approaches the defect [14,25].

3.3. Triple Axis X-ray Diffraction

Measurements of full width half maximum (FWHM) of rocking curves obtained using the double crystal X-ray diffraction (DCXRD) technique are commonly utilised in assessing the structural quality of crystals [24]. However in the standard double crystal X-ray diffraction system, the X-ray detector integrates the X-ray scattering over all angles within the aperture and thus the contributions of dilation (change in lattice parameter) or crystal tilt (due to the occurrence of sub-grains for example) to the FWHM width are indistinguishable. In the triple axis mode an analyser crystal is placed before the detector, and is scanned independently of the specimen. This arrangement is shown in figure 3.6. This enables the scattering from various sources to be distinguished and most importantly the scattering due to dilation (or lattice strain) may be distinguished from tilt (or mosaic spread) [25].

In order to measure lattice tilts only the specimen is tilted (i.e $\Delta\varphi = 0$ and $\Delta\psi$ is scanned). If the specimen and analyser are arranged so that the condition (i.e $\lambda = 2d\sin\theta$) is satisfied and the specimen is then rotated, the intensity of the X-rays reaching the analyser will be reduced (i.e the Bragg condition is no longer satisfied). However if the specimen contains regions which are tilted with respect to one another (i.e sub-grains), then as the specimen is tilted different regions will satisfy the Bragg condition and the scattered intensity gives a measure of the distribution of the tilts.

To measure the lattice parameter, the analyser is scanned at twice the rate of the specimen (i.e a θ - 2θ scan). In this regime a specimen with lattice parameter d, is set to diffract initially at the Bragg angle and as the analyser is initially positioned at this angle, intensity reaches the detector. As a θ - 2θ scan proceeds however the intensity reaching the detector will decrease as the Bragg condition for (the initial arrangement) is no longer satisfied (i.e $\lambda \neq 2d\sin\theta$). However as θ changes, regions of the sample with a lattice parameter d' (where $d' \neq d$) may come into a position where the Bragg condition is satisfied, and as the analyser position is at twice the incident angle, intensity reaches the detector. Hence the scatter recorded in a θ-2θ scan gives a measure of the dilation in a crystal.

A full map of the scattering from a specimen may be plotted as a function of a series of separate specimen and analyser positions, to produce a reciprocal space map. The intensity contours in such a map indicate the distance in reciprocal space from the exact Bragg condition. Lattice tilts produce a horizontal (i.e ΔQ_y axis) extension whereas dilation (or strain) gives a distortion in the vertical (ΔQ_z) axis. Therefore the scattering contributions from both tilt and dilation are distinguishable.

In this project triple axis experiments have been utilised in examining the crystal quality of both CdTe and (Cd,Zn)Te substrates, and (Cd,Hg)Te epilayers. The experiments were performed using a Bede spectrometer. On removal of the analyser stage, standard double crystal X-ray diffraction experiments were also performed.

3.4 Other Characterisation Techniques

Other characterisation techniques used in this project include defect etching, Infra - red (IR) microscopy, optical (Nomarski) interference microscopy and surface profiling. Defect etching provides a rapid and inexpensive characterisation technique and is discussed at length in chapter 5. Nomarski microscopy (using a Vickers optical microscope) is very sensitive to surface topography [26] and was used in this work to examine pits developed by etching. Etch rates were calculated by use of a hoverprobe and a Tencor 200 α-step surface profilometer. Infra-red microscopy, with a resolution of ~2μm [27], was used to examine the precipitate distribution within substrates. (Due to the depth of focus of transmission IR microscopes, care is needed in the calculation of areal precipitate densities, i.e. only those precipitates sharply in focus are used in density calculation.)

3.5 Chemical Polishing and Bevel etching

Prior to the application of all the characterisation techniques all the CdTe and (Cd,Zn)Te substrates examined in this work were chemically polished to remove ~10μm of surface damage present after mechanical polishing. Non-contact chemical polishing was performed over a polyurethane pad using a 2% bromine in ethylene glycol solution, followed by complete rinsing in methanol.

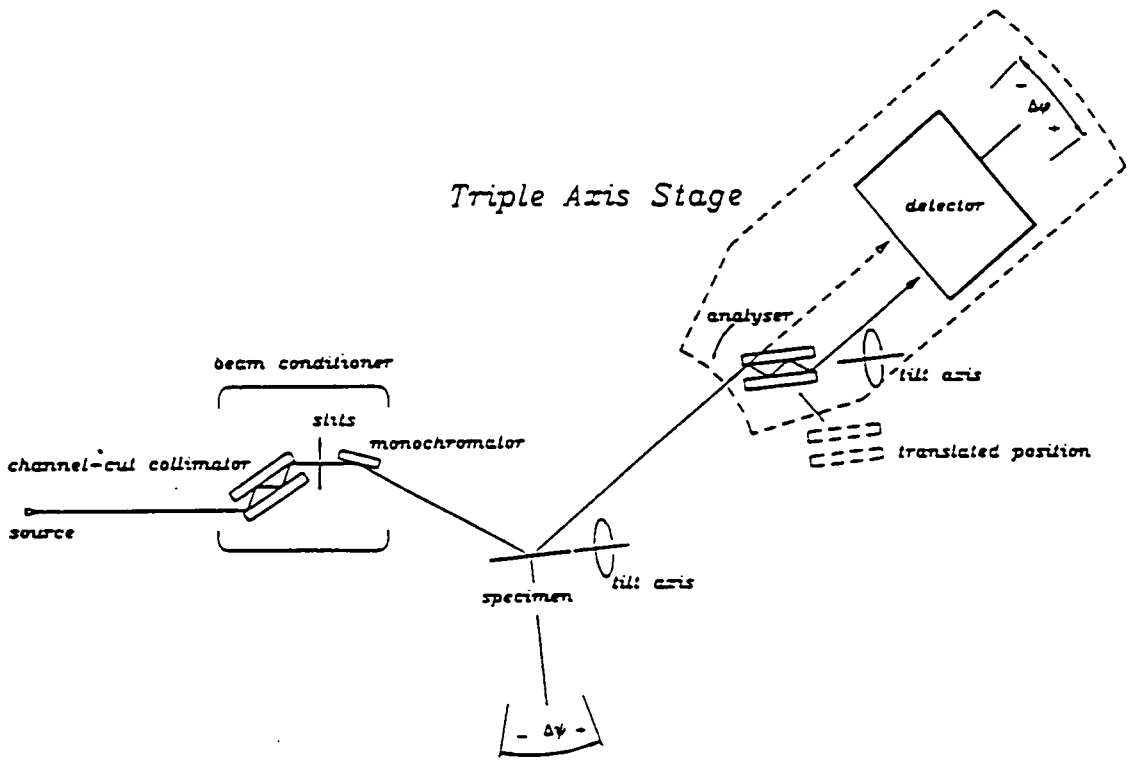

Figure 3.6 Triple Axis X-ray Diffraction Experimental Arrangement (from [27])

In order to obtain bevelled (Cd,Hg)Te layers (chapter 7), an etching solution of 2% bromine in 80% methanol / 20% ethylene glycol was used in conjuncture with the apparatus shown in figure 3.7. A wafer is placed initially in a methanol bath, and by careful opening of valve X, the methanol / etchant interface is slowly allowed to move along the length of the sample. Thus the bottom of the sample in figure 3.7 is etched for a longer period than the top, and if the flow and etch rate of the solution remain constant a linear bevel is obtained. During the etching process valve Y is closed and valves W and Z remain open, and hence valve X limits the flow rate.Valves W and Z close off the sample tube and etch reservoir respectively, and the opening of valve Y enables the rapid positioning of the methanol / etch interface prior to etching. The etching reaction is quenched by flooding the sample tube with methanol.

Using this technique bevels were typically produced in 20μm thick (Cd,Hg)Te layers, over sample lengths of ~20mm. This corresponds to an average bevel angle of ~3'.

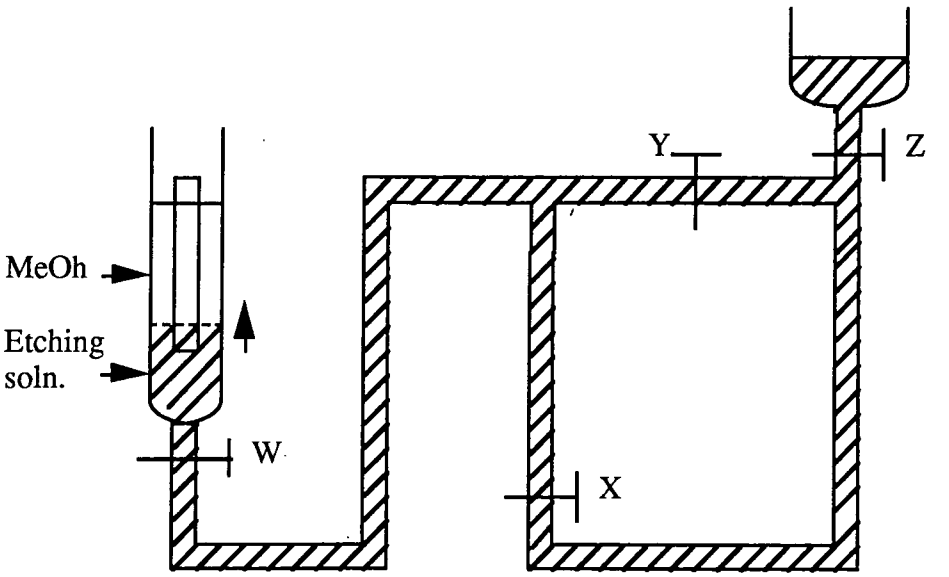

Figure 3.7 Bevelling Apparatus

REFERENCES FOR CHAPTER THREE

1. see for example: H.Bethge and J. Heydenreich (Eds.), 'Electron Microscopy in Solid State Physics', (Elsvier, Amsterdam, 1987).
2. D.B. Holt and D.C. Joy (Eds.), 'SEM Microcharacterization of Semiconductors', (Academic Press, London, 1989).
3. B.G Yacobi and D.B Holt, 'Cathodoluminescence Microscopy of Inorganic Solids', (Plenum, New York, 1990).
4. M. Dupuy, J. de Physique, Colloque **C4** (1983) 277.
5. D.B. Holt, in : 'Point and Extended Defects in Semiconductors', (Eds.) G. Benedek, A. Cavallini and W. Schroter (Plenum, New York, 1989), p. 207.
6. C. Donolato, Optik **52** (1978) 19.
7. B.G. Yacobi and D.B. Holt, as reference 1., p.82.
8. K. Kanaya and S. Okayama, J. Phys. D: Appl. Phys. **5** (1972) 43.
9. G.N Panin and E.B. Yakinov in, : Microscopy of Semiconducting Materials 1991, Inst. Phys. Conf. Ser. **117**, (Eds.) A.G. Cullis and N.J. Long (Inst. Phys., Bristol, 1991).
10. D.B. Holt, M.D. Muir, P.R. Grant and I.M. Boswara, 'Quantitative Scanning Electron Microscopy', (Academic Press, London, 1974).
11. G.J. Russell, M.J. Robertson, B. Vincent and J.Woods, J. Mater. Sci. **15** (1980) 939.
12. C. Donolato, Optik **52** (1978) 19.
13. C. Donolato, in : 'Point and Extrnded Defects in Semiconductors', (Eds.) G. Benedek, A. Cavallini and W. Schroter (Plenum, New York, 1989).
14. C. Donolato, Semicond. Sci. Technol. **7** (1992) 37.
15. L. Paseman and W. Hergert, Izv. Akad. Nauk. SSSR. Ser. Fiz. **51** (1987) 1528.
16. J. Schreiber, W. Hergert and S. Hildebrandt, Appl. Surface Science **50** (1991) 181.
17. P.R. Wilshaw, T.S. Fell and G.R. Booker, in : 'Point and Extrnded Defects in Semiconductors', (Eds.) G. Benedek, A. Cavallini and W. Schroter (Plenum, New York, 1989), p. 243.
18. P.R. Wilshaw and G.R. Booker, in : Microscopy of Semiconducting Materials 1985, Inst. Phys. Conf. Ser.**76**, (Eds.) A.G. Cullis and D.B Holt (Inst. Phys., Bristol, 1985), p.329.

19. P.R. Wilshaw and T.S. Fell, in : Structure and Properties of Dislocations in Semiconductors 1989, Inst. Phys. Conf. Ser.**104**, (Eds.) S.G. Roberts, D.B. Holt and P.R. Wilshaw (Inst. Phys., Bristol, 1989), p. 85.
20. P.R. Wilshaw and G.R. Booker, Izv. Akad. Nauk. SSSR. Ser. Fiz. **51** (1987) 1582.
21. A. Ourmazd, Cryst. Res. Technol. **16** (1981) 137.
22 P.R. Wilshaw, private communication.
23. A. Jakubowicz, J. Appl. Phys. **57** (1985) 1194.
24. A. Jakubowicz, J. Appl. Phys. **59** (1986) 2205.
25. C. Donolato, Izv. Akad. Nauk. SSSR. Ser. Fiz. **51** (1987) 1541.
26. see for example: B.K Tanner and K. Bowen (Eds.), ' Characterisatiom of Crystal defects By X-ray Methods', (Plenum Press, New york, 1980).
27. B.K. Tanner and K. Bowen, J.Crystal Growth **126** (1993) 1.
28. see for example: D.J. Rawlins, 'Light Microscopy', (Bios scientific publishers, Oxford, 1992).
29. see for example: D. Birchon, ' Optical Microscope Techniques', (George Newnes Ltd., 1962).

CHAPTER FOUR

Cathodoluminescence Contrast at Defects in Bulk CdTe Crystals

4.1 Introduction

In this chapter the ability of CL microscopy to qualitatively distinguish between or identify defects in as-grown boules of CdTe and (Cd,Zn)Te is examined and the results are compared with those obtained from complementary techniques, such as EBIC and defect etching. To further characterise defects which are represented in CL micrographs by qualitatively similar contrast, the temperature dependence of the CL contrast at as-grown defects has been measured and employed to quantitatively distinguish different types of defect. By applying models of EBIC contrast which predict the variation in contrast as a function of temperature, the CL contrast mechanism at crystal defects has also been examined.

4.2 Previous CL and EBIC Microscopy of CdTe

CL microscopy has been used to assess the quality of boules of CdTe [1,2] and has also been used to correlate the observation of defects revealed by complementary techniques such as defect etching and X-ray topography [3,4]. However, the use of CL to obtain luminescence spectra at and away from defects in both doped and undoped material, is the most frequently reported application of CL on CdTe (see Refs.[5-7] and bibliographies therein).

Spectral CL (and PL [8,9]) studies of as-grown boules of CdTe have revealed two distinct luminescence peaks, a narrow peak occurring at ~1.58eV and a wider band centred at ~1.4eV. The 1.58 eV peak is attributed to excitonic transitions from near band-edge states [10] whereas the wider band is believed to represent transitions between donor-acceptor pairs [5]. The observation of a weak defect band and a strong band-edge peak is generally thought to indicate good quality CdTe samples [8], on the assumption that point defects, which introduce donors and acceptors into the energy gap, are related to line defects. However, correlations between spectrally filtered CL images and lines in PL spectra [9] have shown sample areas

containing no sub-grain boundaries to exhibit a strong defect band and a weak edge peak luminescence, the opposite being observed at sample areas containing sub-grain boundaries. Thus the relationship between lines observed in CL and PL spectra and CdTe crystal quality is not clear and requires detailed examination; however, no such investigations were performed in the course of the work described in this thesis.

EBIC has also been used to qualitatively assess the structural quality of CdTe boules [10] but unlike CL, quantitative studies of the EBIC contrast observed at extended defects have also been reported [11-13]. For example, by varying the bias voltage on a Schottky diode on CdTe, active and less active dislocations and point-like defects have all been quantitatively identified from the shape of graphs plotting the variation in contrast as a function of E_0, where E_0 is the ratio of penetration depth to depletion region width [12]. 'Active' dislocations are identified by curves with two maxima, a result of a contribution to the contrast from carriers generated in both the bulk and the depletion region, whereas the contrast curves at 'less active' dislocations and 'point like' defects exhibited only one maximum, due to recombination, of only those carriers generated in the depletion region at these defects. The temperature dependence of the EBIC contrast at different extended defects in CdTe has also been examined [13], However as yet no model predicting the variation in contrast at different defects has been reported.

Quantitative models predicting the EBIC contrast at dislocations [14,15] have been used to predict the temperature dependence of the contrast at dislocations in Si and GaAs [15,16,17], and have been tested on experimental EBIC results. These models are described in chapter 3. CL contrast at dislocations has also been modelled [18-20], the results being used to provide techniques for calculating the minority carrier diffusion length in semiconductors [19] and, by comparison with complementary EBIC models, to enable the depth of localised defects to be determined [18]. However, except for the measurement of the temperature dependence of the CL contrast at dislocations in GaAs [21] little has been reported on actual experimental investigations.

In summary, it is apparent that although CL has been used to assess CdTe crystal quality and measure its luminescence spectra, little quantitative analysis of the recombination at defects has been performed. This is true of semiconductors in

general, the quantitative experiments which have been reported being typically performed using EBIC only.

4.3 Qualitative and Quantitative Analysis of CL Contrast at Defects in as-grown CdTe

In this section the ability of CL microscopy both to reveal and to distinguish different types of as-grown crystal defects in boules of CdTe and (Cd,Zn)Te is examined. To enable the qualitative identification of defects, features revealed in CL micrographs were correlated with corresponding features observed by EBIC and etch pits developed by defect etching solutions. The correlation between etching results obtained from a ferric chloride solution and defects imaged by CL is examined in Chapter 5, whereas the comparability of EBIC with CL may be seen by comparing figures 4.1a and 4.1b. These figures show CL and EBIC micrographs obtained at an identical area of a CdTe sample and indicate that both techniques reveal identical defects by a qualitatively similar contrast, e.g as at A.

In order to quantitatively distinguish the characteristic contrast of different defects the temperature dependence of the contrast at defects has been measured, enabling the identification of defects by a characteristic contrast temperature dependence, i.e. contrast 'fingerprinting'. To enable the recombination process responsible for a defect's temperature dependence to be modelled the temperature variation of the background luminescence signal (I_0) has also been examined. The background luminescence (i.e. I_0, the CL signal away from a defect) was observed to fall with increasing temperature as shown in figure 4.2.

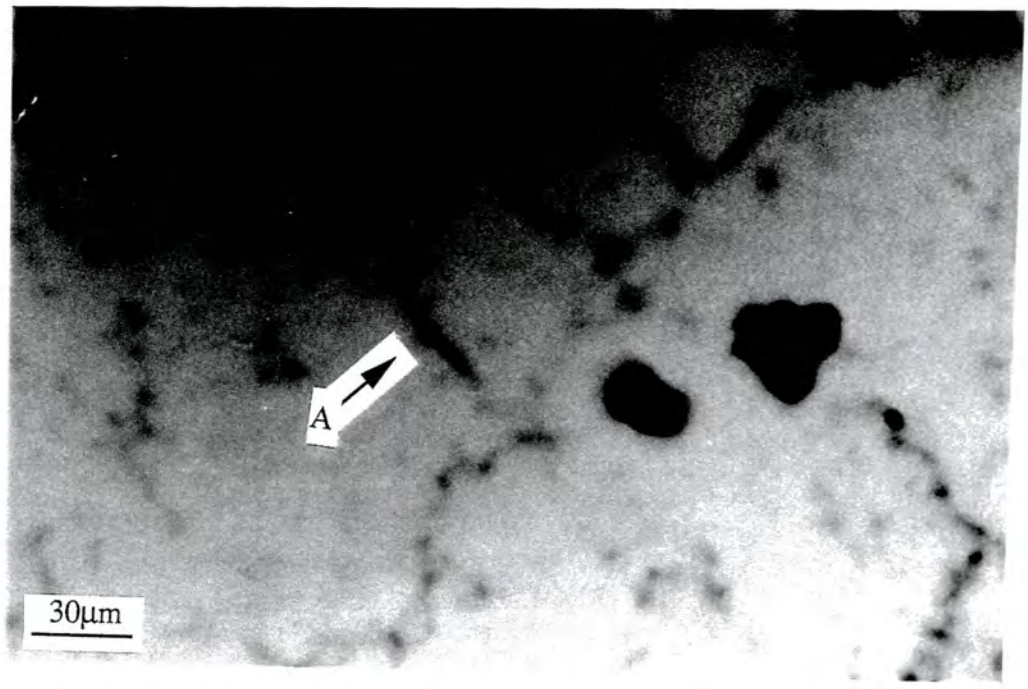

(a)

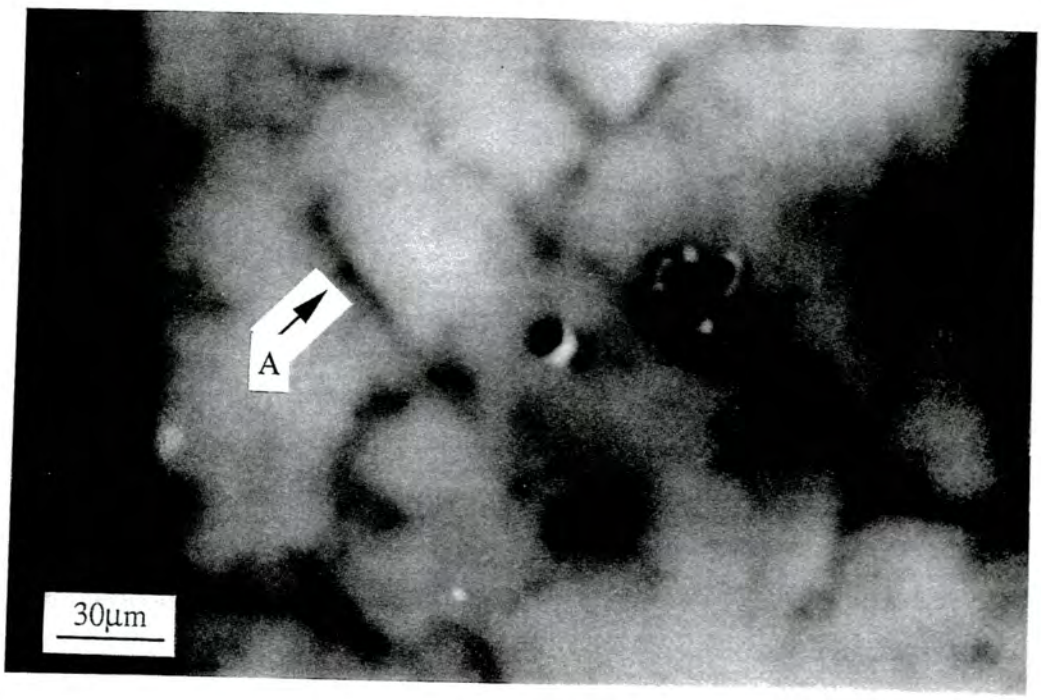

(b)

Figure 4.1 CL (a) and EBIC (b) micrograph of an identical area of a Bridgman grown CdTe sample.

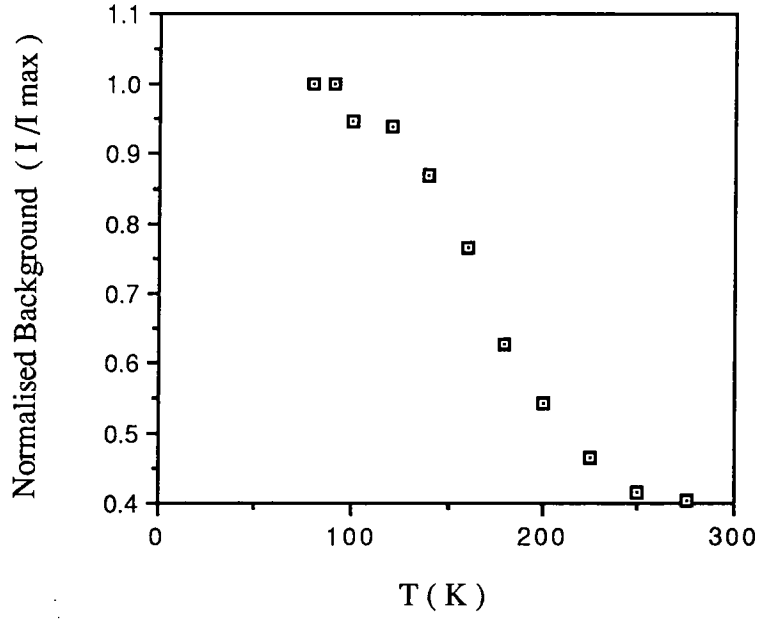

Figure 4.2 Normalised variation in background luminescence. i.e I / Imax.

4.3.1 Twin Boundaries

Extended dark line contrast features corresponding to twin and grain boundaries were commonly observed in vapour grown CdTe and to a lesser extent in Bridgman grown samples. First order Σ=3 lateral and coherent twin boundaries were identified by comparison with etching experiments [22] (see also section 5.4.1). Figure 4.3 shows a twin lamella in a vapour grown CdTe sample with both lateral and coherent boundary segments, the former being characterised by strong continuous contrast (as at B) and the latter by discontinuous contrast (as at A). Temperature dependent contrast was measured for both types of twin boundaries and is plotted in figure 4.4. The lateral boundary is associated with a high level of contrast which is virtually invariant over the temperature range studied, whereas the coherent boundary showed weaker contrast, peaking at ~ 150K.

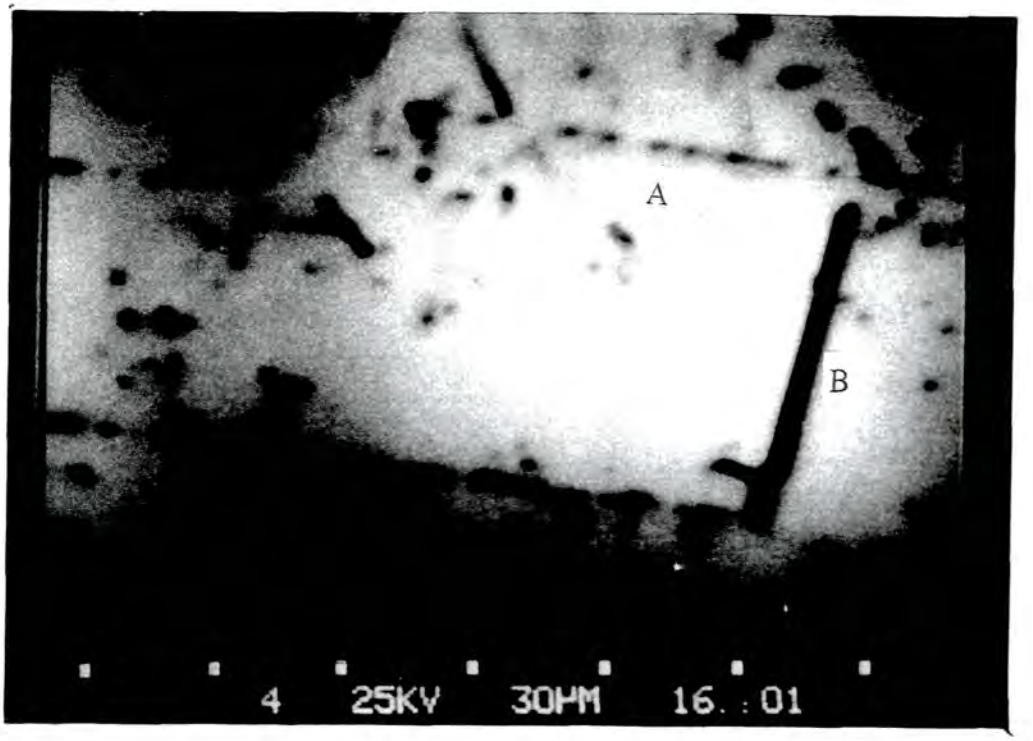

Figure 4.3 CL micrograph of a twin lamella in CdTe. The segment labelled B is a first order (Σ=3) lateral twin boundary and the segment labelled A is a first order (Σ=3) coherent boundary.

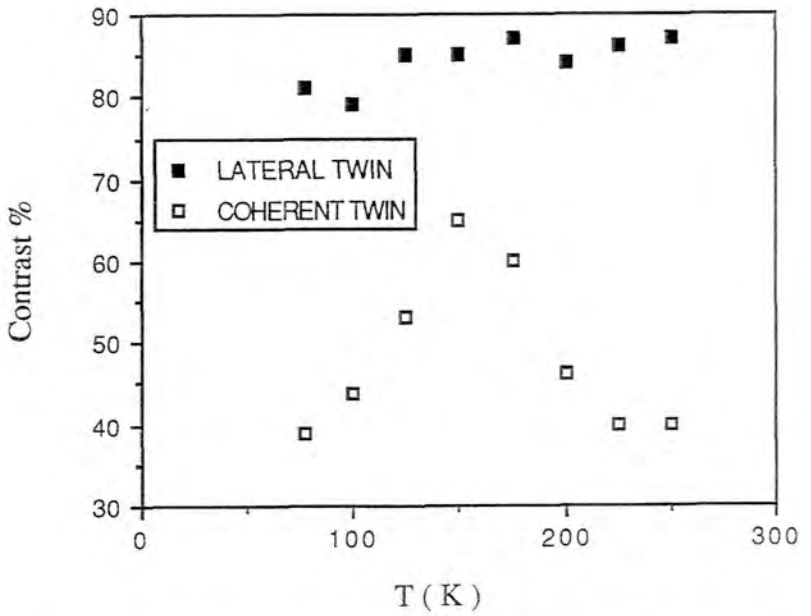

Figure 4.4 Temperature dependence of CL contrast at the Σ=3 lateral and coherent twin boundaries shown in figure 4.3.

4.3.2 Precipitates

Te precipitates have been identified in CL micrographs of CdTe as spots of dark contrast by correlation with EDAX, IR microscopy and defect etching results (see chapter 5 and ref.[23]). Figures 4.5a and 4.5b shows the correlation observed between precipitates decorating a lateral twin boundary revealed upon ferric chloride defect etching and areas of strong CL contrast, e.g at A in both micrographs, whereas figures 4.6a and 4.6b show a similar correlation (feature p3) at a precipitate not located at a twin boundary. The precipitates observed in figures 4.5 and 4.6 were identified as Te inclusions by EDAX analysis, a typical trace being shown in figure 4.7. Those precipitates decorating twin boundaries, such as p1 in figure 4.8 and p2 in figure 4.9, were clearly distinguishable in CL being represented typically by spots 5-10 μm in size. Precipitates away from twin boundaries were not so readily distinguishable; for example, that labelled p3 (figure 4.6b) is revealed by a contrast qualitatively similar to that observed at the surrounding features, which are assumed to be dislocations. Both types of defect are represented by dark spots 2-5 μm in size. The precipitate is tentatively identified in the CL micrograph because of its qualitatively stronger contrast.

In order to quantitatively characterise the CL contrast at precipitates, the variation of contrast as a function of temperature at the features p1,p2 and p3 (figures 4.8, 4.9 and 4.6b) was measured and the graphs obtained are shown in figure 4.10. All the plots in figure 4.10 reveal a similar shape, at low temperatures (i.e < 150K) the contrast for all the features shows only small variations (of less than 10%) with the maximum contrast readings (65-95%) being located in this range. On increasing the sample temperature the contrast of all three precipitates was observed to decrease, and by 250K features p1,p2 and p3 all had contrasts of <40%. This contrast behaviour is discussed in section 4.4.

The occurrence of Cd precipitation in CdTe samples was easily identifiable in CL micrographs, such defects being revealed by 'star' shaped features ~ 40μm in size. A typical example is shown in figure 6.14 and the occurrence of Cd precipitation is discussed in 6.2.3.

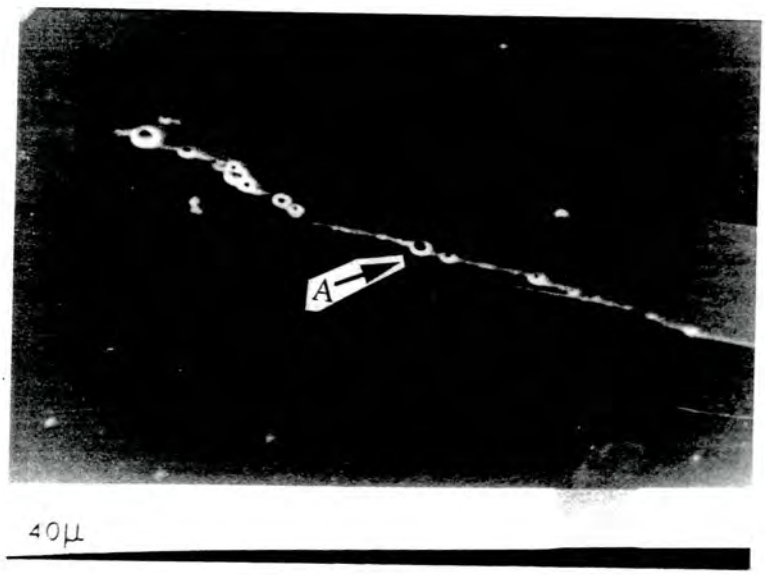

(a)

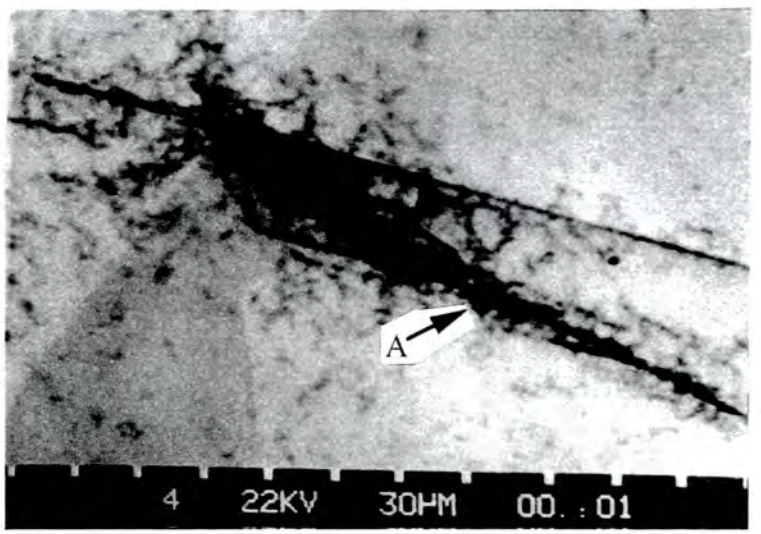

(b)

Figure 4.5 Precipitates decorating a lateral twin boundary in CdTe, as revealed by (a) SEM, after ferric chloride etching and (b) CL.

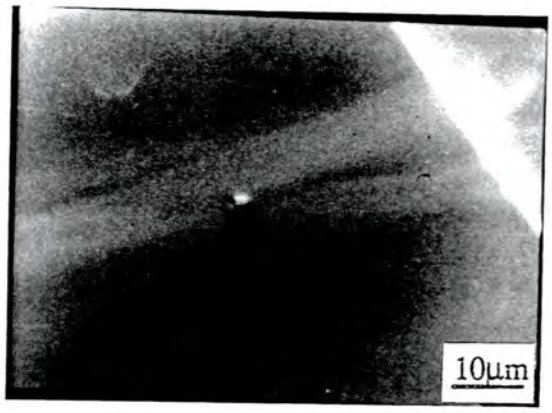

(a)

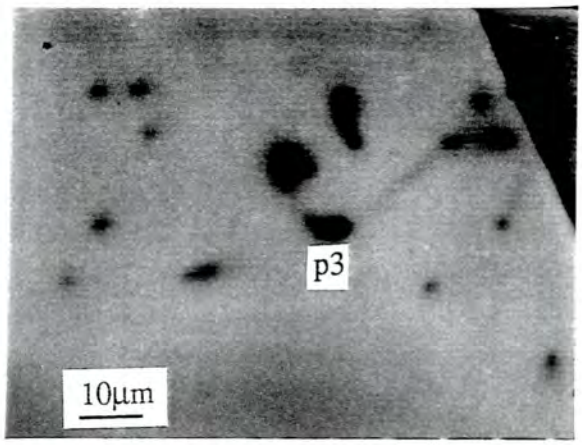

(b)

Figure 4.6 Precipitate (p3) in the bulk of a $Cd_{0.96}Zn_{0.04}Te$ sample, as revealed by (a) SEM, after ferric chloride etching and (b) CL.

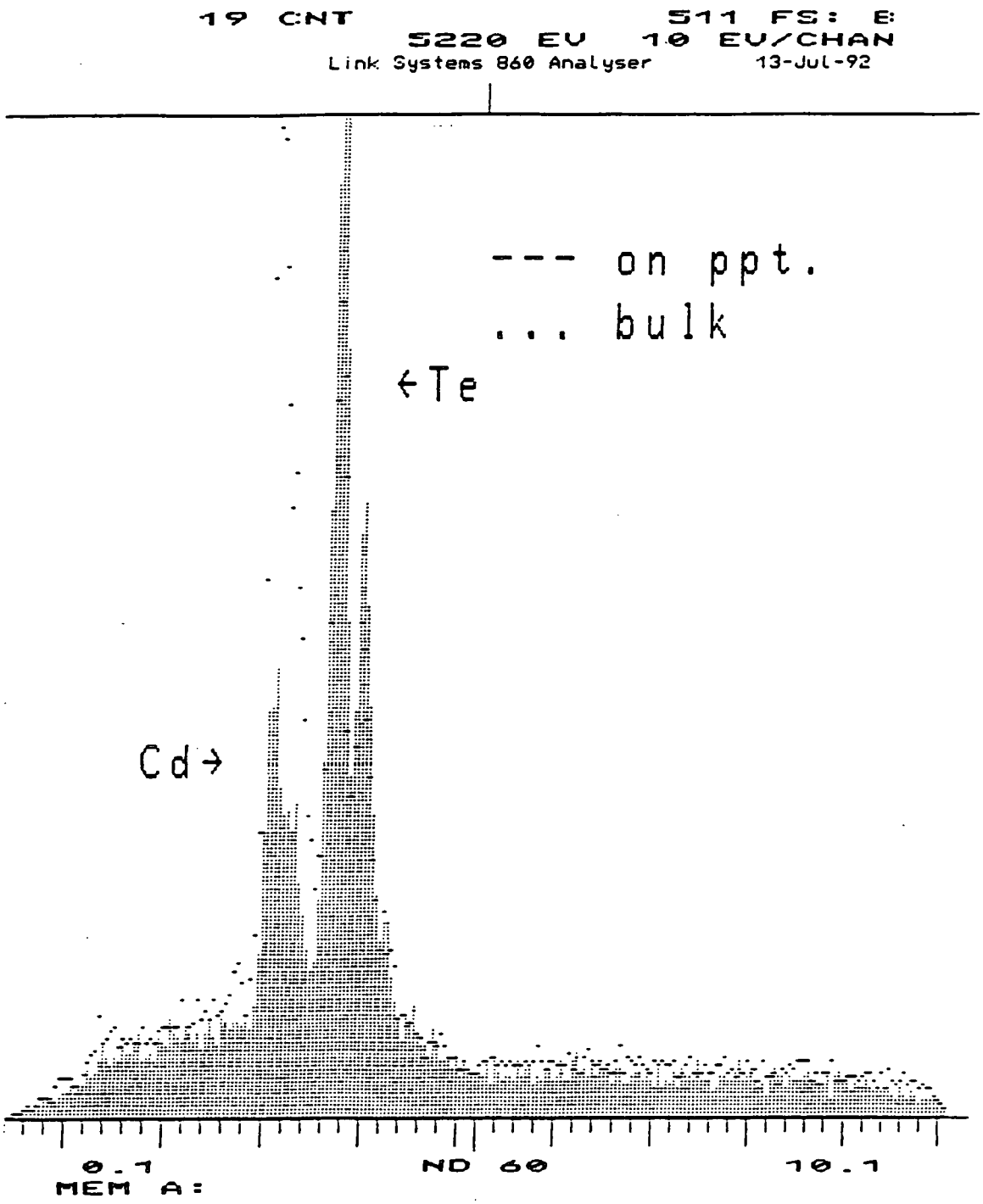

Figure 4.7 Typical EDAX image of precipitates shown in figures 4.5 and 4.6. The solid line shows the spectra obtained from the precipitates whereas the dotted trace was recorded from the CdTe matrix.

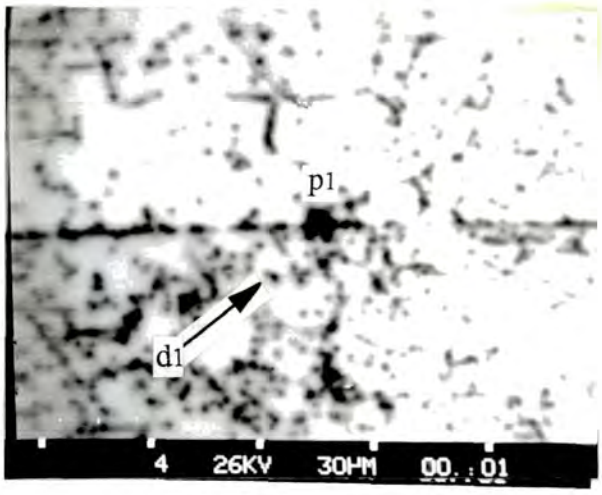

Figure 4.8. Precipitate p1 and dislocation d1.

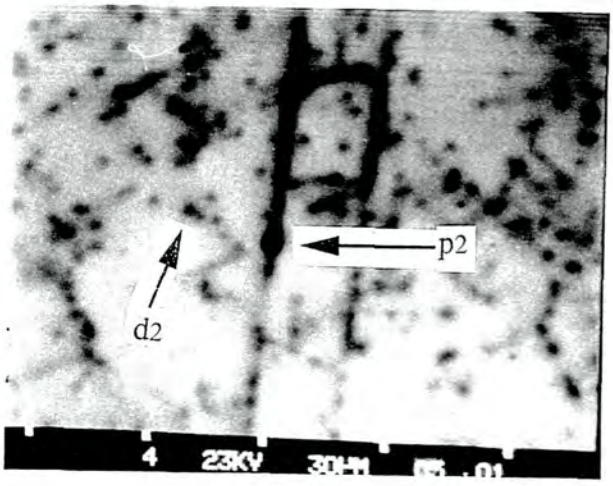

Figure 4.9. Precipitate d2 and dislocation d2.

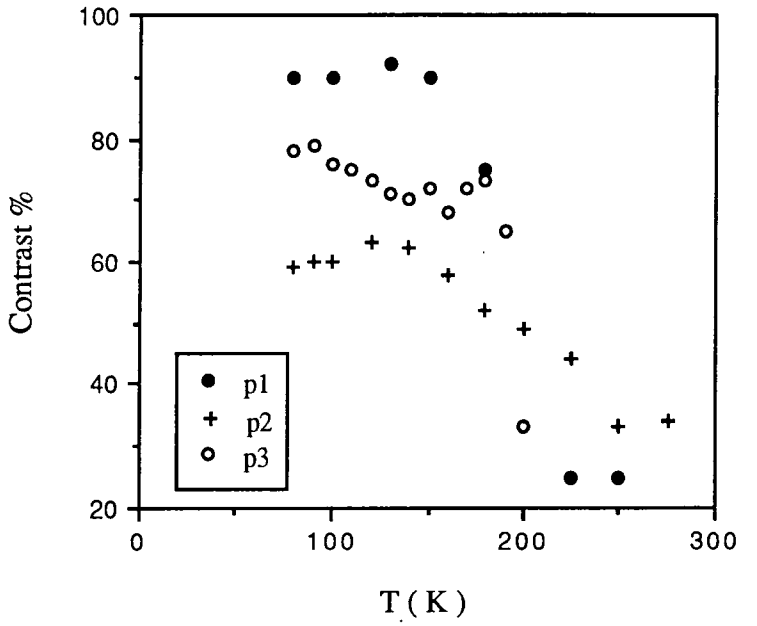

Figure 4.10 Temperature dependence CL contrast at of Te precipitates in CdTe. Precipitates p1 and p2 were located on first order coherent twin boundaries (in CdTe) , whereas p3 was observed in a bulk $Cd_{0.96}Zn_{0.04}Te$ sample.(Each contrast reading was accurate to ± 5%).

4.3.3 Dislocations

Dislocations have been identified in CdTe and (Cd,Zn)Te samples by the observation of cellular arrays of spots or lines of dark CL contrast, consistent with the imaging of sub-grain boundaries reported in etching experiments [9,24]. In Bridgman grown CdTe samples loose arrays of spots forming cells typically 90μm in size (figure 4.11) were observed, with an average inter-spot separation of typically 5μm being measured (figure 4.12). The average size of the dislocation CL spots in figure 4.12 is 1-3 μm, for a 18keV primary beam energy. The observation of individual spots such as those in figure 4.12 indicate the location of individual dislocations and in this micrograph they are present at a density of ~3 x 10^5 cm^{-2}. In vapour grown CdTe samples however dense arrays of dislocations in cells ~150μm wide were observed with individual dislocations being unresolvable, hence producing the lines of extended contrast visible in the CL micrograph as shown in figure 4.13.

The variation of contrast with temperature was analysed at CL spots located at dislocations in an attempt to qualitatively distinguish these features from those

representing precipitates. The graphs obtained for dislocations d1 and d2 (figure 4.8 and 4.9) are shown in figure 4.14 while the plot for d3 (figure 4.12) is shown in figure 4.15. The contrast at d1 and d2 was measured in the temperature range 77 - 300K whereas that at d3 was measured in the range 25 - 300 K. All the plots in figures 4.14 and 4.15 show an increase in contrast with increasing temperature, up to the maxima (35-70%) at 150K. On further increase of temperature the contrast at all three dislocations was observed to fall, and at 275K the contrast values of d1,d2 and d3 were in the range 10 -50%.

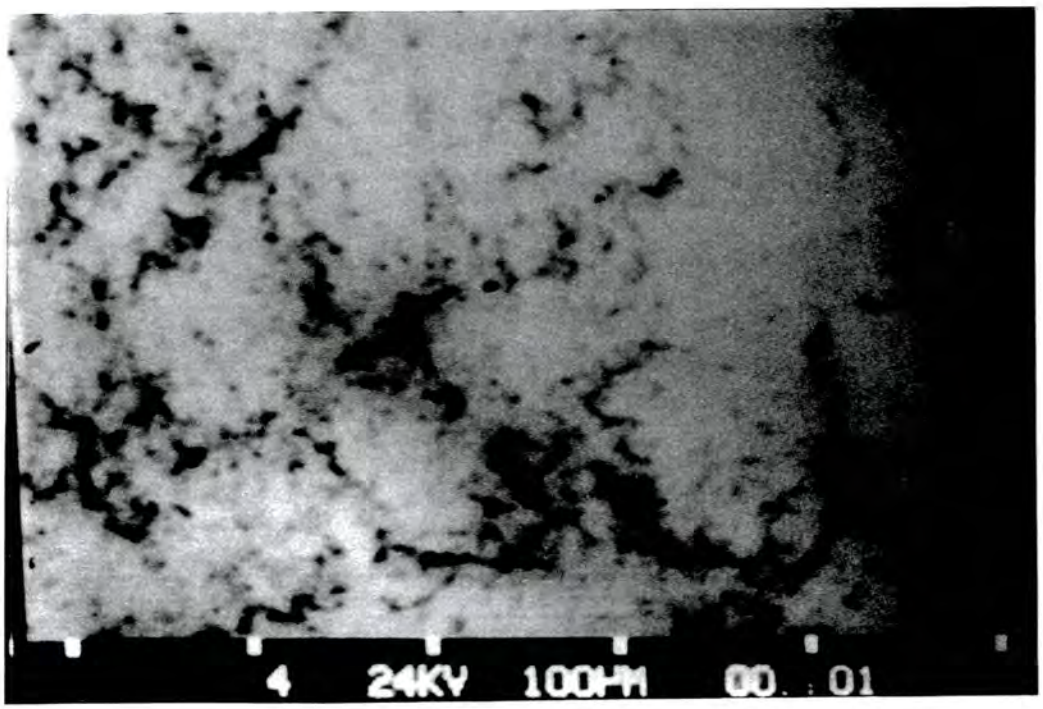

Figure 4.11 CL micrograph of sub-grain boundary network in Bridgman grown ACRT CdTe

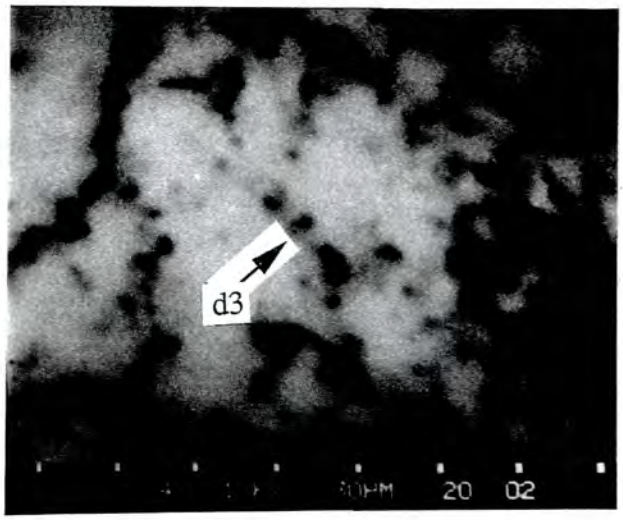

Figure 4.12 CL micrograph of individual dislocations in Bridgman CdTe.

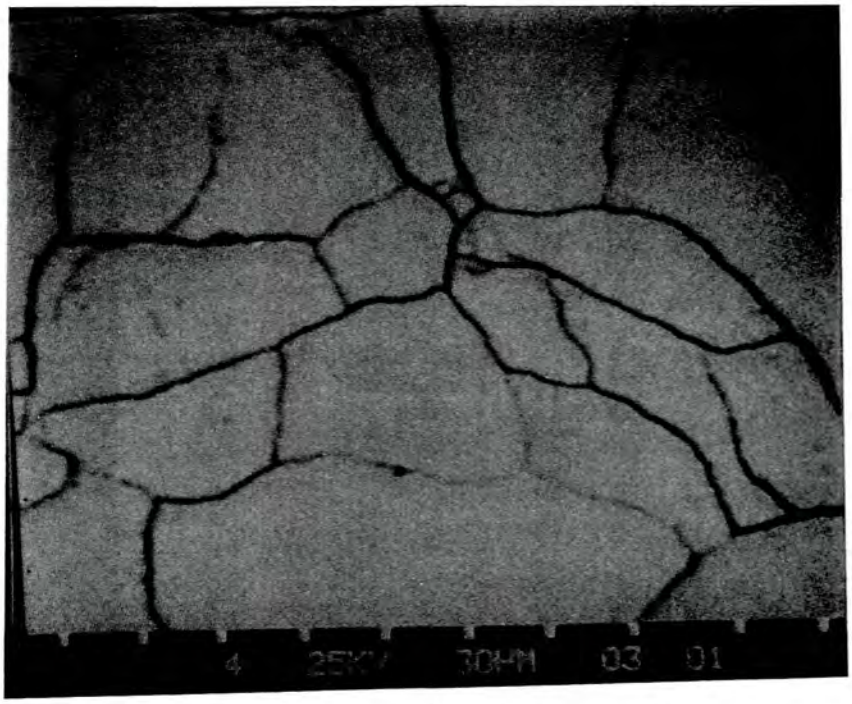

Figure 4.13 CL micrograph of sub-grain boundary network in vapour grown CdTe.

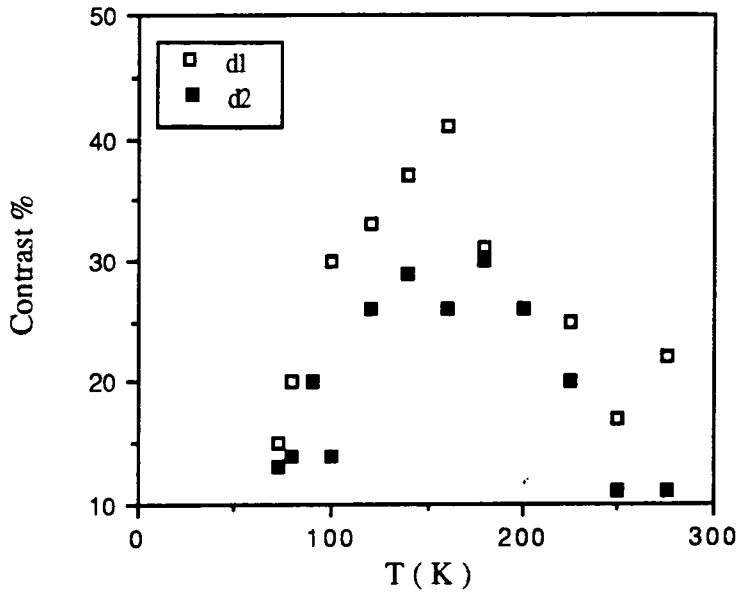

Figure 4.14 Temperature dependence of contrast at dislocations (d1 and d2, of figures 4.8 and 4.9) in CdTe.

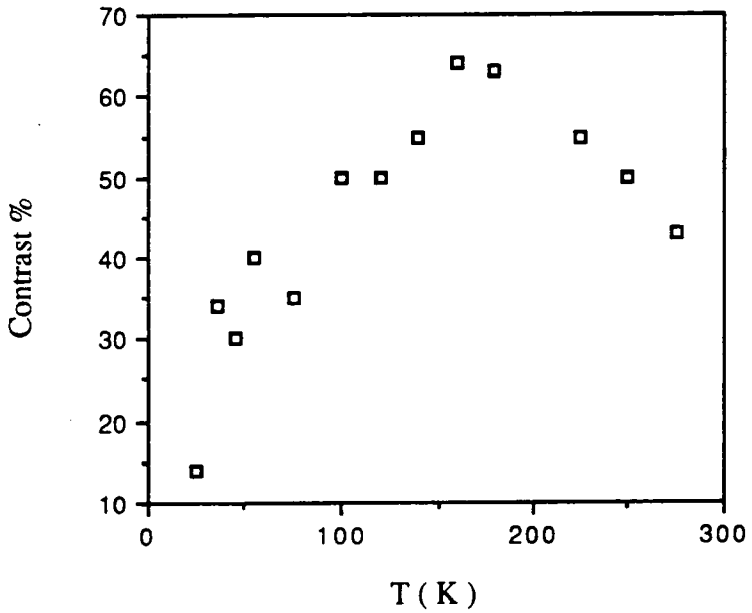

Figure 4.15 Temperature dependence of contrast at dislocation (d3, of figure 4.12) in CdTe, sample cooled with liquid helium enabling measurements in the temperature range 25-300K.

4.4 Discussion

The twin boundaries distinguished in figure 4.3 were easily identifiable Σ=3 coherent and lateral types by reference to etching studies and coincidence site lattice models [22,25]. The observation of strong continuous contrast at Σ=3 lateral twin boundaries and of weaker discontinuous contrast at coherent boundaries demonstrates qualitatively that non-radiative recombination is stronger at lateral twin boundaries. This is in accordance with EBIC observations of the same type of boundary in CdTe [25] and supports the hypothesis based on coincidence site lattice models that lateral boundaries have a higher proportion of wrong bonds than coherent ones and are therefore stronger recombination centres. The preferential decoration of lateral twin boundaries (figure 4.5 and also see chapter 5) by precipitates also strongly enhances the contrast of these boundaries. There are also distinct differences in the temperature dependent contrast obtained from the two types of boundary (figure 4.4), the lateral boundary showing a quantitatively stronger contrast than the coherent boundary, thus appearing to validate the method of temperature dependent CL contrast fingerprinting of crystallographic defects in semiconductors [26].

The temperature dependent contrast technique is of particular importance in distinguishing defects represented by a qualitatively similar contrast, such as that observed at isolated Te precipitates and dislocations. Although the precipitate shown in figure 4.6b is revealed by a qualitatively stronger contrast than that of the surrounding dislocations, the maximum contrast measured at a defect will vary as a function of the defect depth and the excitation conditions (i.e electron beam energy and beam current), for instance the precipitates p1,p2 and p3 (figure 4.10) show a contrast in the range of 50-90 % at 77K. Therefore in order to quantitatively distinguish between defects of a similar appearance, comparisons are required between plots of their respective normalised contrasts (i.e. C / C_{max}). Such a comparison for the features d1 and p3 (figures 4.14 and 4.10) is shown in figure 4.16, revealing a distinct difference in the shape of the two curves, thus obtaining a quantitative discrimination between the CL contrast observed at Te precipitates and dislocations.

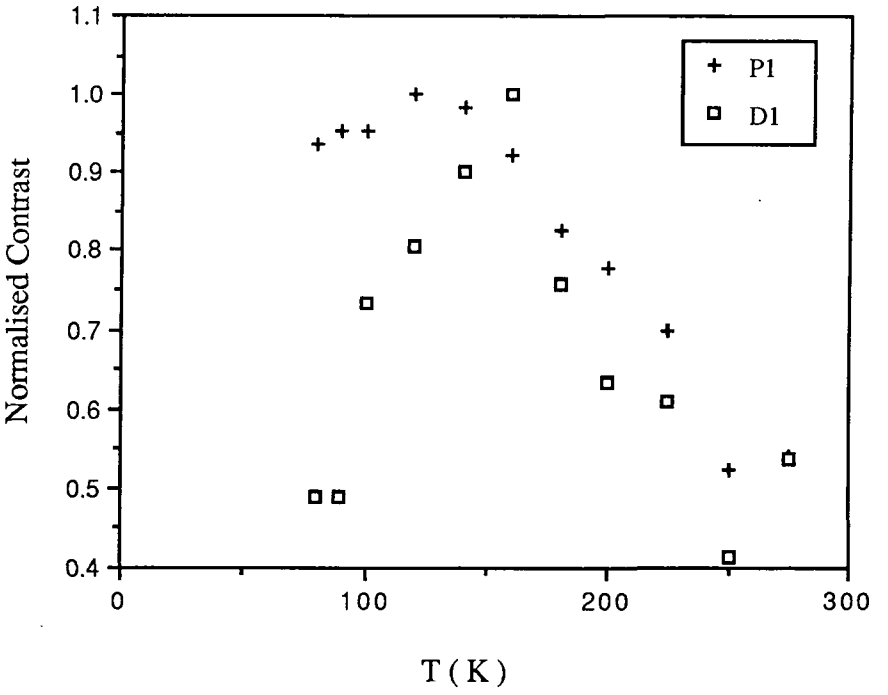

Figure 4.16 Comparison of normalised contrast observed at a dislocation (d1) and a Te precipitate (p3). The differences in the two curves (especially at low temperatures) enables the contrast of the two types of defects to be quantitatively distinguished.

The high contrast typically measured at precipitates at low temperatures, compared to that observed at dislocations, is a result of the physical nature of the Te inclusion. Elemental Te behaves as a metal at room temperature, having a zero band gap [27] and hence a zero excess minority carrier concentration (i.e $\Delta p = 0$) and an infinite surface recombination velocity (i.e $S = \infty$) [15]. At 0K however Te is a semiconductor with an energy gap of 0.33eV [27], this corresponding to an intrinsic luminescence of wavelength ~ 3.7μm. Radiation of this wavelength is however beyond the detection limit of the CL system used in this work, therefore at all temperatures in the range 77-300K Te precipitates are represented by contrast consistent with that observed at a defect with an infinite surface recombination velocity. It may be therefore expected that precipitates are revealed by a contrast of 100%, due to a zero luminescence signal from the defect (i.e $I_D = 0$). This will only be true however if an entire generation volume (when the electron beam is at a defect) contains only elemental Te, otherwise the CdTe matrix will contribute to the luminescence and a finite I_D will be observed at the defect (e.g Precipitates p1,p2

and p3 have maximum contrasts of < 100% and are therefore characterised by a finite I_D at all temperatures). Thus the CL luminescence from a Te precipitate (I_D) is determined by the fraction of the (electron -hole pair) generation volume occupied by the precipitate. Hence the contrast at a Te precipitate may be written;

$$C = \frac{I_0 - I_0(1 - V_p / V_g)}{I_0}$$

where Vg and Vp are the generation volume and the occupancy of the generation volume by a precipitate respectively. Therefore, on simplification ,the contrast at a precipitate is given by; $C = V_p / V_g$. The discussion of the temperature variation of CL contrast at Te precipitates is deferred until later in this section, at which point the contrast variation at precipitates is contrasted with both theoretical and experimental results obtained from contrast investigations of dislocations.

The decrease in background luminescence (I_0) with increasing temperature shown in figure 4.2, has been modelled for direct bandgap semiconductors by Jones [28], the decrease being accounted for by a higher probability of non - radiative electron - phonon transitions at increased temperatures [29].

The dislocation and sub-grain distributions seen in the Bridgman and vapour grown materials in figures 4.11 and 4.13 respectively are similar to those observed in the same material using other techniques such as etching [1], and the occurrence and nature of the sub-grain boundaries are discussed in section 6.2.1. The dislocation density calculated from CL micrographs (e.g ~ 3 x 10^5 cm^{-2} in figure 4.12) was significantly higher than the etch pit densities of ~5 x 10^4 cm^{-2} typically observed in identical CdTe samples after ferric chloride etching (see section 5.4.3). The difference indicates the penetration depth of the electron beam and the ability of the CL technique to reveal volume densities, e.g the dark spots in figure 4.12 correspond to a volume density of 10^9 cm^{-3} using an electron beam penetration of 2.1 μm at 18 keV [30]. Individual dislocations were unresolvable in the sub-grain boundaries observed in the vapour grown material, indicating the inter-dislocation distance to be less than the ~1μm resolution of the CL system.

In the following paragraphs the temperature dependence of the contrast variation at dislocations and precipitates is analysed with respect to the CL and EBIC contrast theories presented in chapter 3.

In section 3.2.3, theoretical expressions defining the CL and EBIC contrast at identical dislocations were shown to to have a similar form, with recombination in both techniques being a function of the recombination strength of the defect. Figures 4.1a and 4.1b confirm this experimentally, the EBIC and CL contrast observed at identical defects in the two micrographs being qualitatively similar. Furthermore the size of CL spots at dislocations in CdTe is comparable, to the size of EBIC spots at dislocations in Si. e.g ~2μm EBIC spots are typical at dislocations in Si for beam voltages of 15keV [31] and this is comparable to the 1-3 μm CL spots visible in figure 4.12, imaged using an electron beam energy of 18keV. Both techniques have a comparable spatial resolution and thus the CL recombination process at dislocations in CdTe occurs over a similar volume to the EBIC recombination process. The Wilshaw EBIC model (section 3.2.4.1 and [16]) is based on the band bending induced by a dislocation core. If for example the recombination observed by CL at dislocations in CdTe had been over an appreciably larger volume than that observed at dislocations by EBIC then a different recombination process would have been indicated (e.g due to the presence of an impurity atmosphere) and hence the Wilshaw model would have been inappropriate to the CL contrast results presented in this work. However from the similarities in both the experimental and theoretical results described above, it is likely that the Wilshaw EBIC model is relevant to CL.

The contrast curves for dislocations d1, d2 and d3 (figures 4.14 and 4.15) all indicate an increasing contrast at low temperatures and a decreasing contrast at temperatures above ~ 150K. These results are indeed consistent with those predicted by Wilshaw's EBIC temperature dependent contrast model, for at low temperatures it predicts a linear increase in contrast of the form ;

$$C \propto \gamma \propto T$$

and a reduction in contrast at high temperatures. However, due to the spread in the data points in figures 4.14 and 4.15 the applicability of the Wilshaw model to these results is yet to be conclusively shown. The data spread is probably due to the difficulty in obtaining reproducible contrast measurements at the exact centre of the CL spot under investigation.

Furthermore as shown in section 3.2.3, the temperature dependence of CL contrast at a dislocation has a functional dependence;

$C = f(\gamma, I_0, \tau_r, L, g(r), F(z), F)$

The optical losses (F(z)) in the system may be assumed to be temperature independent if it is assumed that the total (self) absorption of generated photons is independent of temperature. Such an assumption is valid as the value of the absorption coefficient for near band gap emission is nearly temperature independent in semiconductors [21,28]. If it is also assumed that the defect volume (F) and the generation function (g(r)) are temperature independent then the temperature dependence of the contrast is a function of $\gamma(T)$, L(T), I_0 (T) and τ_r (T). The Wilshaw model only considers $C \propto \gamma$ however in order to fully validate the suitability of Wilshaw's model for dislocations imaged using CL, the temperature dependences of L and τ_r for CdTe are also required (the temperature dependence of I_0 has previously been shown). For example, Eckstein et al [21] account for the temperature dependent CL contrast variation at dislocations in GaAs as the result of a changing minority carrier diffusion length. The CdTe minority carrier diffusion length is likely to vary with temperature `however attempts to measure this variation using the CL linescan technique described by Löhnert and Kubalek [19] were inconclusive. (Results obtained for CdTe samples in this work had too much scatter for meaningful interpretation). EBIC techniques such as those reviewed by Holt [32] may be used to obtain more reproducible minority carrier length values, but this was not attempted in this work. The impurity decoration of the defect [33], and the dislocation type (i.e edge, screw , 60^o) and geometry have also not been taken into account. TEM and X-ray topography are suitable techniques for examining the type and geometry of the dislocations and DLTS may be used to examine active levels which may be impurity related.

In order to ascertain whether the CL contrast variation at dislocations do not obey the Wilshaw theory a larger number of results, containing a greater number of data points are required. Also the CL contrast variation with beam current would be of use in determining the recombination process. It is also possible that the Wilshaw band bending model is intrinsically unsuitable for II-VI semiconductors (i.e for EBIC as well as CL), due to the higher ionicity of these materials (compared to Si) creating a large band bending even at uncharged dislocations. Hence to examine the applicability of the Wilshaw model to CdTe in general, EBIC contrast measurements will be required. Unfortunately due to serious equipment failure additional CL and EBIC contrast measurements were unobtainable and hence the contrast results presented in this work may only be described as preliminary.

The expression modelling the CL contrast at a dislocation (equation 3.1 in section 3.2.3) is based on the assumption that the excess minority carrier concentration inside a defect is approximately equal to the concentration that would occur in the absence of a defect. As previously discussed this is not the situation at Te inclusions, these defects being characterised by a zero excess minority carrier concentration and infinite surface recombination velocity. Therefore the contrast variation at a Te precipitate is not described by dislocation contrast models but as was shown earlier, it is governed at least partly by its fractional occupancy of the generation volume, i.e $C = V_p / V_g$. Therefore in the absence of other considerations this model is inadequate to describe the variation of contrast shown in figure 4.10, since to a first approximation the volumes V_p and V_g are independent of temperature. Other effects however may include the variation of minority carrier diffusion length with temperature which might act to increase the generation volume beyond the electron range [34]. If the minority carrier diffusion length increases with temperature this would act to decrease the contrast at high temperatures. For example, the generation volume may be considered to be a sphere having a radius equal to half the Kanaya and Okayama [30] range (e.g 1.75μm at 25keV). As previously described, preliminary attempts to measure the minority carrier diffusion lengths by the Löhnert and Kubalek [19] CL technique produced inconclusive results. They did however indicate a minority carrier diffusion length range from about 1 to 2μm over the temperature range 77 - 300K. For a precipitate of diameter 5μm this would imply a contrast range of 75% to 30% for a 25keV electron beam. (Assuming that the radius of generation volume + minority carrier diffusion length equals 2.75μm and 3.75μm at 77K and 300K respectively.) This is broadly in line with the observed temperature dependent contrast plots for precipitates shown in figure 4.10. However, the contrast variation predicted is a function of the fraction of the generation volume occupied by the precipitate and this could lead to variations in the contrast behaviour at precipitates of different size. Furthermore the position of a precipitate in the generation volume may lead to greater or lesser screening of the luminescence excited from beneath the defect.

Another influence on the contrast may be junction effects at the CdTe /Te precipitate interface. A CdTe / Te interface has a barrier height of ~ 0.5eV (at 300K) [35] and will result in a bending of the energy bands. Therefore electron and hole pairs generated in this region will be spatially separated, thus resulting in a decrease in the CL luminescence (i.e I_0). As the temperature increases and the Fermi level in the p-type CdTe rises towards the centre of the band gap, the band bending at the

interface will decrease. Therefore a rise in background luminescence (I_0) and a fall in contrast is predicted.

4.5 Conclusion

The CL technique has been shown in this chapter as an excellent technique for the characterisation of as-grown defects in boules of CdTe and (Cd,Zn)Te. Twin boundaries, precipitates and dislocations were imaged as either lines or spots of dark contrast. CL microscopy has been seen to image such defects by a contrast qualitatively similar to that observed at identical defects using the EBIC technique but has the advantage of not requiring the fabrication of electrical contacts to the sample surfaces. The correlation of CL results with those obtained using a ferric chloride defect etching solution is examined in Chapter 5.

The temperature dependence of CL contrast at defects has been shown by this work to be useful in distinguishing between different types of defects which have similar contrast features. This principle was first validated by examining lateral and coherent Σ=3 twin boundaries; the former of which displayed high contrast at all temperatures from 77-300K while the latter showed a contrast peak at 150K (see figure 4.4). The differences may be due to bonding and decoration. This temperature dependent contrast technique is perhaps more useful in providing a method of distinguishing between the dark CL spots at dislocations and those at small precipitates: precipitates of size <2μm are not easily observed by IR microscopy. Te precipitates show nearly constant contrast up to 150K which decreases thereafter whereas dislocations exhibit a large increasing contrast for temperatures up to 150K. Thus the comparison of image contrast at 77K and room temperature enables the dark spots due to precipitates to be distinguished.

The high contrast at precipitates at low temperatures may be simply accounted for by the modelling of Te inclusions as defects with an infinite (to a good approximation) surface recombination velocity, and by also considering the fractional occupancy of the generation volume by the precipitate. The reduction in contrast with increasing temperature observed at Te precipitates however remains unclear, although it is likely that this is a result of the variation in both the minority carrier diffusion length and the CdTe / Te barrier height. The CL contrast temperature dependence at dislocations is consistent with that predicted by the Wilshaw EBIC temperature dependence model. However due to the large spread in

the data points the validity of the Wilshaw model to the CL results obtained at dislocations in CdTe is yet to be fully determined. In order for the CL recombination process to be fully modelled a larger number of results are required, and the type, geometry and impurity associations of the dislocations examined also need to be investigated. The temperature dependence of CL recombination processes in CdTe, such as minority carrier lifetime and minority carrier diffusion length, also need to be determined.

Therefore although temperature dependent CL analysis may be utilised to distinguish precipitates from dislocations, the recombination mechanisms responsible for the differences in the contrast curves from one dislocation type to another are still not completely clear.

REFERENCES FOR CHAPTER FOUR

1. L.O. Bubulac,W.E. Tennant, D.D. Edwall, E.R. Gertner and J.C. Robinson, J. Vac. Sci. Tecnol. **A3** (1985) 163.
2. A.K. Chin, J. Electochem Soc. **129** (1982) 1151.
3. K. Nakagawa, K. Maeda and S. Takeuchi, Appl. Phys. Letters **34** (1979) 574.
4. G. Brandt, H. Ennen, R. Moritz and W. Rothemund, J. Crystal Growth **101** (1990) 226.
5. C.B. Morris and K.R. Zanio, J. Appl. Phys. **53** (1982) 6747.
6. C.B. Morris and C.E. Barnes, Rev. Phys.Appliquée **12** (1977) 219.
7. D. Wood, Ph.D Thesis, University of Hull, 1985.
8. D.E. Cooper, J. Bajaj and P.R. Newman, J. Crystal Growth **86** (1988) 544.
9. L.O. Bubulac, J. Bajaj, W.E. Tennant, P.R. Newman and D.S. Lo, J. Crystal Growth **86** (1988) 536.
10. M. Wada, J. Suyuchi and H. Hosomatsu, Jap. J. Appl. Phys. **25** (1986) L780.
11. H. Blumtritt, G.N. Panin, G.B Yakimov and J. Heydenreich, Phys.Stat.Sol. (a) **109** (1988) K3.
12. B. Sieber and J.L. Farvacque, in : Microscopy of Semiconducting Materials 1987, Inst. Phys. Conf. Ser. **87**, (Eds.) A.G. Cullis and P.D. Augustus (Inst. Phys., Bristol, 1987), p.739.
13. G.N Panin and E.B. Yakinov in, : Microscopy of Semiconducting Materials1991, Inst. Phys. Conf. Ser. **117**, (Eds.) A.G. Cullis and N.J. Long (Inst. Phys., Bristol, 1991), p.763.
14. C. Donolato, Optik **52** (1978) 19.
15. A. Jakubowicz, J. Appl. Phys. **57** (1985) 1194.
16. P.R. Wilshaw, T.S. Fell and G.R. Booker, in : 'Point and Extrnded Defects in Semiconductors', (Eds.) G. Benedek, A. Cavallini and W. Schroter (Plenum, New York, 1989), p. 243.
17. A. Ourmazd, Cryst. Res. Technol. **16** (1981) 137.
18. A. Jakubowicz, J. Appl. Phys. **59** (1986) 2205.
19. K. Löhnert and E. Kubalek, phys.stat.sol. (a) **83** (1984) 307.
20. L. Paseman and W. Hergert, Izv. Akad. Nauk. SSSR. Ser. Fiz. **51** (1987) 1528.
21. M. Eckstein, A. Jakubowicz, M. Bode and H-U. Habermeir, SPIE **1284** (1990) 229.

22. K. Durose, G.J. Russell and J. Woods, in : Microscopy of Semiconducting Materials 1985, Inst. Phys. Conf. Ser.**76**, (Eds.) A.G. Cullis and D.B.Holt (Inst. Phys., Bristol, 1985), p.233.
23. C.C.R. Watson, K. Durose, A.J. Bannister, E. O' Keefe and S.K. Bains, Mat. Sci. Eng. **B16** (1993) 113.
24. K. Durose and G.J. Russell, J. Crystal Growth **86** (1988) 471.
25. K. Durose and G.J. Russell in, : Microscopy of Semiconducting Materials 1987, Inst. Phys. Conf. Ser. **87**, (Eds.) A.G. Cullis and P.D. Augustus (Inst. Phys., Bristol, 1987), p.327.
26. C.C.R. Watson and K. Durose, J. Crytal Growth **126** (1993) 325.
27. C. Kittell, 'Introduction to solid State Physics', (John Wiley and Sons (6^{th} Edition), New York, 1986), p. 185.
28. G.A.C. Jones, B.R. Nag and A. Gopinath, in : 'Scanning Electron Microscopy' 1973 / II, (Ed.) O. Johari (SEM inc., Chicago, 1973), p.309.
29. D.D. Yoffee, K.J. Howlett and P.M. Williams, in : 'Scanning Electron Microscopy '1973 / II, (Ed.) O. Johari (SEM inc., Chicago, 1973),p. 301.
30. K. Kanya and S. Okayama, J. Phys. D (Appl. Phys.) **5** (1972) 43.
31. see for example: S.A. Galloway, P.R. Wilshaw and T.S. Fell, in: Microscopy of Semiconducting Materials 1993, Inst. Phys. Conf. Ser., in press.
32. D.B. Holt, in:, 'Quantitative Scanning Electron Microscopy', (Eds.) D.B. Holt, M.D. Muir, P.R. Grant and I.M. Boswara, (Academic Press, London, 1974), chapter 8.
33. A. Berg, I. Brough, J.H. Evans, G. Lorimer and A.R. Peaker, Semicond. Sci. Technol **7** (1992) A263.
34. B.G. Yacobi and D.B. Holt, 'Cathodoluminescence Microscopy of Inorganic Solids', (Plenum, New York, 1990), p.59.
35. J.G. Werthen, J-P. Häring, A.L. Fahrebruch and R. H. Bube, J. Phys. D: Appl. Phys. **16** (1983) 2391.

CHAPTER FIVE

Qualification of a Saturated $FeCl_3$ Solution as a Defect Etchant for CdTe and (Cd,Zn)Te

5.1 Introduction

In this chapter the suitability of a saturated aqueous ferric chloride solution as a defect revealing etchant for CdTe and (Cd,Zn)Te substrates is examined. The action of the etch in revealing as-grown defects has been qualified in this work by correlating the location of etch pits with dark contrast features revealed by cathodoluminescence microscopy on a range of crystal orientations. In particular the feasibility of its use on the technologically important $(\bar{1}\bar{1}\bar{1})$B Te face has been investigated, and Section 5.4 describes this work. The performance of a number of defect etchants reported in the literature to be suitable for CdTe is reviewed in Section 5.2. Attention is especially drawn to the orientation dependence of their action and whether any direct correlation between the occurrence of etch pits and defects revealed by other structural characterisation techniques has been reported.

5.2 Review of Etching Solutions commonly used for CdTe

The use of defect revealing etches is a common technique for the structural evaluation of CdTe substrates, and a number of such etching solutions are discussed in the literature [1-6]. These are listed in table 5.1 which also discusses the advantages and disadvantages of each reagent. The majority of these etches have the drawback that they are not suitable for use on the technologically important $(\bar{1}\bar{1}\bar{1})$B crystal surface of CdTe and (Cd,Zn)Te, this being the orientation upon which epitaxial (Cd,Hg)Te is grown [7].

The most commonly used etchants are the Nakagawa [1] and Inoue [2] reagents with the Nakagawa solution being the most frequently used in the determination of dislocation densities [8]. The Nakagawa etchant is reported to develop pits on the

NAME	ETCH SOLUTION	COMMENT
Nakagawa [1]	HF, H_2O_2, H_2O (3:2:2)	Develops pits on {111}A faces of CdTe which have been correlated to dislocations observed by CL. Not reported to develop pits on $(\bar{1}\bar{1}\bar{1})$B CdTe [1,3,5]
Inoue [2]	HNO_3,H_2O,$AgNO_3$, $K_2Cr_2O_7$ (10ml,20ml,1.5mg,4g)	Develops pits on {111} A and B surfaces of CdTe. No 1:1 correlation between etch pits and defects reported. [2]
Photoetch [3]	1/2% bromine in methanol + visible light	Delineates etch lines at grain and sub-grain boundaries on all faces. Not reported to develop pits at individual dislocations. [3,10]
Chen [4]	HNO_3, HCl, H_2O,$K_2Cr_2O_7$ (20ml,10ml,80ml + 8g)	Reported to develops pits on {111} Cd and {110} faces of CdTe and on {111}A, {111}B, {110}, {100} and {311} faces of (Cd,Hg)Te. Not reported to develop pits on $(\bar{1}\bar{1}\bar{1})$B face of CdTe. [4]
Hähnert [5]	HF, chromic acid (50 wt% in H_2O), HNO_3 (1:1:1 + 20x dilution in H_2O) (For (Cd,Hg)Te HNO_3 replaced by HCl and 8x dilution)	Reported to develop pits on (111)A face of CdTe and on (111)A, (111)B and {110} faces of (Cd,Hg)Te.These pits have been correlated to dislocations revealed by X-ray topography. Not reported to develop pits on $(\bar{1}\bar{1}\bar{1})$B face of CdTe. [5]
Polisar [6]	HNO_3, HCl, CH_3COOH, bromine, H_20 (60ml, 25ml, 5ml, 0.1ml,90ml)	Reported to develop pits on (111)A face of CdTe and on all surfaces of (Cd,Hg)Te. Not reported to develop pits on $(\bar{1}\bar{1}\bar{1})$B face of CdTe. [5,6]

Table 5.1 Common defect revealing etches for CdTe

{111} Cd faces of CdTe [1,8,9] and a 1:1 correlation has been reported between pits on the (111)A face and defects observed by CL microscopy [1]. The etchant however is reported not to develop pits on the $(\bar{1}\bar{1}\bar{1})$B face of CdTe [9]. The Inoue reagent has been reported to develop pits on all crystal planes of CdTe but no 1:1 correlation has been observed between these pits and defects revealed by complementary techniques [5,8,9]. Apart from the Nakagawa solution, the only reagent reported to show such a 1:1 correlation is Hähnert's etchant which developed etch pits at identical locations to dislocations revealed by X-ray topography [5].

The photoetch [3] is reported to reveal line defects (e.g grain or sub-grain boundaries), delineated as either ridges or troughs, on all crystal orientations but individual pits were not seen [10]. The Chen [4], Hähnert [5] and Polisar [6] etching solutions are reported to have a similar etching action to one another, all three producing pits on a number of (Cd,Hg)Te faces, including the $(\bar{1}\bar{1}\bar{1})$B surface, but not developing pits on the $(\bar{1}\bar{1}\bar{1})$B face of CdTe.

This brief survey has revealed that an etching solution capable of developing pits at identical locations to defects revealed by complementary techniques, remains lacking for the $(\bar{1}\bar{1}\bar{1})$B surface of CdTe.

5.3 The Ferric Chloride Etching Reagent

The etchant was prepared by dissolving 35g of Analar $FeCl_3(H_2O)_6$ in 10ml of demineralised water to produce a saturated solution. When successive etch steps were used the etching reaction was quenched and the samples cleaned in distilled water. Defect etching was performed by waxing the samples onto glass slides and then dipping the slides into the solution for the required period, typically 2-3 minutes.

It is of note that although ferric chloride reagents have not been previously reported as defect etchants for CdTe and related materials, solutions based on it have been reported as defect etchants for InSb, InP, alkali halides [11] and Ni [12].

5.4 Results and Discussion

The CdTe crystal orientations examined were the (111)A, $(\bar{1}\bar{1}\bar{1})$B, {110}, {511}, {5 7 13} faces and a random polycrystalline boule. The (111)A and $(\bar{1}\bar{1}\bar{1})$B faces of $Cd_{0.96}Zn_{0.04}Te$ were also etched. Pits were developed on all of these orientations in both materials. A background etch rate was also observed, revealed by the removal of material from etched surfaces and was measured, using a hoverprobe, for the (111)A and $(\bar{1}\bar{1}\bar{1})$B faces of both materials. The etch rate was found to be linear with time and indicating a rate of ~2 μm min^{-1} on all measured faces. Figures 5.1a and 5.1b show the etch rate for $(\bar{1}\bar{1}\bar{1})$B CdTe and $(\bar{1}\bar{1}\bar{1})$B $Cd_{0.96}Zn_{0.04}Te$ respectively.

In this section the ability of the etch to reveal, and distinguish between, common crystallographic defects is reported and discussed. Wherever possible, micrographs of defects revealed by the ferric chloride solution are correlated to micrographs of the same features, imaged using a complementary technique, these being CL and IR microscopy. The aim was to test the etchant as a defect revealing reagent by attempting to find relationships between different types of etch pit and specific structural defects [13]. Specific attention was paid to the $(\bar{1}\bar{1}\bar{1})$B surface of both materials as no etchant has been proved to successfully reveal defects on this orientation.

5.4.1 Twin Boundaries

Twin boundaries were clearly delineated as lines after ~ 30 seconds of etching. Figure 5.2a is a S.E.M micrograph of the intersection of two twin lamellae on a $(\bar{1}\bar{1}\bar{1})$B CdTe surface, as revealed by ferric chloride etching. The etch developed lines representing first order ($\Sigma = 3$) [14] coherent and lateral twin boundaries and higher order boundaries as indicated at A, B and C in figure 5.2a. CL microscopy of the same area revealed an identical twin network (figure 5.2b), with a very strong contrast being observed at the first order lateral and second order segments of the twin boundaries. The explanation behind this strong contrast is discussed in section 4.4. Surface profiles (figure 5.3) across twin lamella on {111} faces, using an α - step surface profilometer, revealed a higher etch rate on the twin orientation than on the matrix. After 10 minutes of etching the twin lamella was

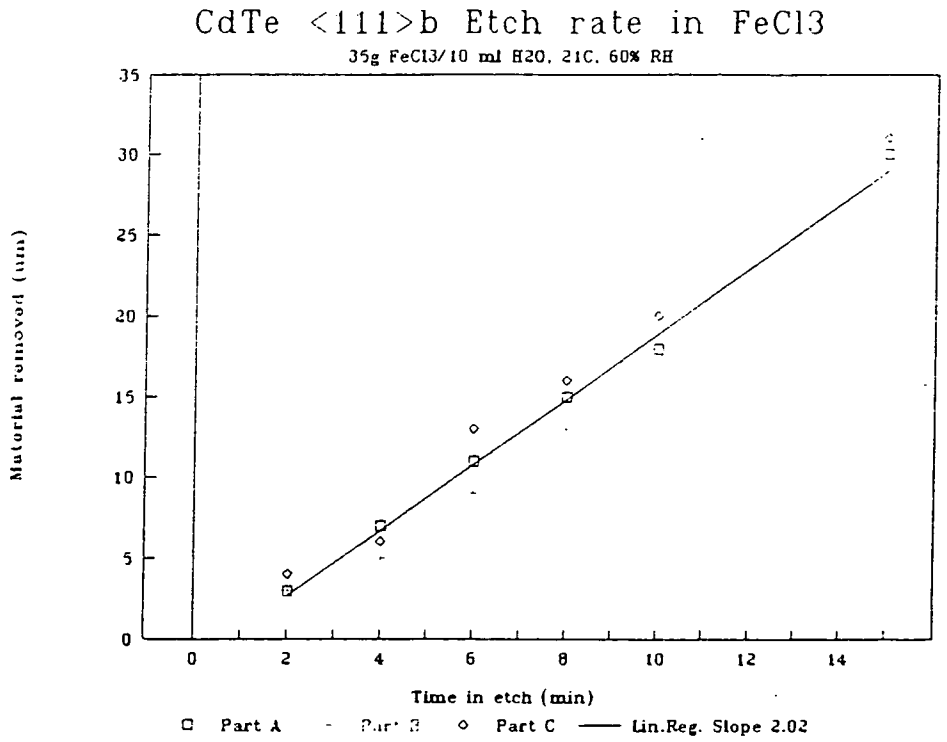

(a)

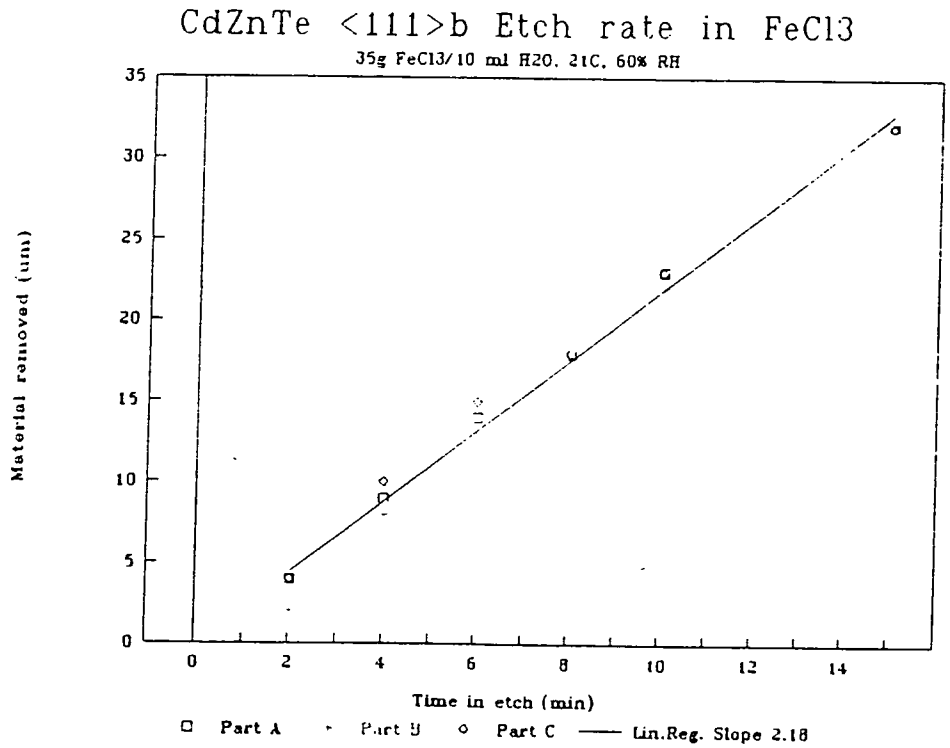

(b)

Figure 5.1 Ferric Chloride etch rate on (a) $(\bar{1}\bar{1}\bar{1})$B CdTe and (b) $(\bar{1}\bar{1}\bar{1})$B $Cd_{0.96}Zn_{0.04}Te$.

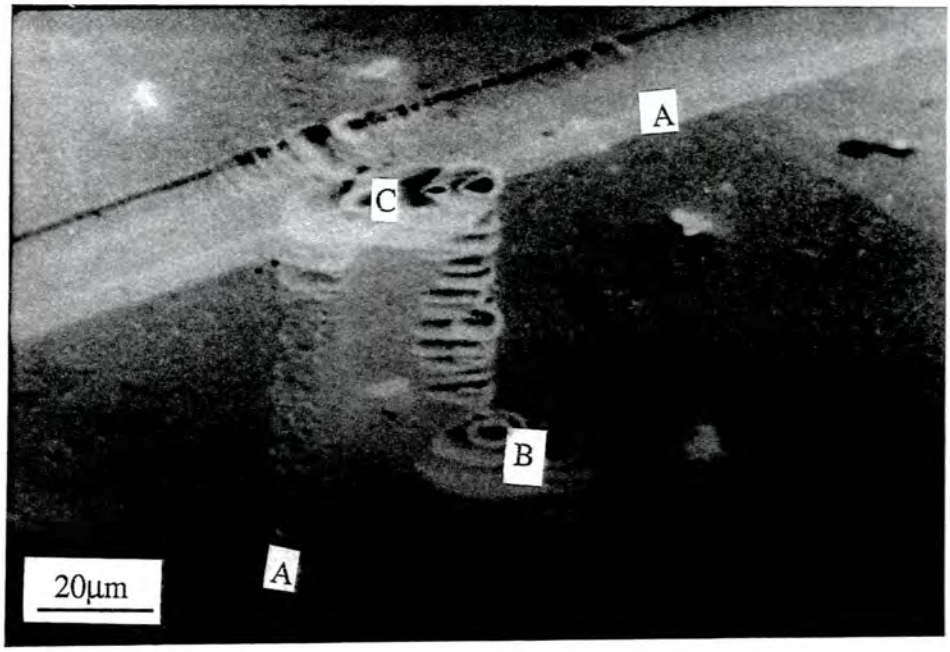

(a)

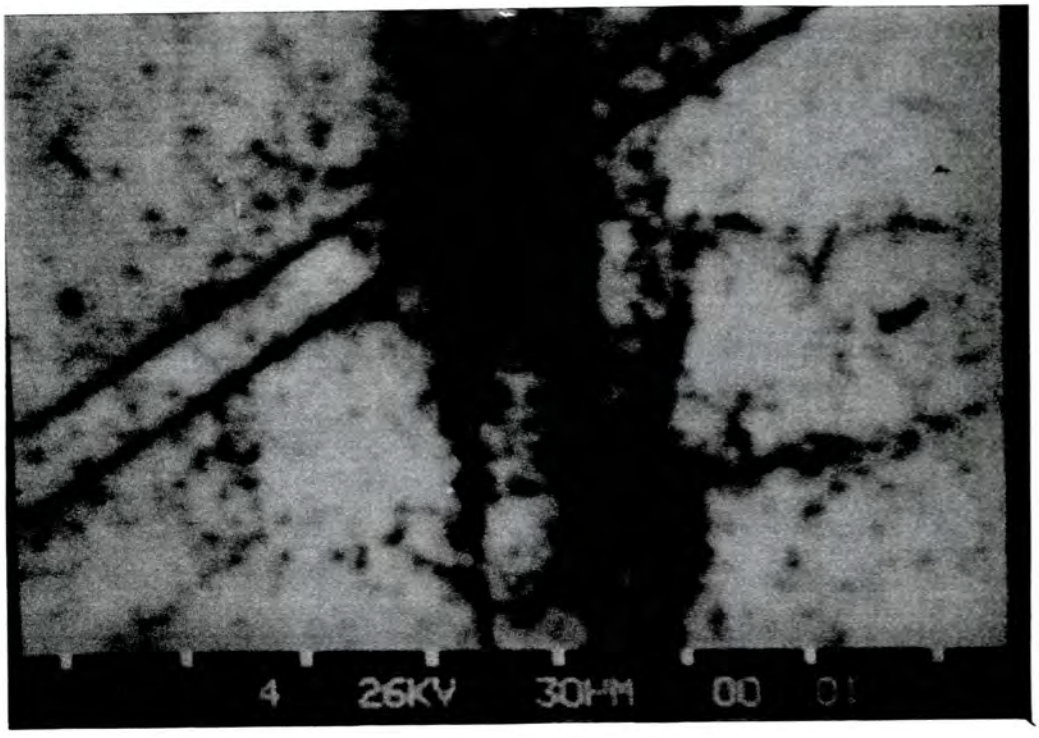

(b)

Figure 5.2 Intersection of two twin lamella as revealed by (a) SEM, after ferric chloride etching and (b) CL. Segment A is a first order (Σ=3) coherent boundary, B is a first order lateral twin boundary and C is a second order (Σ=9) twin boundary.

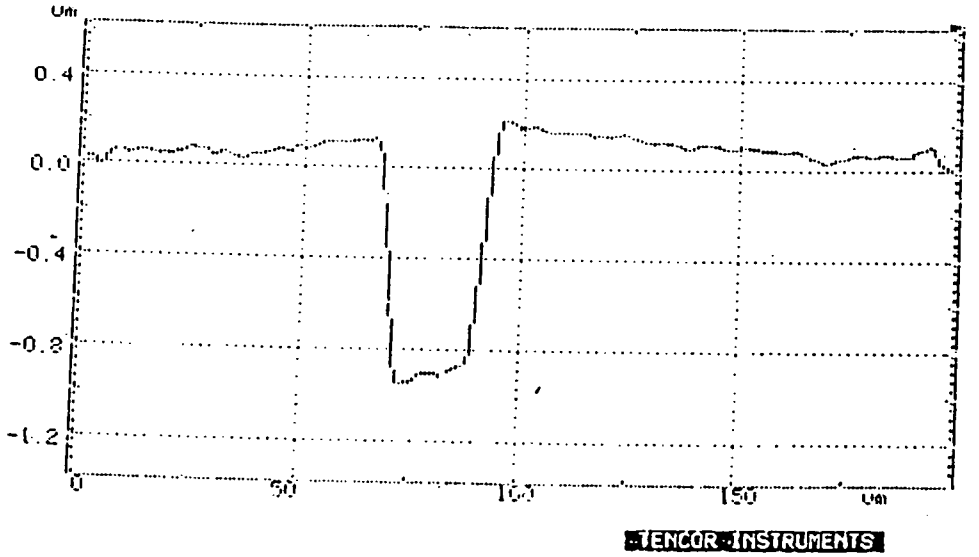

Figure 5.3 Profile across a (51$\bar{1}$) twin lamella after 10 minutes ferric chloride etching.

revealed as a trough ~ 10μm in depth, indicating an increased etch rate of ~1μm min^{-1} compared to the matrix. The twin boundaries are therefore delineated due to the differential etch rate at either side of the boundary. The twin orientation was established to be (5$\bar{1}\bar{1}$) by applying a matrix method [15].

5.4.2 Precipitates

All twin boundaries defined by ferric chloride solutions were seen to be decorated to a greater or less extent, with pits ~3-10μm in size (also see section 4.3.1). Examples of these may be seen on the twin boundaries shown in figure 5.2a. A direct 1:1 correlation was observed between pits of this type and precipitates imaged by IR microscopy. Figure 5.4a for example reveals dense pitting of a Σ=3 lateral twin boundary, which in IR microscopy (shown in figure 5.4b) was seen to coincide with the intersection of a band of precipitates and the ($\bar{1}\bar{1}\bar{1}$)B surface. These etch pits therefore undoubtedly indicate the presence of precipitates associated with twin boundaries.

Small circular pits ~1-2 μm in size, but not lying on any crystal grain boundaries, were revealed after etching times of ~ 1 minute. On continued etching these pits were seen to grow, reaching a size of up to 10 μm, before becoming indistinct (or blurred). An example is shown in figure 5.5. This type of pit on investigation

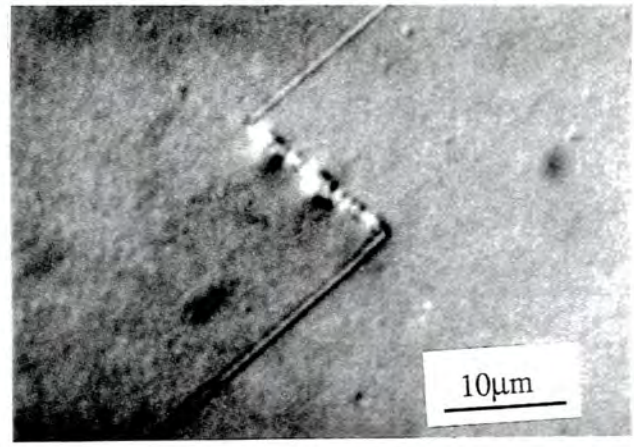

(a)

(b)

Figure 5.4 Precipitates decorating a first order lateral twin boundary as revealed by (a) ferric chloride etching and (b) IR microscopy.

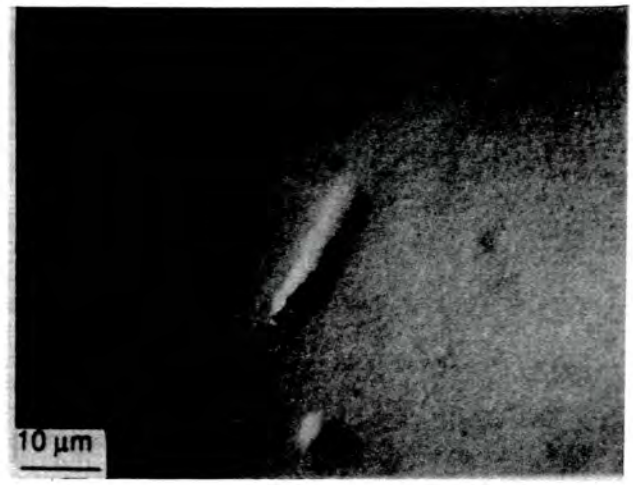

Figure 5.5 Precipitates in (111)A $Cd_{0.96}Zn_{0.04}Te$ revealed by ferric chloride defect etching.

produced a similar EDAX result to that shown in figure 4.7 (see section 4.3.2) indicating the occurrence of Te precipitation. The occurrence of Te precipitates of this size was reported to be independent of whether a Cd or Te excess was used during growth [16]. Pits of this nature were also correlated with precipitates observed in IR microscopy. The observed blurring of these pits (figure 5.5) was assumed to be due to the defect being totally etched through, leaving a shadow of the original feature. The figure shows such an example on the (111)A face of $Cd_{0.96}Zn_{0.04}Te$, where a line of precipitates penetrating to the surface has been etched, developing a row of 10 pits ranging in size from < 1 μm to 4 μm. The larger blurred pits replicate precipitates completely etched out of the material, whereas the smaller pits, with a sharper appearance, indicate precipitates penetrating the crystal surface. The smallest pit in figure 5.5 was developed after ~8 minutes etching, therefore figure 5.5 shows a line of precipitates penetrating through a 16μm slice of substrate. The ability of the ferric chloride etch to profile through defects leaving a shadow of the original feature is expected to make it of value in obtaining estimates of volume densities of defects, e.g. the volume density of precipitates in figure 5.5 is ~ 1 x 10^2 cm^{-3}.

Cathodoluminescence studies revealed an excellent correlation between spots of very dark contrast and etch pits developed at Te precipitates, as imaged using optical and scanning electron microscopes. Such correlations were observed on the (111) A and $(\bar{1}\bar{1}\bar{1})$B faces of CdTe, and the (111) A and $(\bar{1}\bar{1}\bar{1})$B faces of (Cd,Zn)Te. Figures 5.6a and 5.6b show this correlation for $(\bar{1}\bar{1}\bar{1})$B CdTe and figures 5.7a and 5.7b show a similar correlation for $(\bar{1}\bar{1}\bar{1})$B $Cd_{0.96}Zn_{0.04}Te$ (The strong CL contrast observed being expected due to elemental Te having a nearly infinite surface recombination velocity, and hence acting as a non-radiative recombination centre as discussed in section 4.4). Examinations of the shape of these pits after 2-3 minutes of etching indicated the majority to be triangular in shape (figure 5.8) but others appeared as hexagons as shown in figure 5.9. On close examination the triangular pits were observed to have a tetrahedral nature, this being clearly seen in the S.E.M micrograph shown in figure 5.8. The tetrahedral shape was observed on both the (111)A and $(\bar{1}\bar{1}\bar{1})$B faces for both CdTe and $Cd_{0.96}Zn_{0.04}Te$. (Figure 5.8 shows a pit on $(\bar{1}\bar{1}\bar{1})$B $Cd_{0.96}Zn_{0.04}Te$, however examples of tetrahedral pits developed on (111)A $Cd_{0.96}Zn_{0.04}Te$ are shown in figure 5.5) .This is in contrast to the action of Inoue's EAg-1 reagent as reported by Durose [17], in this case small pyramidal triangular pits, similar to those developed by ferric chloride, were observed on {111} Cd faces whereas large flat bottomed triangular pits were developed on {111}Te faces. The difference was accounted for

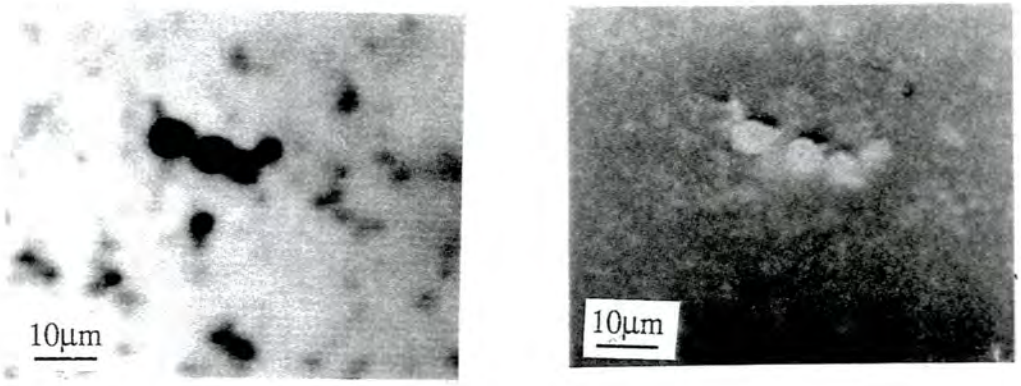

(a) (b)

Figure 5.6 Correlation between precipitates observed in $(\bar{1}\bar{1}\bar{1})$B CdTe by (a) CL and (b) SEM, after ferric chloride defect etching.

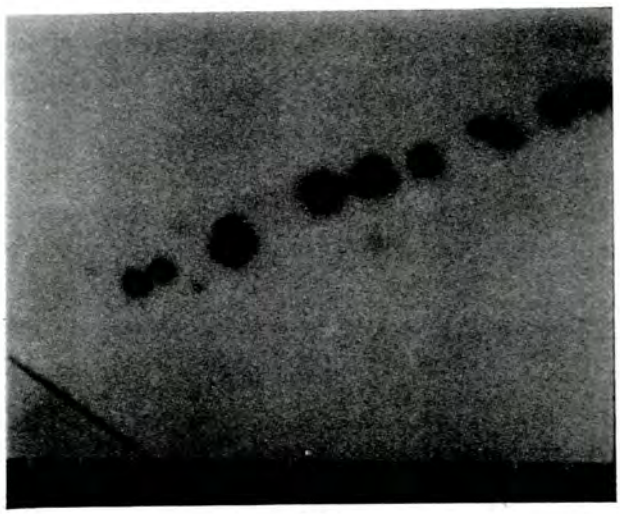

(a)

(b)

Figure 5.7 Correlation between precipitates observed in $(\bar{1}\bar{1}\bar{1})$B $Cd_{0.96}Zn_{0.04}Te$ by (a) CL and (b) SEM, after ferric chloride defect etching.

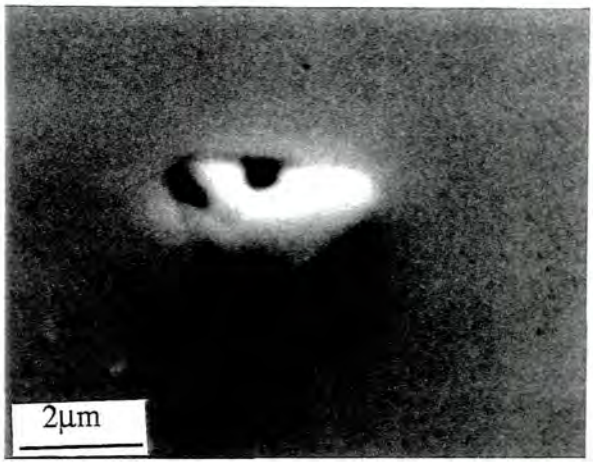

Figure 5.8 SEM micrograph of tetrahedral etch pit developed at a precipitate in $(\bar{1}\bar{1}\bar{1})$B $Cd_{0.96}Zn_{0.04}Te$ after ferric chloride etching.

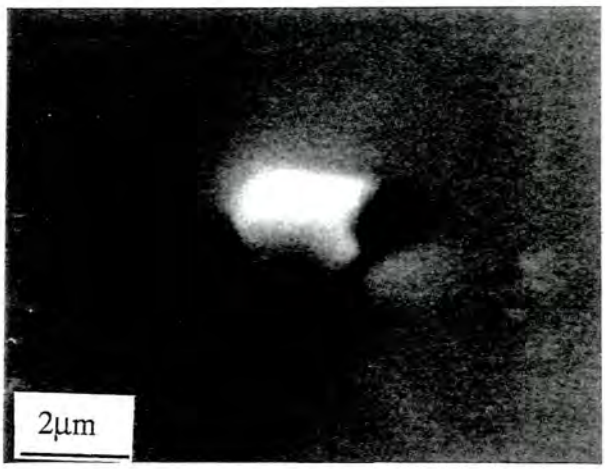

Figure 5.9. SEM micrograph of a hexagonal etch pit developed at a precipitate in $(\bar{1}\bar{1}\bar{1})$B $Cd_{0.96}Zn_{0.04}Te$ after ferric chloride etching.

by an anisotropic etch rate, with the {111}Te surfaces being etched at a higher rate than the {111} Cd surfaces. The shape of etch pits on {111} polar faces in the sphalerite structure has been reviewed by Holt [18]. The etch rate of ferric chloride however, as already reported, is virtually identical on the (111)A and $(\bar{1}\bar{1}\bar{1})$B faces, thus providing a likely explanation for the similarity in shape of etch pits observed on these faces.

5.4.3 Dislocations

Loose networks of small, 1-2 μm, circular pits consistent with the presence of dislocation arrays (or sub-grain boundaries) were observed on (111)A and $(\bar{1}\bar{1}\bar{1})$B faces of both CdTe and $Cd_{0.96}Zn_{0.04}Te$ after ~1 minute of ferric chloride etching. Figure 5.10 shows a typical network on the (111)A face of a (Bridgman grown) CdTe sample, revealing an average etch pit density of $\sim 5 \times 10^4$ cm^{-2}, and figure 5.11 shows a pit density of 3×10^4 cm^{-2} on the $(\bar{1}\bar{1}\bar{1})$B face of a different CdTe sample. These etch pit densities compare favourably with pit densities revealed on similar material by the Nakagawa solution [16,19,20]. The occurrence and nature of sub-grain boundaries observed, by ferric chloride etching and CL microscopy, in CdTe and (Cd,Zn)Te samples is discussed in depth in section 6.2.1.

Ferric chloride etching also revealed dislocations in epitaxial (Cd,Hg)Te. In figure 5.12 an etch pit density of 1×10^5 cm^{-2} is revealed on the $(\bar{1}\bar{1}\bar{1})$B surface of a 18μm thick $Cd_{0.24}Hg_{0.76}Te$ epilayer.

The etch pits developed at precipitates in CdTe and (Cd,Zn)Te and those assumed to represent dislocations may be distinguished by both their shape and size. After 2-3 minutes of etching pits thought to represent dislocations were still circular and typically 1-3 μm in size, e.g as at A in figure 5.13, whereas those developed at precipitates were typically 5-20 μm in size, e.g at B in figure 5.13. On close examination of pit B a tetrahedral nature is also apparent.

A key aim of the work was to establish the validity of the ferric chloride etching in revealing dislocations on the $(\bar{1}\bar{1}\bar{1})$B surface so enabling the etch to be used in the calculation of dislocation densities. At locations where rosettes of dislocations were visible (e.g at Cd precipitates shown in figures 6.15 in Section 6.2.2) a general correlation between the etch pits and CL contrast delineating the individual arms

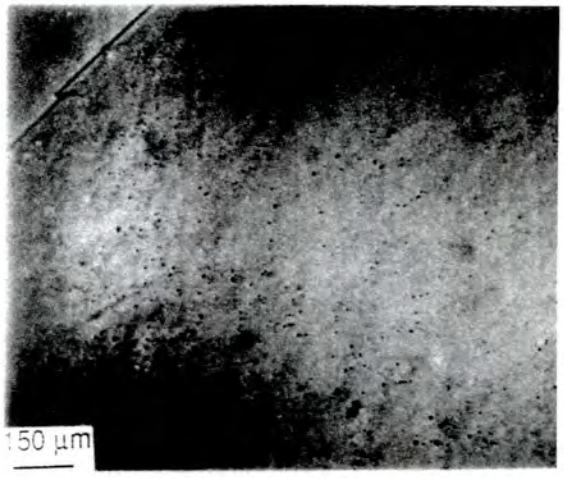

Figure 5.10 Etch pits developed on (111)A CdTe by ferric chloride etching.

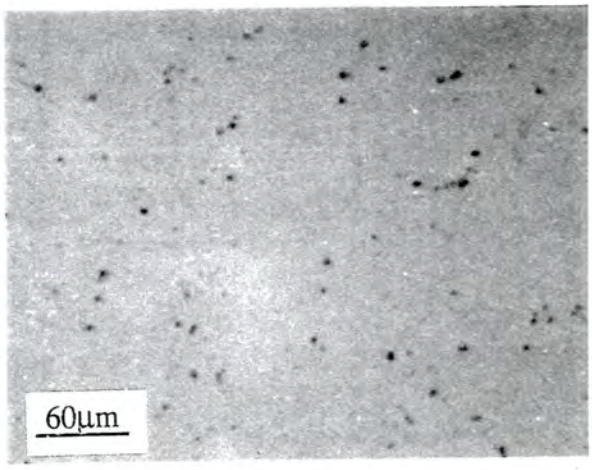

Figure 5.11 Etch pits developed on $(\bar{1}\bar{1}\bar{1})$B CdTe by ferric chloride etching.

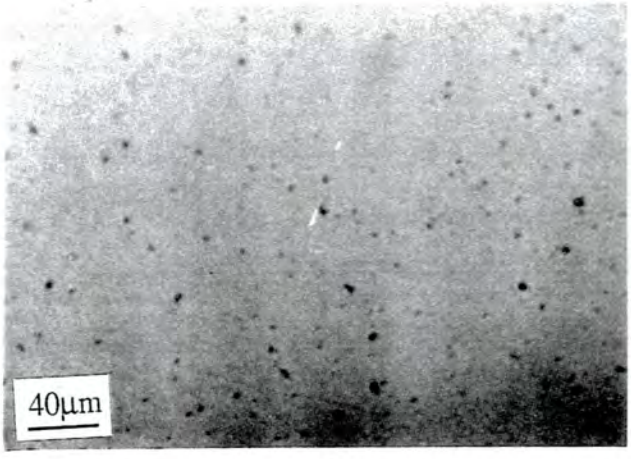

Figure 5.12 Etch pits developed on $(\bar{1}\bar{1}\bar{1})$B $Cd_{0.24}Hg_{0.76}Te$ by ferric chloride etching.

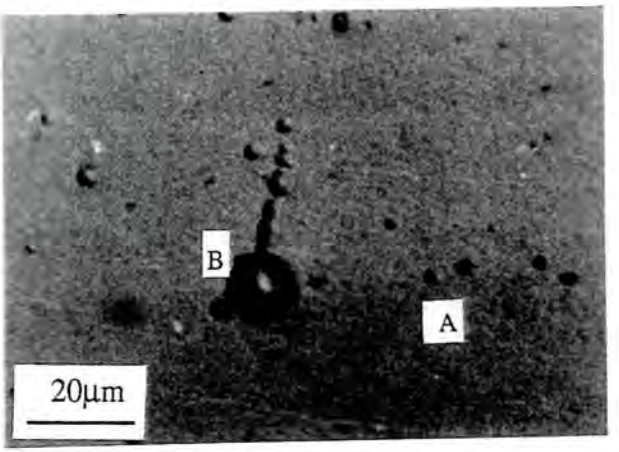

Figure 5.13 Comparison of etch pits developed at dislocations (A) and precipitates (B) on $(\bar{1}\bar{1}\bar{1})$ B CdTe by ferric chloride etching.

was possible. However, because of the high density of defects located in these rosettes, ~10^{10} cm^{-2}, a 1:1 correlation between individual defects was impossible as individual dislocations were not resolvable in CL (see figure 6.15). Where individual pits and dark CL spots were visible experiments to determine a 1:1 relationship still proved to be non trivial with three main difficulties arising:-

1. CL was seen to reveal a higher number of features than that disclosed by etching (compare figure 5.14a and figure 5.14b which are micrographs of features on the $(\bar{1}\bar{1}\bar{1})$B face of CdTe), due to the penetration of the electron beam, e.g a 25 kV electron beam penetrates ~ 3.5μm into CdTe [22]. A similar difficulty was encountered in attempts to correlate EBIC results with etch pits [23].
2. Etching times of ~2 minutes removed approximately 4-5 μm of material, thus only pits developed at dislocations penetrating normal to the {111} surfaces were seen to have the same x-y co-ordinates as CL spots, imaged before etching and representing identical dislocations.
3. On comparison of figures 5.14a and 5.14b CL microscopy was observed to have a lower resolution than that obtained by ferric chloride etching, e.g in the dense cluster of etch pits in figure 5.14b, individual features are resolved but no individual features are visible in the corresponding area of figure 5.14a.

A full correlation of all etch pits with dark spots was therefore not expected, however at sample areas decorated by a lower pit density, examples of 1:1 correlations were observed. For instance in figures 5.14a and 5.14b the features labelled A-C appear at identical locations in the two micrographs. Thus the ability of

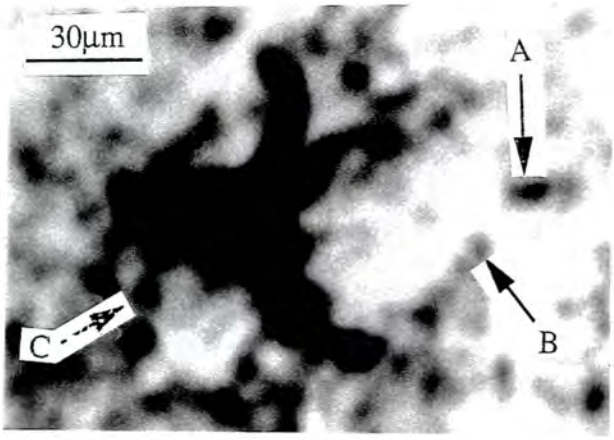

(a)

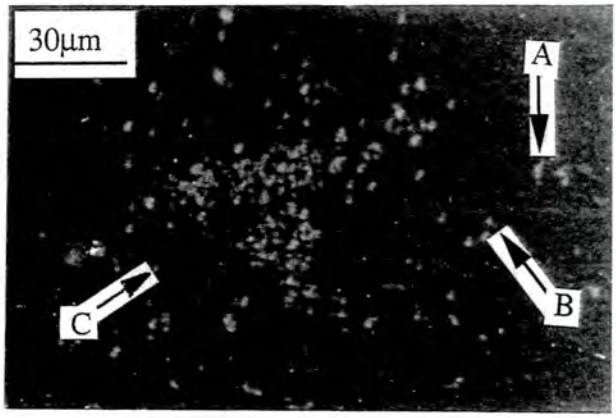

(b)

Figure 5.14 Correlation between dislocations on $(\bar{1}\bar{1}\bar{1})$B CdTe as revealed by (a) CL and (b) ferric chloride etching.

the ferric chloride reagent to develop pits at dislocations is proved on the $(\bar{1}\bar{1}\bar{1})$B face of CdTe.

5.5 Chemistry of Etching Reaction

Although the chemistry of the dissolution process has not been systematically investigated here it may proceed as follows [13]; $FeCl_3$ is hydrolysed in aqueous solution and the species below are in equilibrium (all with coordinated water and/or chloride ions) [23],

$$FeCl_3 \overset{H_2O}{\underset{+HCl}{\rightleftharpoons}} FeCl_2(OH) \overset{H_2O}{\underset{+HCl}{\rightleftharpoons}} FeCl(OH)_2 \overset{H_2O}{\underset{+HCl}{\rightleftharpoons}} Fe(OH)_3$$

$$2Fe(OH)_3 \equiv Fe_2O_3 + 3H_2O \quad \text{, the latter being rust}$$

$FeCl_3$ thus forms a brown acidic 'solution' (a colloidal dispersion of $Fe_2O_3.xH_2O$). The etching of CdTe may then proceed by the dissolution of Cd^{2+} as $CdCl_2$ (aq).The oxidation of Te^{2-} proceeds in the presence of HCl (aq) perhaps with the assistance of atmospheric oxygen, to give Te^{4+} as $TeCl_4$. In HCl (aq) $TeCl_4$ is complexed as $TeCl_5H_2O^-$ and $TeCl_6^{2-}$ and these species are in equilibrium with their hydrolysis products, e.g.

$$TeCl_4 \overset{H_2O+HCl}{\rightleftharpoons} H_3O^+\, TeCl_5^- \overset{H_2O+HCl}{\rightleftharpoons} (H_3O^+)_2\, TeCl_6^{2-}$$

$$TeCl_4 \overset{H_2O}{\underset{+HCl}{\rightleftharpoons}} TeCl_3OH \overset{H_2O}{\underset{+HCl}{\rightleftharpoons}} TeCl_2(OH)_2 \overset{H_2O}{\underset{+HCl}{\rightleftharpoons}} TeCl(OH)_3 \overset{H_2O}{\underset{+HCl}{\rightleftharpoons}} Te(OH)_4$$

In the event that the surface of the crystal is oxidised prior to etching or else by dissolved oxygen the stable oxide will be TeO_2. This is soluble in acidic solution:-

$$TeO_2 \overset{HCl}{\rightleftharpoons} TeCl_4 + 2H_2O$$

As HCl is consumed during the reaction Fe_2O_3 is plated out onto the crystal surface and this is observed in practice.(e.g in the vicinity of the precipitate in the IR micrograph shown in figure 6.14a).

These processes or related ones may account for the solvation of Cd and Te species. However the role of Fe itself in the etching remains unclear. Fe_2O_3 is observed to be plated out during the reaction but its involvement in the selective etching or oxidation process has not been determined.

5.6 Conclusions

The suitability of an etching reagent as a defect etch is governed by two criteria; the ability to reproducibly develop etch pits on all crystal faces of interest and an observation of a relationship between different types of etch pit and specific crystal defects. It is hoped that the results presented in this chapter have satisfied both, the ferric chloride etch being shown to develop pits on a range of crystal orientations and a direct relationship found between twin boundaries, precipitates and dislocations, and different types of etch pit. The ability of the etch to reveal dislocations on the $(\bar{1}\bar{1}\bar{1})$B surface of CdTe is of particular value, this being the substrate orientation upon which LPE films of (Cd,Hg)Te are grown. No other etch has been shown to work successfully on this technologically important surface. The etch also successfully develops etch pits on epitaxial (Cd,Hg)Te and thus dislocation densities in both a layer and its substrate may be simultaneously calculated. The etch pit densities in bulk CdTe and epitaxial (Cd,Hg)Te compare closely with dislocation densities observed in similar material after etching with the Nakagawa and Hähnert solutions respectively.

Other features, such as a linear etch rate of ~2 μm $minute^{-1}$, on {111} surfaces, enabling the profiling of defects and the calculation of volume defect densities, and the high resolution definition of individual defects, enable the use of the etch as a powerful characterisation tool. In Chapter 6, ferric chloride etching results are employed with those obtained from the complementary CL and EBIC techniques, in fully characterising as-grown defects in CdTe and $Cd_{0.96}Zn_{0.04}Te$ samples cut from substrate quality boules.

The etch however does have potential drawbacks. The major limitation is the relatively long etching time needed to develop clear and distinguishable pits. Etching times of 2-3 minutes were common, with in some instances periods of 7 or 8 minutes being employed. Periods of this length lead to the removal of several microns of material from the exposed surface (e.g 3 minutes etching corresponded

to a removal of ~6 μm), making the etch unsuitable for use on thin slices, or films, < 4-5 μm in thickness. A further limitation of this etchant is that it contains iron which is sometimes plated out onto the etched surface as Fe_2O_3. Iron would therefore be incorporated into substrates which is undesirable for material which is to be used for device fabrication. As with many defect etchants the development of pits may also be temperature dependent; the temperature dependence of the ferric chloride solution was not examined in this work.

REFERENCES FOR CHAPTER FIVE

1. K. Nakagawa, K. Maeda and S.Takeuchi, Appl. Phys. Lett. **34** (1979) 574.
2. M. Inoue, I. Teramoto and S. Takayanagi, J. Appl. Phys. **33** (1962) 2578.
3. D.J. Williams, private communication.
4. J-S. Chen, United States Patent No. 4,897,152, Etchant for Revealing Dislocations in II - VI compounds, (1990).
5. I. Hähnert and M. Schenk, J. Crystal Growth. **101** (1990) 251.
6. E.L. Polisar, N.M. Boinikh, G.V. Indenbaum, A.V. Vanyukov and V.P. Shastlivin, Izv. Vyshch. Uchebn. Zaved. Fiz. **6** (1988) 81.
7. P.D. Brown, K. Durose, G.J. Russell and J.Woods, J.Crystal Growth **101** (1990) 211.
8. G.Brandt, H. Ennen, R. Moritz and W. Rothemund, J. Crystal Growth. **101** (1990) 226.
9. Y-C. Lu, R.K. Route, P. Elwell and R.S. Feigelson, J. Vac. Sci. Technol. **3** (1985) 264.
10. K. Durose, Ph.D Thesis, University of Durham, 1986.
11. B.Tuck, J. Mat. Sci. **10** (1975) 321.
12. K. Sangwall, 'Etching of solids', (North Holland, Amsterdam, 1987).
13. C.C.R. Watson, K. Durose, A.J. Banister , E. O'Keefe and S.K. Bains, Mat. Sci. Eng. **B16** (1993) 113.
14. K. Durose and G.J. Russell, J. Crystal Growth **101** (1990) 251.
15. see for example: K. Durose and G.J Russell, J. Crystal Growth **86** (1988) 471.
16. P. Capper, J.E. Harris, E. O'Keefe, C.L. Jones, C.K. Ard, P. Mackett and D. Dutton, Mat. Sci. Eng. **B16** (1993) 29.
17. K. Durose, G.J. Russell and J.Woods, Inst. Phys. Conf. Ser. **72** (1985) 272.
18. D.B. Holt, J. Mat. Sci. **23** (1988)1131.
19. M. Yoshikawa, J. Appl. Phys. **63** (1988) 1533.
20. S.Sen, W.H. Konkel, S.J. Tighe, L.G. Bland, S.R. Sharma and R.G. Taylor, J. Crystal Growth. **86** (1988) 111.
21. K. Kanaya and S. Okayama, J. Phys. D (Appl. Phys). **5** (1972) 43.
22. M. Wada, J. Suyuchi and H. Hosomatsu, Jap. J. Appl. Phys. **25** (1986) L780.
23. J.C. Bailor (Ed.), Comprehensive Inorganic Chemistry Vol 1, (Permagon Press, Oxford, 1973).

CHAPTER SIX

Structural Defects in Bulk CdTe

6.1 Introduction

In the two preceding chapters the suitability of CL microscopy and a ferric chloride etching solution as characterisation tools for bulk CdTe has been examined. In this chapter these two techniques are employed, in conjunction with IR microscopy and triple axis X-ray diffraction to examine the structural quality of substrates cut from melt grown boules of CdTe and (Cd,Zn)Te. The CdTe boules assessed have been grown by the Bridgman technique with and without the ACRT modification [1]. The (Cd,Zn)Te samples examined were obtained from boules grown by a modified Bridgman technique (by the Nippon Mining Co.), in which a Cd overpressure is maintained by use of a Cd reservoir [2]. (Although ACRT (Cd,Zn)Te is grown by G.E.C Marconi, at Southampton, no boules of this material were available for this work.) The structural quality of the substrates, i.e their dislocation, sub-grain boundary and precipitate content, is compared with results reported in the literature.

In order to compare the quality of vapour grown boules with those obtained from the melt, the defect content of a CdTe boule grown from the vapour by the 'Durham' [3] technique has also been examined.

6.2 Structural Defects in Bridgman Grown CdTe and (Cd,Zn)Te

The samples examined in this section were all cleaved from 2 x 3 cm substrates cut from large grains with a {111} orientation, located in the boules by the Laue back reflection X-ray technique. The {111} surface investigated in each case was the Te or $(\bar{1}\bar{1}\bar{1})$B face, identified by etching using a solution containing CH_3OOH, HF and HNO_3 [4]. The substrates where possible were cut from crystal areas devoid of twins therefore the occurrence of twinning in Bridgman grown material is not examined in this chapter.

6.2.1 Dislocations and sub-grain boundaries

Ferric chloride etching of a number of ACRT CdTe crystals revealed an average etch pit density in the range 3-5 x 10^4 cm^{-2} (figures 6.1a and 6.1b show etch pit densities of ~ 4.5 x 10^4 cm^{-2} and ~ 3 x 10^4 cm^{-2} respectively), with the lowest and highest densities observed being 2 x 10^4 cm^{-2} and 7 x 10^4 cm^{-2} (see figures 7.2e and 5.11). No relationship was found between the etch pit density and the starting material composition (i.e initial growth with 0.5% Cd excess, 1% Te excess or no excess). CL microscopy of identical samples revealed ACRT material to contain a cellular dislocation structure with an average sub-grain size of 60-100 μm (figure 6.2), however on some occasions cells up to ~150 μm in size were observed, i.e. in figure 6.3. (Additional CL micrographs showing sub-grain networks in ACRT CdTe are shown in figures 4.1a and 4.11). Few dislocations were visible inside the cells and the separation between dislocations forming the sub grain boundaries was typically 6μm. From such a dislocation separation a sub-grain misorientation of 17 arcseconds may be calculated, if it is assumed that the dislocations have a Burgers vector a/2<110> and obey the relationship $\theta \sim b / D$. The structural defect contents of the boules examined are tabulated in table 6.1.

For non-ACRT CdTe an average etch pit density of 9 x 10^4 - 2 x 10^5 cm^{-2} was calculated (figure 6.4), and CL microscopy (figure 6.5) revealed a distinct sub-grain network with an average cell size of 30μm. The average dislocation separation in the sub-grain boundaries shown in figure 6.5 is 4μm, from which a sub-grain misorientation of 26 arcseconds may be calculated.

Substrates cut from a boule of $Cd_{0.96}Zn_{0.04}Te$ grown by a modified Bridgman technique utilising a Cd reservoir were also examined. Ferric chloride etch pit densities of 3-5 x 10^4 cm^{-2} were also observed (figure 6.6 shows a density of ~ 4.7 x 10^4 cm^{-2}), however CL microscopy revealed a less distinct cellular dislocation structure compared to ACRT CdTe (figure 6.7), although cells ranging from 100-150 μm in size were visible. The dislocation separation in the sub-grain boundaries was ~15μm (figure 6.8) from which a tilt of 6 arcseconds was calculated. As in ACRT CdTe few dislocations were observed within the sub-grain cells.

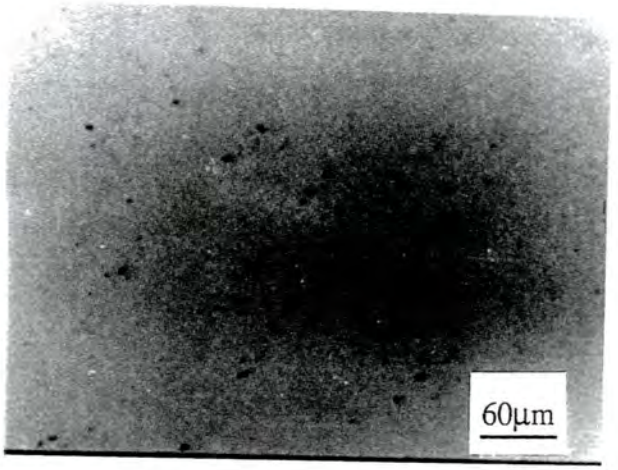

(a)

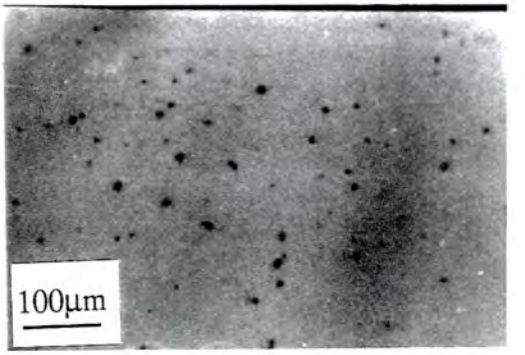

(b)

Figure 6.1 Ferric chloride etch pits on $(\bar{1}\bar{1}\bar{1})$B ACRT CdTe, illustrating the range in dislocation density across a wafer; i.e. optical micrographs showing etch pit densities of (a) ~ 4.5 x 10^4 cm^{-2} and (b) ~ 3 x 10^4 cm^{-2}.

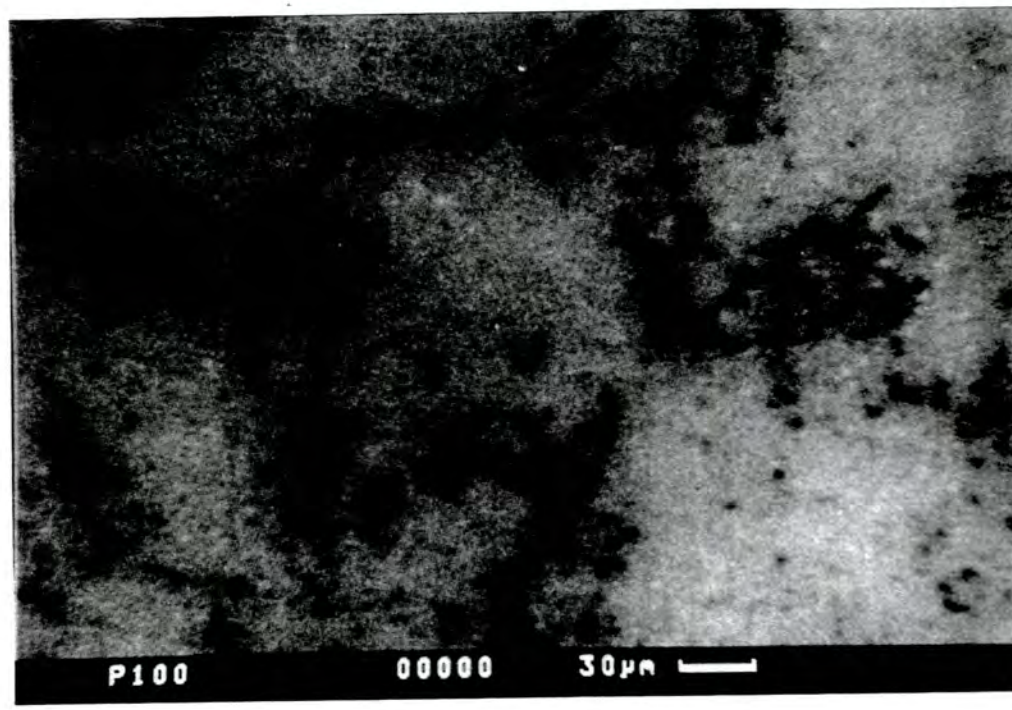

Figure 6.2 Sub-grain boundaries in ACRT CdTe revealed by CL.

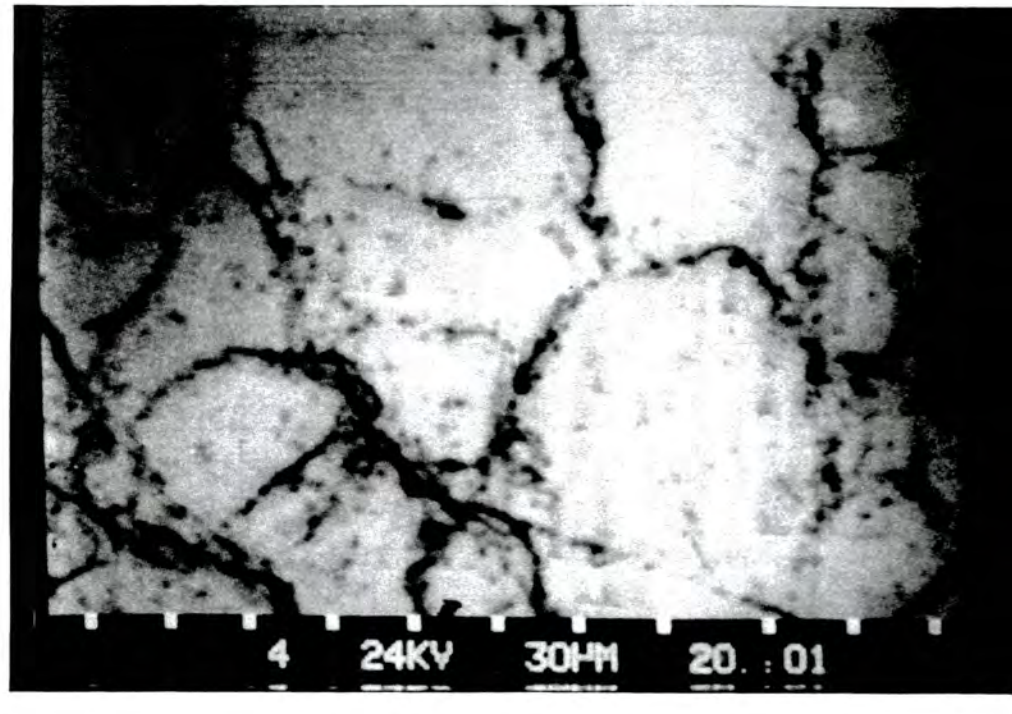

Figure 6.3 Sub-grain boundaries in ACRT CdTe, showing sub-grain cells up to ~ 150µm in size.

Figure 6.4 Ferric chloride etch pits on $(\bar{1}\bar{1}\bar{1})$B non-ACRT CdTe, showing an average etch pit density of ~ 1 x10^5 cm^{-2}.

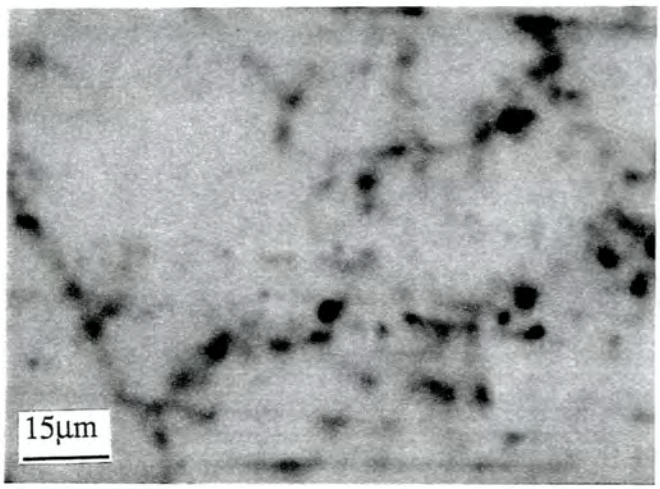

Figure 6.5 Sub-grain boundaries in non-ACRT CdTe revealed by CL.

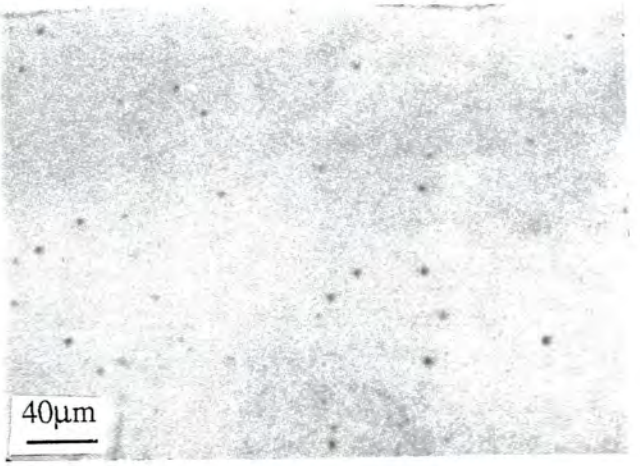

Figure 6.6 Ferric chloride etch pits on $(\bar{1}\bar{1}\bar{1})$ B $Cd_{0.96}Zn_{0.04}Te$, showing an average etch pit density of ~ 4.7 x 10^4 cm^{-2}.

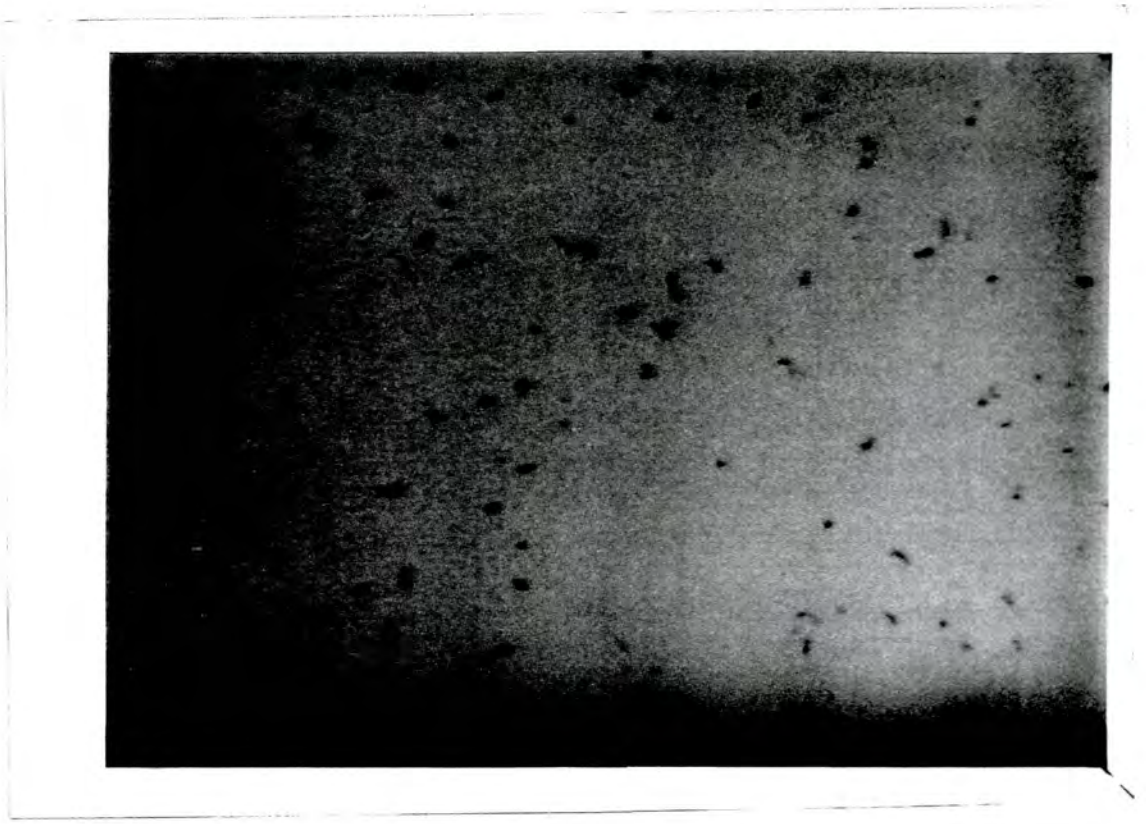

Figure 6.7 Sub-grain boundaries in $Cd_{0.96}Zn_{0.04}Te$ revealed by CL.

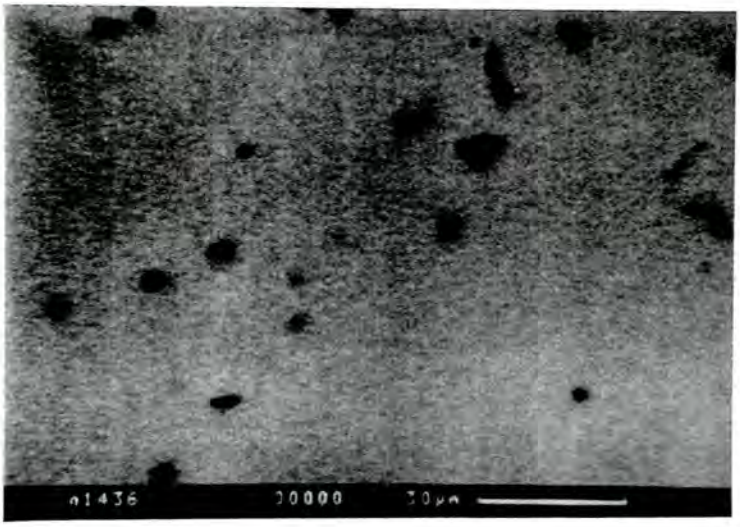

Figure 6.8 Individual dislocations forming sub-grain boundaries in $Cd_{0.96}Zn_{0.04}Te$ revealed by CL.

Typical triple axis reciprocal space maps for the $Cd_{0.96}Zn_{0.04}Te$ and ACRT CdTe examined in this work are shown in figures 6.9a and 6.9b. In both cases the maps are steeper in the ΔQ_y (tilt) axis indicating a greater contribution to the total rocking curve width from mosaic tilt compared with lattice dilation. Quantitative triple axis analysis indicated an average tilt of 8 arcseconds in the $Cd_{0.96}Zn_{0.04}Te$ substrates examined, compared with an average tilt of 26 arcseconds for ACRT CdTe. Average FWHM's of 9 and 11 arcseconds were obtained from lattice dilation rocking curves for (Cd,Zn)Te and ACRT CdTe and total rocking curve widths (i.e standard DCXRD FWHM) of 17 and 32 arcseonds respectively, were also calculated. No reproducible X-ray rocking curves were obtainable for the non-ACRT CdTe samples examined and the 40 arcsecond and 17 arcsecond values for the substrate tilt and lattice dilations, given in Table 6.1 for this material are those reported by Capper et al [1] for similar material.

In ACRT CdTe samples obtained from a boule grown from a 0.5% Cd excess, patterns of etch pits forming two equilateral triangles were observed, the triangles being rotated by 180° with respect to each other as shown in figure 6.10. The edges of the triangle were identified as lying parallel to <110> directions. Similar triangles were observed by CL, the micrograph in figure 6.11 showing lines of contrast forming an equilateral triangle of side length ~ 100 μm, within which are another three lines of contrast, with a separation of 120°, propagating from a common point. It is shown in section 6.2.3 that these features are dislocation arrays associated with Cd precipitates.

	CdTe (A.C.R.T)	CdTe (non-A.C.R.T)	$Cd_{0.96}Zn_{0.04}Te$
Dislocation Density (cm^{-2}) (revealed by ferric chloride etching)	3-5 x 10^4	9 x 10^4 - 2 x 10^5	3-5 x 10^4
Sub-grain Cell Size (μm) (from CL micrographs)	60 - 100	30	100 - 150
Precipitate Density (cm^{-2}) (revealed by I.R. microscopy)	0 - 30 x 10^2	5 - 30 x 10^2 (from ref [1])	1 x 10^4
Substrate Tilt from X-ray rocking curve (arcseconds)	8	40 (from ref [1])	26
Substrate Dilation from X-ray rocking curve (arcseconds)	11	17 (from ref [1])	12

Table 6.1 Structural Defect Content in Substrate Materials

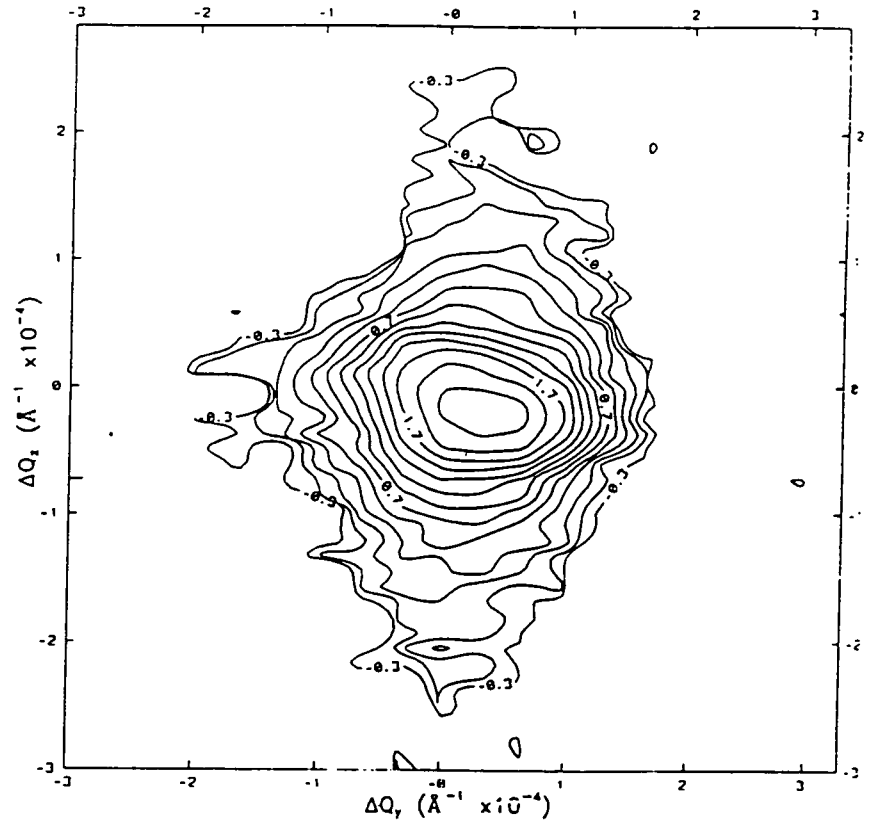

(a)

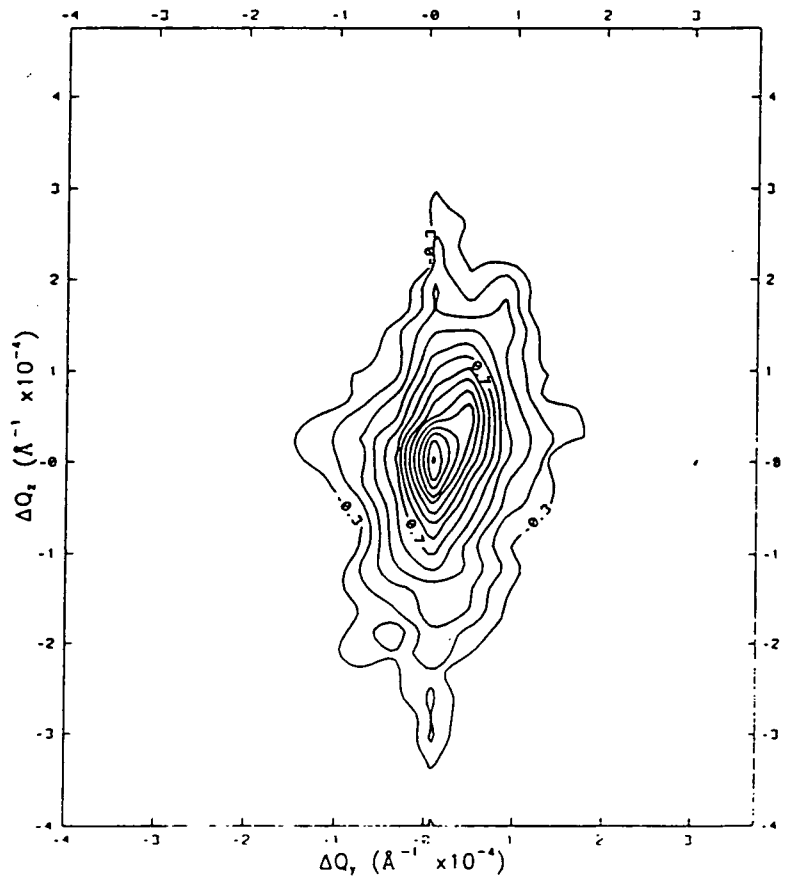

(b)

Figure 6.9 Triple axis X-ray diffraction reciprocal space maps of (a) ACRT CdTe and (b) $Cd_{0.96}Zn_{0.04}Te$ substrates.

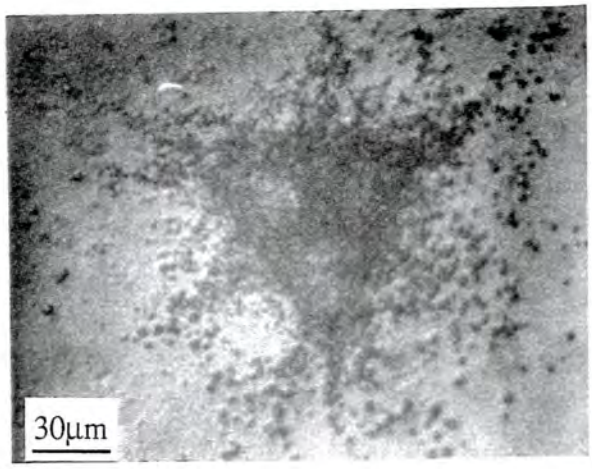

Figure 6.10 Triangular (ferric chloride) etch pit network in ACRT CdTe in the vicinity of a Cd precipitate. The precipitate is out of the plane of the micrograph.

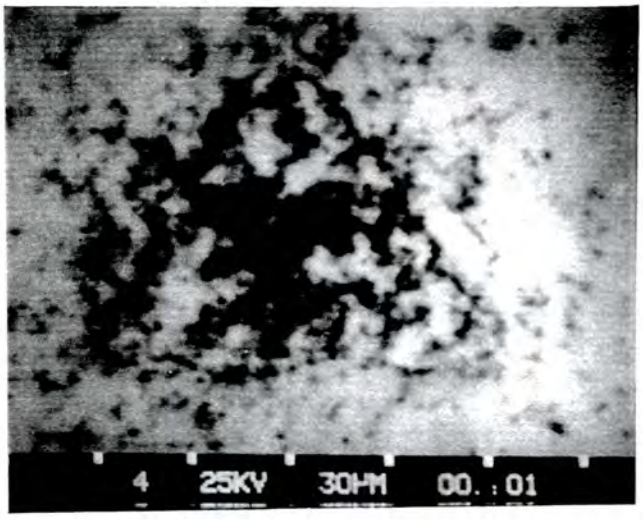

Figure 6.11 CL micrograph of a dislocation triangle in ACRT CdTe in the vicinity of a Cd precipitate

6.2.2 Precipitates

Te precipitates, identified by EDAX (see figure 4.9) were examined using a polarising I.R microscope. They were present in all the CdTe and (Cd,Zn)Te boules examined in this work, regardless of whether growth was from stoichiometric, Te rich or Cd rich conditions. ACRT CdTe crystals revealed a precipitate density range of 0 - 30 x 10^2 cm^{-2}, these Te precipitates being < 5μm in size. A higher precipitate density of typically ~ 1 x 10^4 cm^{-2} was observed in $Cd_{0.96}Zn_{0.04}Te$ samples grown using a Cd overpressure, the precipitates again being < 5μm in size. The increased precipitate content in the $Cd_{0.96}Zn_{0.04}Te$ boules examined may be clearly seen on comparison of the I.R. micrographs shown in figures 6.12 and 6.13. The former shows a typical Te precipitate distribution in ACRT CdTe whereas the latter is an example of the distribution commonly observed in $Cd_{0.96}Zn_{0.04}Te$. The precipitate content of non-ACRT CdTe crystals, grown at G.E.C Marconi, was not examined in this work but a precipitate density of 5-30 x 10^2 cm^{-2} has previously been reported for this material [1], with larger inclusions > 10 μm also being observed.

In ACRT CdTe boules grown under a 0.5% Cd overpressure, larger precipitates ~ 40μm in diameter were also observed by I.R microscopy, (e.g the precipitate in figure 6.14a), such features being characterised by a 'star' shaped appearance. On examination by CL microscopy (figure 6.14b) and ferric chloride etching (6.14c and 6.14d), these defects were revealed to consist of a central inclusion from which arms of etch pits or dark CL spots propagate every 60^o, the arms lying parallel to <110> directions. EDAX analysis (figure 6.15) of such features indicated a higher Cd : Te ratio at the precipitate compared to the CdTe bulk, thus indicating the precipitate to be Cd or at least Cd rich. In section 6.2.3 it is shown that these precipitates are the cause of the triangular dislocation patterns shown in figure 6.10 and figure 6.11.

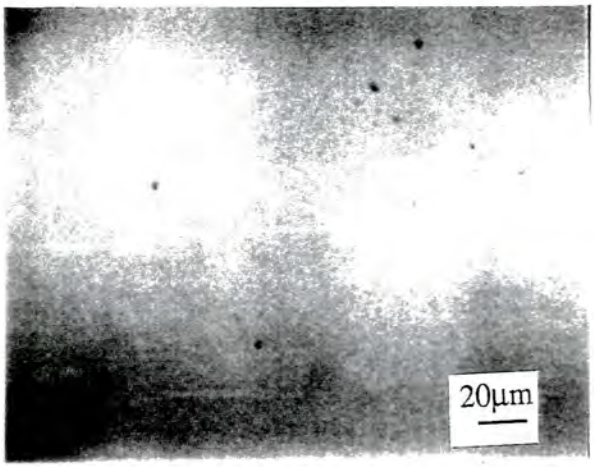

Figure 6.12 Infra-red micrograph of Te precipitates in ACRT CdTe.

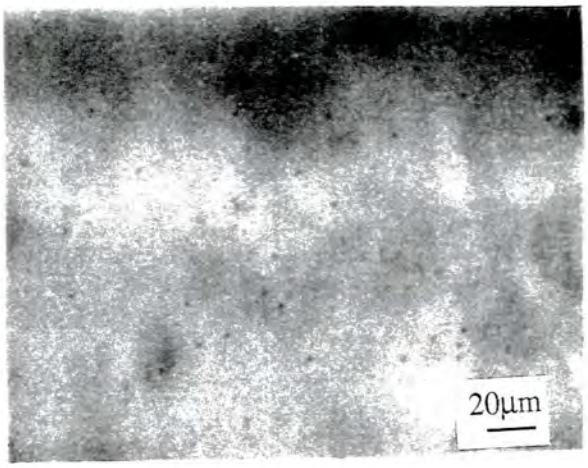

Figure 6.13 Infra-red micrograph of Te precipitates in $Cd_{0.96}Zn_{0.04}Te$ grown under a Cd overpressure.

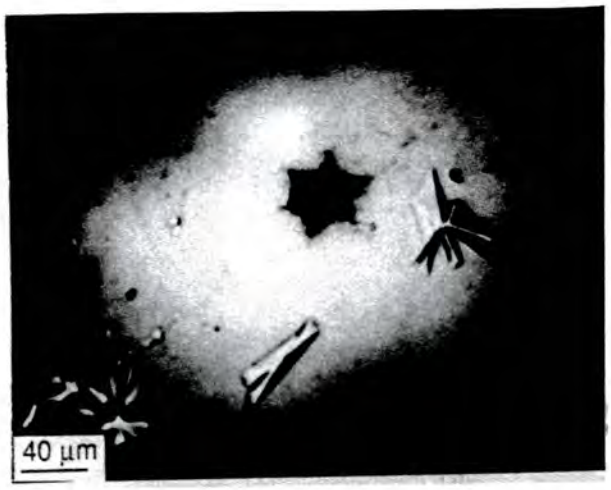

(a)

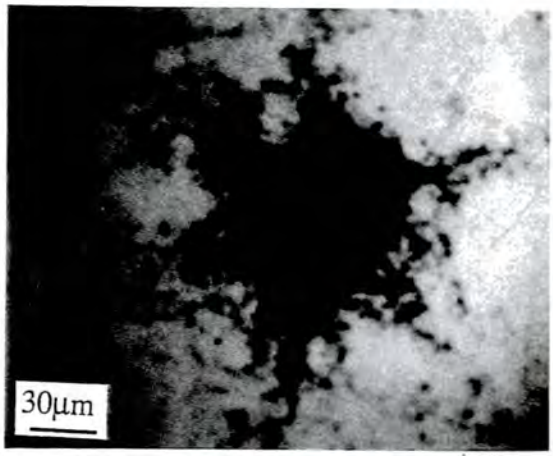

(b)

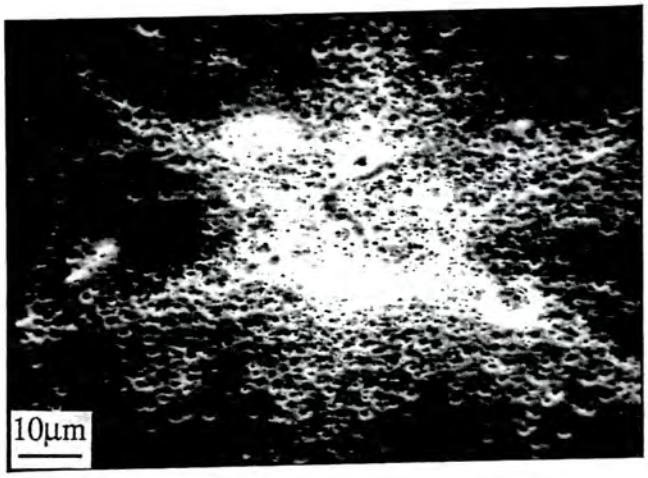

(c)

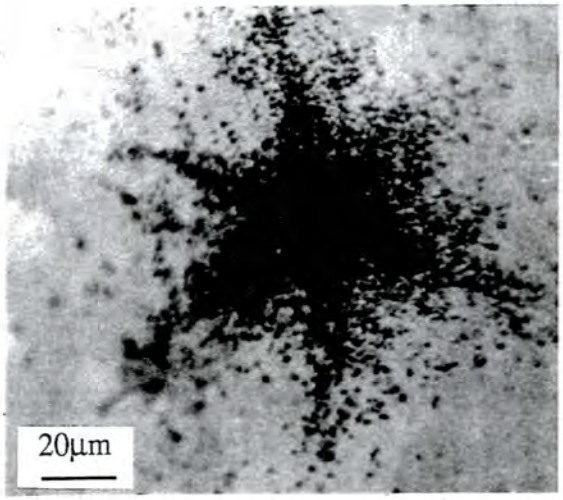

(d)

Figure 6.14 Cd precipitate in ACRT CdTe, as observed by (a) I.R microscopy, (b) CL (c) SEM, after ferric chloride etching and (d) optical microscopy after ferric chloride etching.

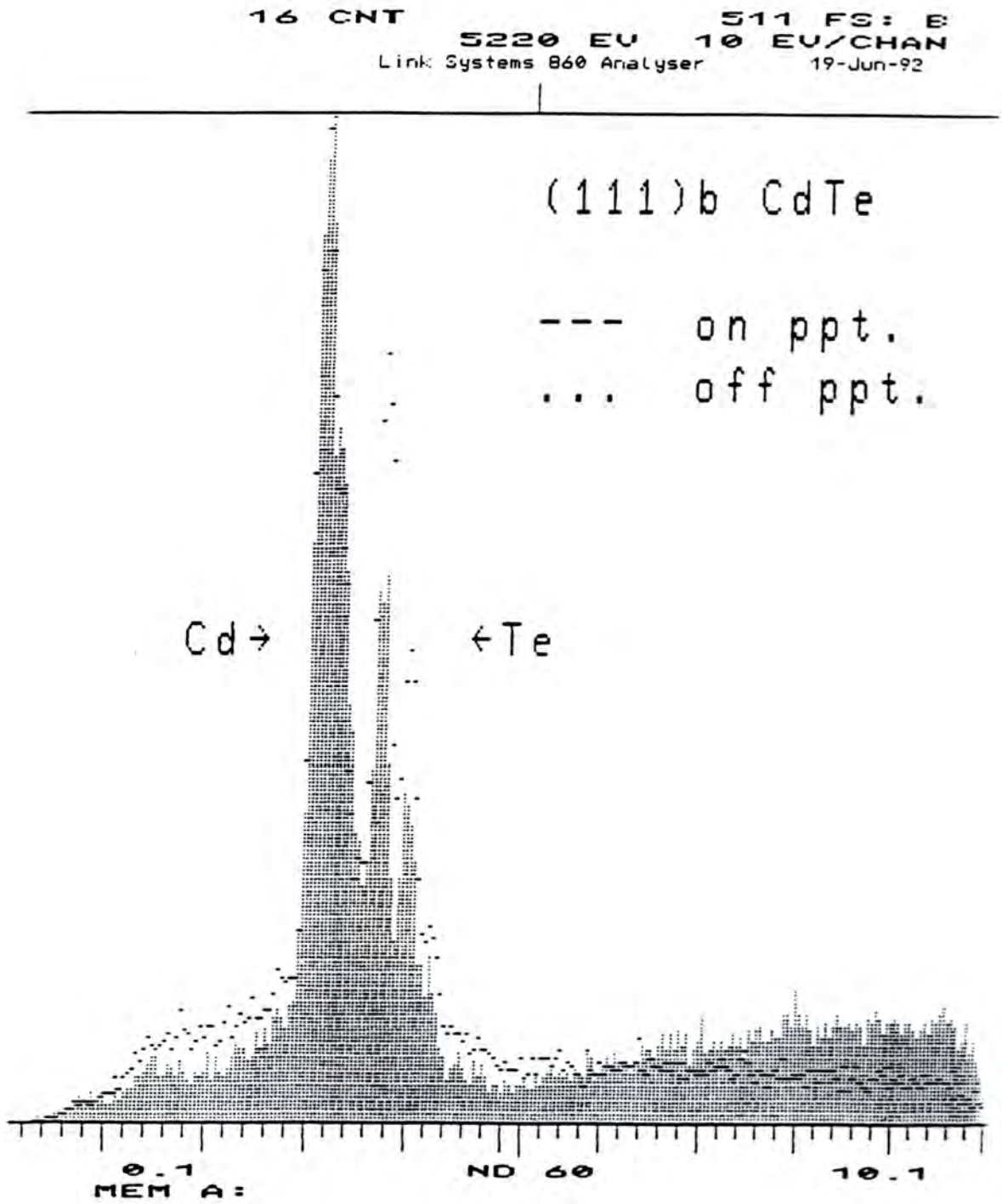

6.15 EDAX trace of precipitate shown in figure 6.14. The solid line shows the spectrum obtained from the precipitate whereas the dotted trace was recorded from the CdTe matrix.

6.2.3 Discussion

The average etch pit density of 3 - 5 x 10^4 cm^{-2}, on $(\bar{1}\bar{1}\bar{1})$B surfaces of ACRT CdTe crystals, revealed by ferric chloride etching compares well with the dislocation density of 3.3 x 10^4 cm^{-2}, revealed by Nakagawa's etch, on (111)A surfaces of samples cut from identical boules [1]. The value also compares favourably with dislocation densities reported in the literature for CdTe boules grown in different laboratories, Johnson [5] reports a dislocation density of 8 x 10^4 cm^{-2}, Sen et al [6] a value of 2 x 10^4 cm^{-2} and Lay et al [7] a dislocation density of 2 x 10^4 cm^{-2} for CdTe grown by the horizontal Bridgman technique. The dislocation density range of 3-5 x 10^4 cm^{-2} revealed by ferric chloride etching on the $(\bar{1}\bar{1}\bar{1})$B surface of $Cd_{0.96}Zn_{0.04}Te$ samples is also similar to published results for Nakagawa etching on (111)A, values of 4 x 10^4 cm^{-2} and 2 x 10^4 cm^{-2} being reported by Sen and Bruder respectively [6,8]. A value of 4.2 x 10^4 cm^{-2} has been reported by Capper et al [1] for (Cd,Zn)Te boules grown using the ACRT Bridgman technique. Sher [9] has previously reported that the incorporation of Zn into the CdTe lattice reduces the bond length, subsequently increasing both the hardness of the material and the dislocation energy, thus it may be expected that (Cd,Zn)Te boules contain a reduced dislocation density compared with CdTe, e.g as reported by Rai et al [10]. The observation of a similar dislocation density in boules of (Cd,Zn)Te and ACRT grown CdTe therefore indicates the high quality of the CdTe grown at G.E.C. Marconi, Southampton.

Although the $Cd_{0.96}Zn_{0.04}Te$ and ACRT CdTe substrates examined contain a similar dislocation density, the formation of cellular arrays of sub-grain boundaries is more advanced in boules of CdTe (see figures 6.2 and 6.7). Such an observation may be due to the 'solution hardening' which is observed in dilute alloys with the fcc structure [11], with the result that dislocations in boules of $Cd_{0.96}Zn_{0.04}Te$ are less mobile than those in pure CdTe and hence are unable to form a fully developed sub-grain array. Comparison of the triple axis X-ray rocking curves shown in figures 6.9a and 6.9b indicates a larger elongation in the ΔQ_y (tilt) axis in CdTe, confirming the greater spread in mosaic tilt present in this material. The average FWHM's, in the ΔQ_y direction, of 8" and 26" respectively for $Cd_{0.96}Zn_{0.04}Te$ and ACRT CdTe quantify this observation and these values compare favourably with (tilt) FWHM's of 16" and 26" previously reported for ACRT (Cd,Zn)Te and ACRT CdTe respectively [1]. The improved crystallinity in $Cd_{0.96}Zn_{0.04}Te$, compared to CdTe, observed in this work, has also been reported by other groups

[2,6]. The sub-grain misorientations of 6", 17" and 26", calculated from the average inter-dislocation distance in CL micrographs of $Cd_{0.96}Zn_{0.04}Te$, ACRT CdTe and non-ACRT CdTe respectively give only an approximate agreement with the tilts calculated from triple axis X-ray analysis. The difference is likely to be due to the boundaries containing dislocations with a range of different Burgers vectors, whereas the misorientations calculated from the CL micrographs assumed only the presence of 60^o type dislocations. Also it should be realised that this calculation is for the misorientation between adjacent grains while the X-ray measurement gives the distribution for an assembly of grains.

Measurements of the dilation in the substrates give a measure of the variation in stoichiometry (i.e change in composition and hence lattice parameter) within the materials. Thus from the low lattice dilation FWHM values of 11 and 9 arcseconds respectively, it may be concluded that both the ACRT CdTe and $Cd_{0.96}Zn_{0.04}Te$ boules examined in this work contain only small stoichiometric inhomogenities.

The enhanced quality of ACRT CdTe compared to non-ACRT material is shown by both the reduction in dislocation density (i.e $4.5x\ 10^4\ cm^{-2}$ in figure 6.1 and $1\ x\ 10^5\ cm^{-2}$ in figure 6.4) and mosaic tilt (i.e 26" and 40" respectively). The increased tilt is also indicated by the tighter sub-grain network, observed by CL, in non-ACRT CdTe crystals. In non-ACRT material an average cell size of 30μm is revealed whereas the average cell size in ACRT CdTe is in the range 60 -100μm. The lower dislocation density, and improved crystallinity, in CdTe boules grown by the ACRT modification is likely to be a result of the reduction in the thermal gradient in the growing crystal which is induced by the enhanced melt mixing. The slightly higher dilation measurement in non-ACRT CdTe (17 arcseconds) compared to ACRT CdTe (12 arcseconds) may also be accounted for by the greater melt mixing in the latter. The increased mixing in this instance helping to produce an increasingly homogeneous stoichiometry throughout the crystal.

The Te precipitate density range, of $0 - 30\ x\ 10^2\ cm^{-2}$ (figure 6.12) observed in ACRT CdTe is almost identical to the $1\text{-}30\ x\ 10^2\ cm^{-2}$ precipitate density previously reported for this material [1]. This value also compares favourably with other reported values for CdTe grown by the Bridgman technique without the incorporation of ACRT. Johnson [5] reports a maximum value of $1\ x\ 10^4\ cm^{-2}$ and Sen [6] gives a density of $2\text{-}5\ x\ 10^4\ cm^{-2}$. In boules of non-ACRT CdTe grown at G.E.C a Te precipitate density of $5\text{-}30\ x\ 10^4\ cm^{-2}$ has been reported [1], these boules containing Te precipitates > 10 μm in size. The I.R micrograph in figure

6.13 of an area of a $Cd_{0.96}Zn_{0.04}Te$ sample clearly shows a higher precipitate density than in figure 6.12 which shows an identical area in ACRT CdTe. The average value of ~ 1 x 10^4 cm^{-2} observed in the $Cd_{0.96}Zn_{0.04}Te$ boules examined in this work is typical of that reported in the literature, eg Sen [6] and Bruder [8] report values of 4 x 10^4 and 10^4 - 5 x 10^5 cm^{-2} respectively. It is however significantly higher than the value of 2-20 x 10^2 cm^{-2} reported in ACRT (Cd,Zn)Te [1].

The ACRT CdTe crystals examined in this work were typically grown under nearly stoichiometric conditions. However, such initial growth conditions have been reported to lead to growth from a Te rich melt [12], due to the higher evaporation rate of Cd from the melt [13], and hence the formation of Te inclusions is expected. In an attempt to obtain a stoichiometric melt the $Cd_{0.96}Zn_{0.04}Te$ samples examined have been grown under a Cd overpressure (by use of a Cd reservoir), such a technique being reported to lower the Te inclusion content of CdTe [12]. However the results presented here have indicate that the density (and often the size) of Te precipitates in ACRT crystals is significantly lower than that in non-ACRT boules including those grown under Cd rich conditions. Therefore it may be concluded that the maximised stirring of the melt provided by ACRT growth inhibits the formation of Te droplets at the melt boundary and hence on solidification the concentration of Te inclusions is decreased. The excess Te must therefore be present in solid solution, being accommodated in the existence region for CdTe on the T-x phase diagram.

All the Te precipitates observed in melt grown crystals in this work were ≤ 10 μm in diameter. Small inclusions such as these are not expected to be detrimental to LPE growth [5] however such inclusions will act as infra-red scattering centres and are undesirable when high optical transmission is required, i.e in (Cd,Hg)Te configurations with through-substrate illumination.

Precipitates observed by I.R microscopy as having a star shaped appearance, and located at the centre of rosettes formed by etch pits and dark CL spots have been identified by EDAX (figure 6.15) as Cd inclusions. The CL micrograph in figure 6.14b shows rosette arms longer than those revealed by I.R microscopy in figure 6.14a, i.e ~120 μm compared to 80μm. This indicates that the etch pits and CL spots in the arms represent dislocations rather than precipitates. However from the observation in the CL micrograph in figure 6.14b of very dark contrast at segments of the arms closest to the centre and from the star shaped appearance of the defect

under I.R microscopy it may be concluded that the dislocations in the arms closest to the precipitate are decorated. The nucleation of such dislocations may be explained using a 'punch out' mechanism for stress relief at a stress concentrator [14]. This explanation has been ascribed to similar features previously reported in Bridgman grown CdTe boules [15,16] however these defects were assumed to be large Te inclusions. Such a stress may be accounted for by considering the contraction of inclusions of elemental Cd or Te situated within the CdTe matrix. Both Cd and Te have a higher thermal expansion coefficient (31.8×10^{-6} and 16×10^{-6} K^{-1} respectively) than CdTe (4.5×10^{6} K^{-1}) and hence on cooling from their respective melting points (594K and 725K), impose a tensile stress on the lattice. This stress may be relieved by the nucleation of dislocations on {111} slip planes which intersect the $(\bar{1}\bar{1}\bar{1})$B CdTe surface at 60° intervals, giving the characteristic rosettes shown in figure 6.14. From Hull [14], the misfit parameter (ε) of an inclusion in a hole in a semiconductor crystal is defined by:-

$$\varepsilon = \Delta T (\alpha_1 - \alpha_2)$$

where α_1 is the thermal coefficient of expansion of Cd or Te, α_2 that of CdTe and ΔT is the temperature change. Hull also defines τ_n as the stress required for the spontaneous nucleation of dislocations where τ_n is defined by,

$$\tau_n = G / 4\pi e = 3\varepsilon G$$

where G is the bulk modulus of the crystal and e is the base of the natural logarithm (i.e. 2.718). Hence for the spontaneous nucleation of dislocations $\varepsilon \geq 9.8 \times 10^{-3}$. On substituting the thermal coefficients of expansion for Cd and Te, misfit parameters of 8×10^{-3} and 4.8×10^{-3} are obtained respectively. This calculation suggests that neither inclusion generates sufficient stress to nucleate dislocations. However the misfit for Cd inclusions is approximately double that for Te, and is very close to the critical value. Balasubramanian and Wilcox [17] have reported that dislocation motion and multiplication in semiconductors occurs at stresses of 0.3 - 0.6 times the critical resolved shear stress (CRSS) and hence it is likely that the formation of Cd inclusions will induce the nucleation of dislocation rosettes. Due to the lower thermal expansion coefficient this is less probable for Te inclusions. Confirmation of the association of dislocation rosettes with Cd precipitates was given by EDAX, i.e. figure 6.15. No such features were observed near Te precipitates.

The dislocation rosettes observed at Cd inclusions were similar to those revealed by CL and defect etching in micro-indentation experiments on CdTe and GaAs [18,19,20]. In these experiments, {111} oriented samples were stressed using a Vickers indentor, inducing dislocation rosettes consisting of six double (i.e long and short) arms which pointed in <110> directions. On application of an external stress to an indented $(\bar{1}\bar{1}\bar{1})$B CdTe surface it was concluded [19] that the long and short arms consisted of 60° Te (glide) and 60° Cd (glide) dislocations respectively. On etching the CdTe surface the rosette arms induced by indentation were observed to vanish after the removal of ~ 50 μm of material, indicating that the arms consist of shallow dislocation loops. In the centre of indented regions in both CdTe and GaAs the formation of two equilateral triangles of etch pits [19,20] and lines of dark CL contrast [18] were observed, the sides of the triangles lying parallel to <110> directions but rotated by 180° with respect to each other. Such features were accounted for [19] by the generation of dislocations on {111} slip planes defining two tetrahedra within the sphalerite lattice, one with an external apex and the other an internal apex .This accounts for the etch pit distribution shown in figure 6.10. In this optical micrograph no rosette is visible, hence it may be concluded that the sample area was situated directly above or below the site of a Cd precipitate. At increasing depths from indented surfaces the triangle defined by the tetrahedron with the external apex was reported to grow [18,19,20] whereas that defined by the tetrahedron with the internal apex was reported to reduce in size, eventually revealing the apex of the tetrahedron. In figure 6.11 such an apex is visible, formed by the three lines of dark CL contrast. The apex is situated inside lines of contrast forming an equilateral triangle representing dislocations on {111} slip planes defining an externally apexed tetrahedron. Therefore as in figure 6.10 the sample area shown in figure 6.11 is either directly above or below a Cd precipitate.

Whereas Te inclusions in Bridgman grown material appear coherent with the CdTe matrix, Cd inclusions are seen to introduce structural defects which range over a relatively large substrate volume. Hence the occurrence of Cd precipitates is seen to be strongly detrimental to the CdTe crystal quality.

6.3 Vapour grown CdTe

In this section the distribution and nature of extended defects in CdTe grown from the vapour using the 'Durham' technique is examined. In order to compare the quality of such material with CdTe grown by the Bridgman technique, only the occurrence of dislocations (sub-grain boundaries) and precipitates is discussed. It

[21] and an example of a typical twin lamella in 'Durham' CdTe is shown in figure 4.3 in section 4.3.1.

6.3.1 Structural Defects in CdTe grown by the 'Durham' Technique

Samples cut from polycrystalline boules of 'Durham' grown material were characterised in CL micrographs by a well defined cellular sub-grain structure, as shown in figure 6.16. The size of the sub-grain cells typically varied in the range 60 - 100 μm and individual dislocations at the boundaries were unresolvable in CL micrographs, indicating a dislocation separation $\leq 0.8\mu m$. At sample areas within sub-grain cells no dislocations were visible.

Te precipitates (identified by EDAX) in the 'Durham' material were typically 10-30μm in size, and were invariably observed to decorate twin or grain boundaries. Figure 6.17 shows a 16μm precipitate decorating a lateral twin boundary, i.e at A.

6.3.2 Discussion

A comparison between typical CL micrographs of vapour grown (e.g figure 6.16) and melt grown CdTe (figure 6.2) indicates a similar sub-grain size of ~60-100 μm in both materials. However in Bridgman CdTe samples the cells consist of loose groupings of dislocations, (producing a tilt of ≤ 26 arcseonds), whereas the dislocations forming the sub-grain boundaries in the vapour grown material have a separation smaller than the resolution of the CL system. T.E.M analysis of such sub-grains [4], revealed a dislocation separation of 0.05 - 0.5 μm, corresponding to a tilt of 3' - 25' (assuming the dislocations have Burgers vector a/2<110>). The tight cellular arrays in the 'Durham' material are consistent with an advanced degree of polygonisation and indicate an equilibrium distribution of dislocations. The equilibriated nature of the vapour material has been ascribed to the long crystal growth period of 10 - 14 days (i.e. growth rate of ~2mm / day), allowing the dislocations time to reach an equilibrium distribution. In material grown from the vapour using a modified Piper - Polich technique and employing a shorter growth period a less advanced polygonisation structure was observed [3]. The observation of a less well developed sub-grain structure in the melt grown material may therefore be also accounted for by the faster growth rate used in the Bridgman technique; i.e.~1mm / hour. The shallow temperature gradient utilised in the

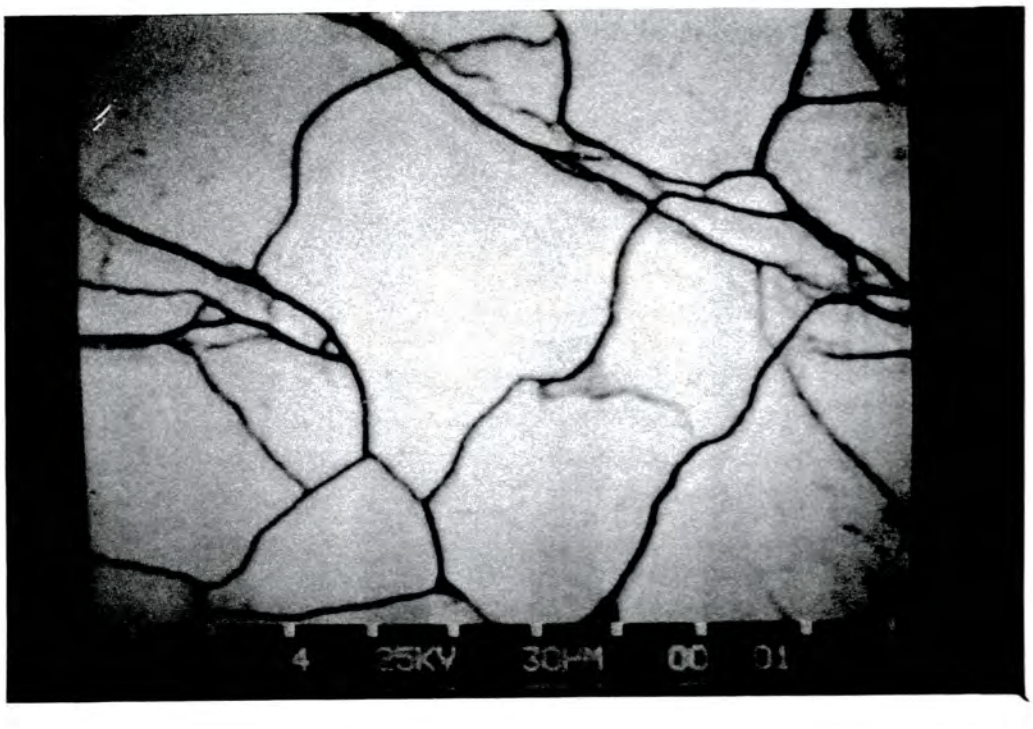

Figure 6.16 Sub-grain boundaries in CdTe grown by the 'Durham' (vapour growth) technique.

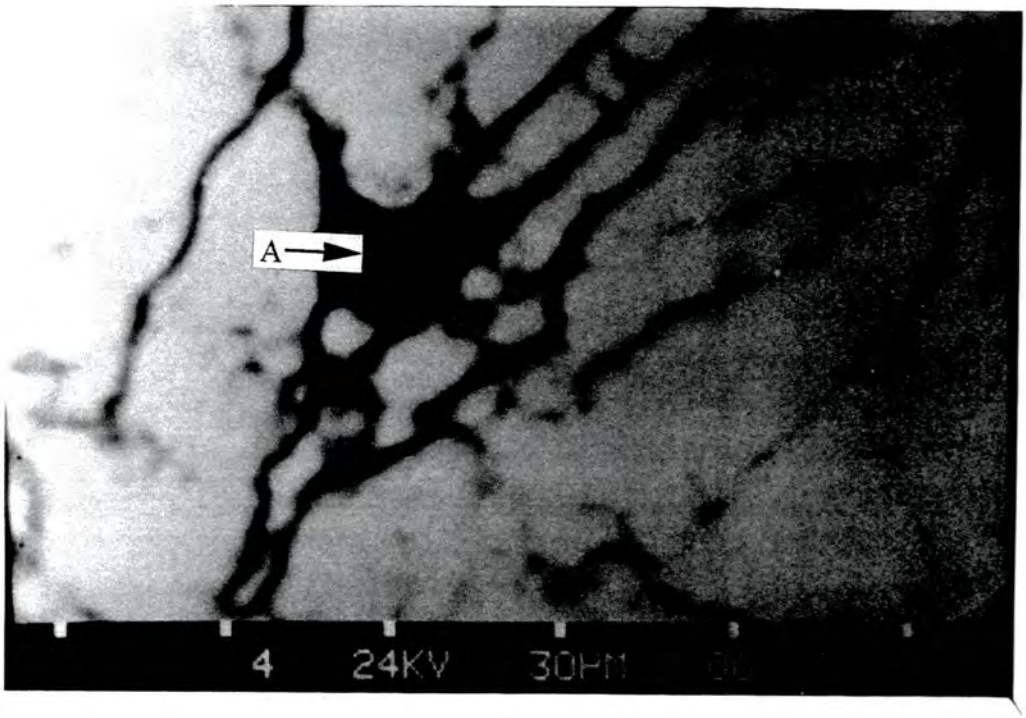

Figure 6.17 CL micrograph showing the decoration of a lateral twin boundary by a Te precipitate

Bridgman process however is also reported to reduce the occurrence of sub-grain boundaries [22]. Finally it must be noted that the Bridgman samples were obtained from high quality areas of the melt grown boules, whereas no attempt was made to find good parts of the vapour grown boule.

The size and distribution of Te precipitates in the 'Durham' material is also consistent with an equilibrium situation, with large inclusions 20 - 30 μm forming which segregate preferentially to grain and twin boundaries during the extended growth period [3].

Despite the poor crystal quality of the 'Durham' grown CdTe compared with the best Bridgman material, vapour growth does offer advantages over growth from the melt [23]. Vapour growth may be performed at temperatures below the congruent melting point (1092°C), giving the benefit of reduced thermal strain on cooling, a higher critical resolved shear stress at the growth temperature [17], and less contamination. Furthermore by controlling the composition of the vapour by use of separate sources stoichiometric growth may be obtained. These advantages have yet to be realised in practice.

6.4 Conclusions

Boules of CdTe grown by the ACRT variation of the Bridgman technique at G.E.C Marconi, in Southampton, contain a dislocation density in the range 3-5 x 10^4 cm^{-2} (measured from etch pits developed by ferric chloride etching) which is comparable to the best results reported for CdTe in the literature. The dislocation density of the ACRT CdTe substrates was significantly lower than the dislocation density of 9 x 10^4 - 2 x 10^5 cm^{-2} typically observed in boules of non-ACRT CdTe also grown at G.E.C Marconi. Furthermore the ACRT CdTe dislocation density was almost identical to that measured in substrates cut from boules of (non-ACRT) $Cd_{0.96}Zn_{0.04}Te$ grown under a Cd overpressure. It is encouraging that CdTe boules may be grown with a dislocation density comparable to that observed in $Cd_{0.96}Zn_{0.04}Te$, as generally the lowest dislocation densities are observed in the latter.

Comparisons between the sub-grain cell sizes in ACRT and non-ACRT CdTe also shows the improved crystal quality obtained using the ACRT modification. The former contains cells with an average size of 60-100μm whereas the latter contains

sub-grain cells typically 30μm in size. The difference in crystallinity is quantified by the tilt FWHM values obtained using triple axis X-ray analysis; i.e a mosaic spread of 26 arcseconds in ACRT CdTe compared to 40 arcseconds reported in the non-ACRT CdTe [1]. However, comparison of ACRT CdTe with (non-ACRT) $Cd_{0.96}Zn_{0.04}Te$ highlighted the advantage of the alloy system over the binary. The $Cd_{0.96}Zn_{0.04}Te$ boules had larger sub-grains (100-150μm) and contained a lower mosaic tilt (8 arcseconds). The formation of a less well developed cellular sub-grain structure, containing larger sub-grain cells in (Cd,Zn)Te compared to the well defined structure in CdTe, indicates that the incorporation of ~ 4% Zn into the lattice reduces the mobility of dislocations.

The Te precipitate content of ACRT CdTe was significantly lower than both that in non-ACRT CdTe, and non-ACRT $Cd_{0.96}Zn_{0.04}T$ grown under a Cd overpressure. Precipitate densities of 0 - 30 x 10^2 cm^{-2} and 1 x 10^4 cm^{-2} were observed in ACRT CdTe and non-ACRT $Cd_{0.96}Zn_{0.04}Te$ respectively, and a density of 5-30 x 10^2 has been previously reported for non-ACRT CdTe grown by G.E.C Marconi [1].

Therefore to summarise, boules of CdTe grown with the ACRT modification have been observed to contain a reduced dislocation and precipitate density, and an improved crystallinity, compared to boules of non-ACRT CdTe grown in the same laboratory. Furthermore the ACRT CdTe contains a comparable dislocation density and a reduced precipitate density compared to boules of non-ACRT $Cd_{0.96}Zn_{0.04}Te$. The improvement in the CdTe crystal quality is likely to be a result of the enhanced melt mixing which is obtainable during ACRT growth. However, the substrates with the best crystallinity remain those cut from boules of (Cd,Zn)Te.

Whereas the Te precipitates observed in this work did not introduce additional defects into the lattice, the occurrence of Cd inclusions was observed to coincide with the introduction of a localised high density of dislocations into the lattice. The dislocations nucleated were similar to punch out dislocation rosettes observed when CdTe is stressed by a micro-indentor, and are the result of the lattice undergoing a tensile stress on cooling due to the highly dissimilar thermal coefficient of expansions of Cd inclusions and the CdTe matrix. The thermal stress around Te inclusions is not great enough to induce dislocation formation since the thermal expansion coefficient is too low.

Examination of a boule of vapour grown CdTe revealed an equilibrium distribution of defects and a significantly poorer crystal quality compared to melt grown

material. The vapour material grown by the 'Durham' technique is characterised by the formation of dense arrays of dislocations in sub-grain boundaries, which induce a large substrate tilt (3-30' compared to 26" in Bridgman ACRT CdTe), and by the segregation of large, 20-30μm, Te precipitates to grain and twin boundaries. These features are thought to be a result of long growth times.

REFERENCES FOR CHAPTER SIX

1. P. Capper, J.E. Harris, E. O'Keefe, C.L. Jones, C.K. Ard, P. Mackett and D. Dutton, Mats. Sci. Eng. **B16** (1993) 29.
2. see for example: S.L. Bell and S.Sen, J. Vac. Sci. Technol. **A3** (1985) 112.
3. K. Durose and G.J. Russell, J. Crystal Growth **86** (1988) 471.
4. K. Durose, Ph.D Thesis, University of Durham, 1986.
5. C.J. Johnson, SPIE **1106** (1989) 56.
6. S. Sen, W. H. Konkel, S. J. Tighe, L. G. Bland, S.R. Sharma and R.E. Taylor, J. Crystal Growth **86** (1988) 111.
7. K. Y. Lay, D. Nichols, S. McDevitt, B.E. Bean and C.J. Johnson, J. Crystal Growth **86** (1988) 118.
8. M. Bruder, H. Figgemeir, R. Schmitt and H. Maier, Mats. Sci. Eng. **B16** (1993) 40.
9. A.R. Sher, A-B. Chen and W.E. Spicer, Appl. Phys. Lett. **46** (1985) 54.
10. R.S. Rai, S. Mahajan, S. McDevitt and C.J. Johnson, J. Vac. Sci. Technol. **B9** (1991) 1892.
11. T. Suzuki, S. Takeuchi and H. Yoshinaga, in : 'Dislocations, Dynamics and Plasicity', (Springer-Verlag, Berlin Heidelberg, 1992).
12. P. Rudolph and M. Mühlberg, Mats. Sci. Eng **B16** (1993) 14.
13. K. Peters, A. Wenzel, and P. Rudolth, Cryst. Res. Technol. **25** (1990) 10.
14. D. Hull,' Introduction to Dislocations', (Permagon Press (2nd Ed.), 1975).
15. A. W. Vere, V. Steward, C. A. Jones, D.J. Williams and N. Shaw, J. Crystal Growth **72** (1985) 97.
16. M. Wada and J. Suzuki, Jap. J. Appl. Phys. **27** (1988) L972.
17. R. Balasubramanian and W.R. Wilcox, Mats. Sci. Eng **B16** (1993) 1.
18. A. Rivière, B. Sieber and J.P Rivière, Microsc. Microanal. Microstruct. **2** (1991) 503.
19. C. Braun and H.W. Helberg, Philos. Mag A **53** (1986) 277.
20. P.B. Hirsch, P. Pirouz, S.G. Roberts and P.D. Warren, Philos. Mag B **52** (1985) 759.
21. K. Durose, G.J Russell and J. Woods, J. Crystal Growth **72** (1985) 85.
22. M. Mühlberg, P. Rudolph, C. Genzel, B. Wemke and V. Becker, J. Crystal Growth **110** (1990) 275
23. K. Durose, A. Turnbull and P.B. Brown, Mats. Sci. Eng. **B16** (1993) 96.

CHAPTER SEVEN

Structural Defects in Epitaxial (Cd,Hg)Te

7.1 Introduction

In the previous experimental chapters bulk CdTe and (Cd,Zn)Te substrates have been examined. In this chapter however the structural quality of layers of epitaxial (Cd,Hg)Te grown on both CdTe and (Cd,Zn)Te substrates is assessed. The LPE layers examined were all grown on $(\bar{1}\bar{1}\bar{1})$B oriented substrates and hence the layer orientation investigated is also $(\bar{1}\bar{1}\bar{1})$B. They were assessed using defect selective etching, triple axis X-ray and EBIC techniques and particular attention was given to the variation in dislocation density as a function of the film thickness.

7.2 Defect Selective Etching Studies of (Cd,Hg)Te

To investigate the dislocation density in (Cd,Hg)Te layers as a function of distance from the interface, bevelled samples were prepared using the technique described in section 2.3. Defect etching was then performed using a saturated aqueous ferric chloride solution (see section 6.2) and the Hähnert etch. The Hähnert etch has previously been reported to reliably develop pits on the $(\bar{1}\bar{1}\bar{1})$B face of (Cd,Hg)Te [1]. The compositions of the (Cd,Hg)Te layers were measured by optical transmission.

Figure 7.1 shows the variation in (Hähnert) etch pit density of a $Cd_{0.24}Hg_{0.76}Te$ layer grown on an ACRT CdTe substrate. The lattice mismatch of this system is 0.3%. The figure shows that the etch pit density decreases with increasing film thickness, from the near interface value of 3×10^7 cm^{-2}, to a background density of $\sim 3 \times 10^5$ cm^{-2}. The background density is reached at a film thickness of ~ 6μm and shows little variation throughout the remainder of the layer. The fall in etch pit density is revealed clearly in figures 7.2a-d (obtained along a bevelled layer), which show optical micrographs of the etch pit distribution for layer thicknesses of 3.2μm, 5.4μm, 9μm, and 14μm, the etch pit densities in figures 7.2a-d being ~ 1×10^6 cm^{-2}, 5×10^5 cm^{-2}, ~ 3×10^5cm^{-2} and 3×10^5 cm^{-2} respectively. Ferric chloride etching of the CdTe substrate (figure 7.2e) indicated a dislocation density of 3×10^4 cm^{-2}.

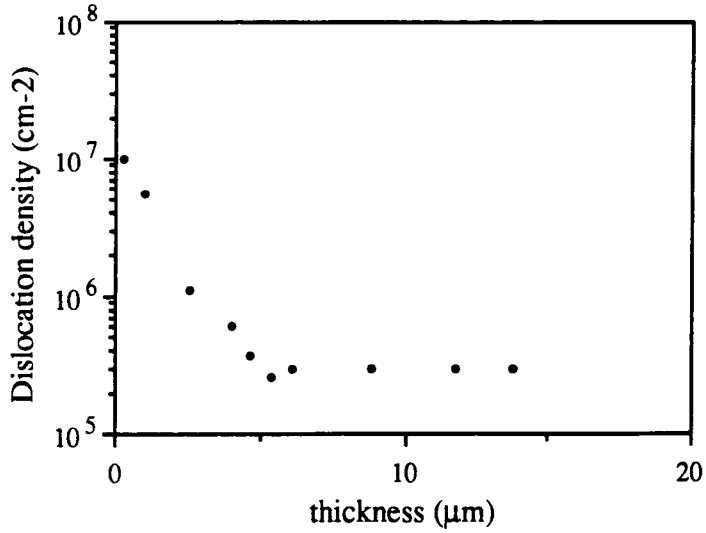

Figure 7.1 Variation in etch pit density with epilayer thickness in $Cd_{0.24}Hg_{0.76}Te$ / CdTe

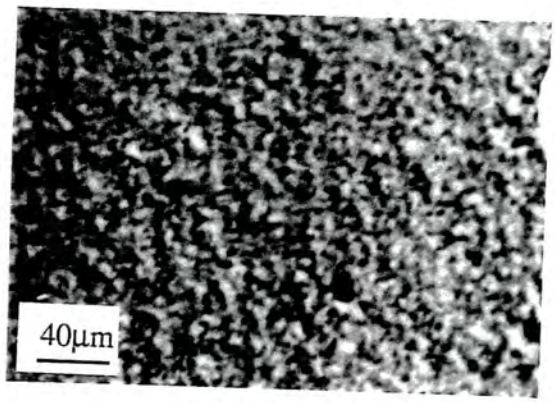

(a)

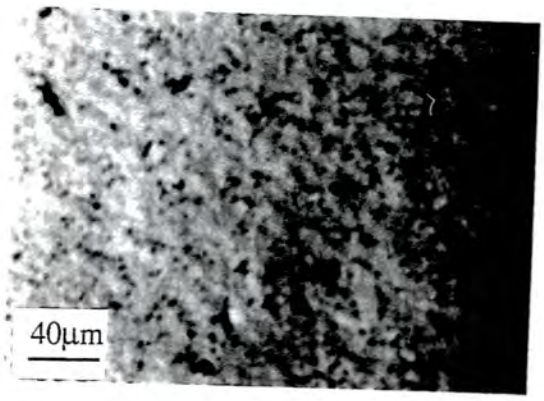

(b)

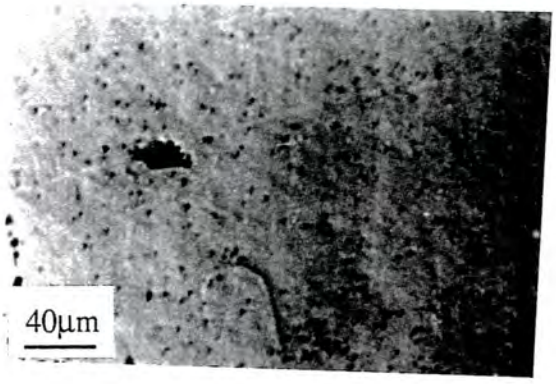

(c)

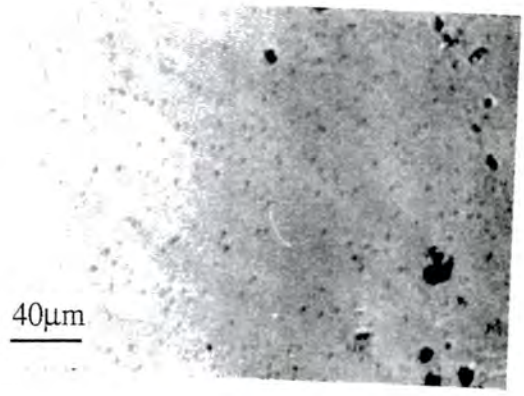

(d)

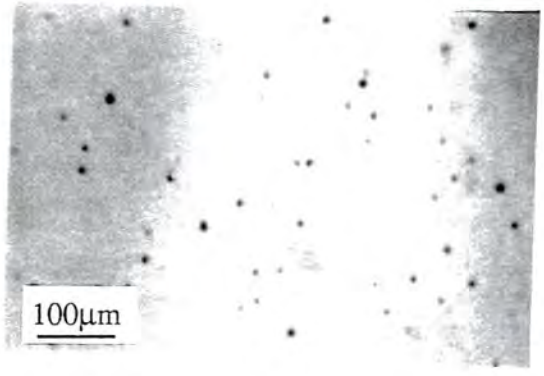

(e)

Figure 7.2 Etch pit distribution in $Cd_{0.24}Hg_{0.76}Te$ / CdTe, at layer thicknesses of (a) 3.2μm, (b) 5.4μm, (c) 9μm, (d) 14μm (Hähnert etch) and in (e) CdTe substrate (ferric chloride etch) .

Figure 7.3 shows the etch pit distribution for a $Cd_{0.24}Hg_{0.76}Te$ layer grown on a $Cd_{0.96}Zn_{0.04}Te$ substrate. The lattice mismatch in this system is 0.01%. The initial (i.e chemical interface) etch pit density is ~ 3 x 10^5 cm^{-2} and after rising to a maximum value of 1 x 10^6 cm^{-2}, the etch pit density falls with increasing layer thickness until a background density is obtained for layer thicknesses ≥6μm. The background dislocation density of ~ 9 x 10^4 cm^{-2} was revealed by both the ferric chloride and Hähnert etching solutions, as shown in figures 7.4a and 7.4b. Ferric chloride etching of the $Cd_{0.96}Zn_{0.04}Te$ substrate revealed a dislocation density of 3 x 10^4 cm^{-2}, as shown in figure 7.4c.

Whereas in figure 7.1 the maximum etch pit density is at the chemical interface, in figure 7.3 the peak density occurs ~ 0.6μm within the layer. The displacement of the maximum etch pit density away from the chemical interface in $Cd_{0.24}Hg_{0.76}Te$ / $Cd_{0.96}Zn_{0.04}Te$ is clearly shown in figure 7.5.

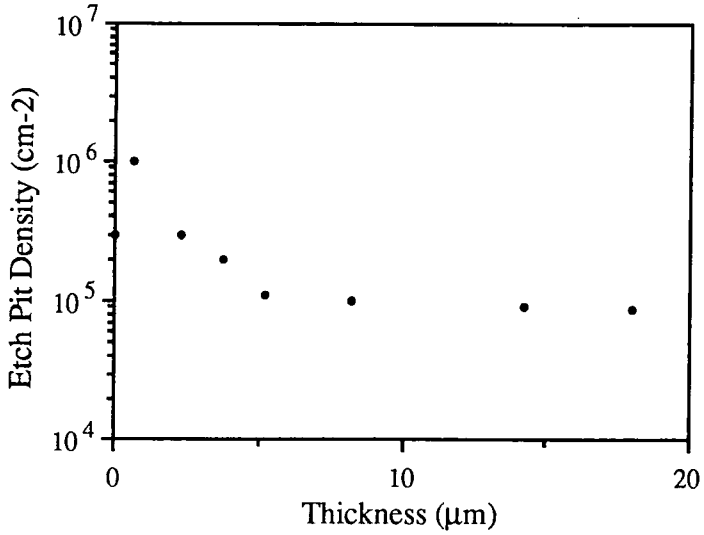

Figure 7.3 Variation in Etch Pit Density with epilayer thickness in $Cd_{0.24}Hg_{0.76}Te$ / $Cd_{0.96}Zn_{0.04}Te$

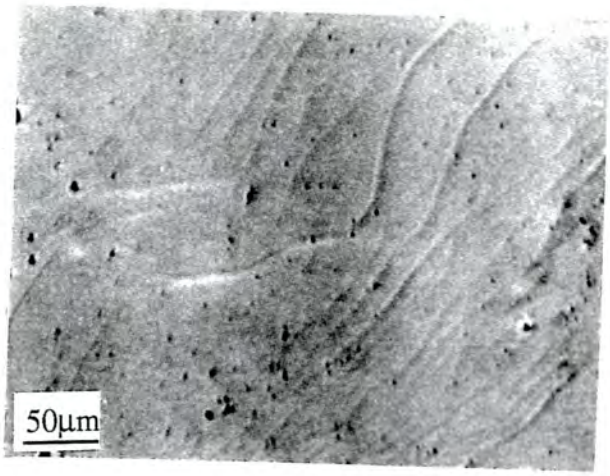

(a)

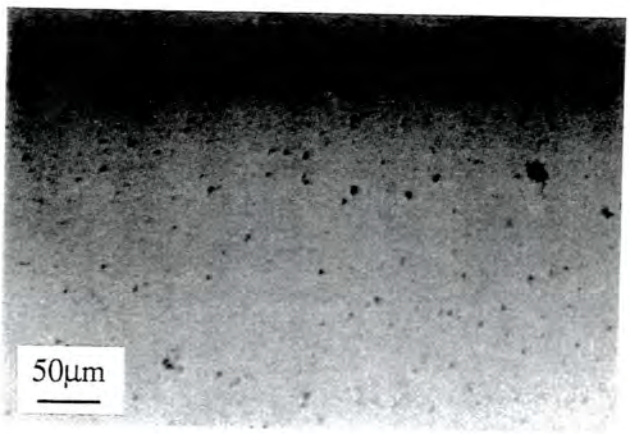

(b)

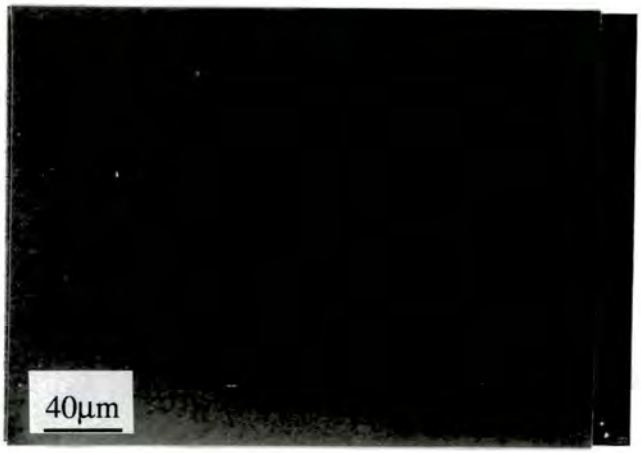

(c)

Figure 7.4 Etch pit distribution in $Cd_{0.24}Hg_{0.76}Te$ / $Cd_{0.96}Zn_{0.04}Te$; (a) etch pit distribution developed by Hähnert etch for a 18µm thick layer , (b) etch pit distribution developed by ferric chloride etching for an identical layer and thickness, (c) typical etch pit distribution developed in $Cd_{0.96}Zn_{0.04}Te$ substrate by ferric chloride etching.

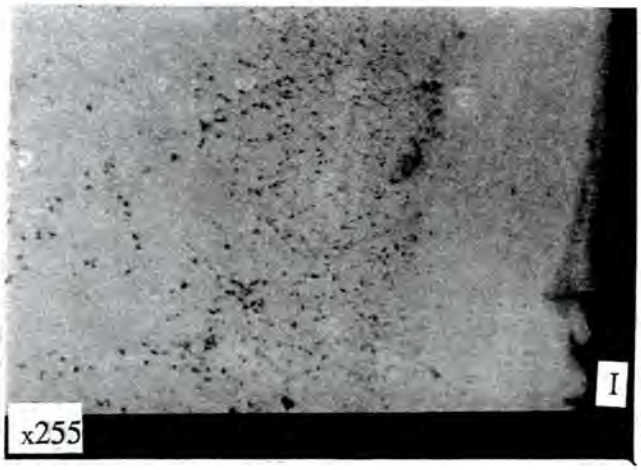

Figure 7.5 Movement of maximum dislocation density away from chemical interface (labelled I) in $Cd_{0.24}Hg_{0.76}Te$ / $Cd_{0.96}Zn_{0.04}Te$.

7.3 Triple Axis X-ray Diffraction Studies

The $Cd_{0.24}Hg_{0.76}Te$ / CdTe layer etched in the previous section was also assessed using the triple axis X-ray diffraction technique (see section 3.3). By etching back (using a 0.5 % bromine in methanol solution) from the as-grown state, layer thicknesses of 10μm and 2μm were examined. The reciprocal space maps for the 10μm and 2μm thick layers are shown in figure 7.6a and 7.6b, and both reveal an elongation in the ΔQ_y (tilt) direction. The FWHM's of the layer tilt, lattice dilation and total (standard double crystal) rocking curve at both thicknesses are summarised in Table 7.1. The tilt rocking curve FWHM shows an increase with decreasing film thickness, however the dilation FWHM shows only a small variation.

A $Cd_{0.24}Hg_{0.76}Te$ / $Cd_{0.96}Zn_{0.04}Te$ epilayer (not that examined in the previous section) has been examined at layer thicknesses of 12μm and 5μm. The triple axis reciprocal space map obtained at 12μm and 5μm are shown in figures 7.7a and 7.7b respectively. For a 12μm thick layer the map is elongated in the ΔQ_y (tilt) axis, however at a thickness of 5μm a tail is also visible in the ΔQ_z (dilation) axis. The FWHM's obtained from the $Cd_{0.24}Hg_{0.76}Te$ / $Cd_{0.96}Zn_{0.04}Te$ layer are also summarised in Table 7.1. The increase in the tilt and dilation rocking curve widths with decreasing thickness show a similar trend to the results obtained for

System	Layer thickness (μm)	Dislocation Density (cm^{-2})	FWHM Total (arcsec)	FWHM Tilt (arcsec)	FWHM Dilation (arcsec)
$Cd_{0.24}Hg_{0.76}Te$ /	10	3×10^5	51	39	12
CdTe	2		51	46	13
(0.3% misfit)			(31)	(25)	(11)
$Cd_{0.24}Hg_{0.76}Te$ /	12	1×10^5	35	29	12
$Cd_{0.96}Zn_{0.04}Te$	5		46	36	14
(0.01% misfit)			(17)	(8)	(9)

Table 7.1 X-ray rocking curve widths and ferric chloride etch pit densities in $Cd_{0.24}Hg_{0.76}Te$. (The values in brackets are the corresponding rocking curve FWHM's for the respective substrates)

$Cd_{0.24}Hg_{0.76}Te$ / CdTe. The dislocation density of 1×10^5 cm^{-2} at a layer thickness of 12μm (figure 7.8) was calculated after ferric chloride etching.

7.4 EBIC Studies

EBIC studies of (Cd,Hg)Te layers were performed using the technique described in section 2.2.2. EBIC micrographs revealed a cellular structure in both epitaxial $Cd_{0.24}Hg_{0.76}Te$ / CdTe and $Cd_{0.24}Hg_{0.76}Te$ / $Cd_{0.96}Zn_{0.04}Te$. Figure 7.9 shows a cellular network with an average cell size of 30μm in in a 5μm thick layer grown on CdTe whereas figure 7.10 shows an average cell size of 75μm in a 5μm layer grown upon $Cd_{0.96}Zn_{0.04}Te$.

The extended lines of contrast (e.g at A) in figure 7.10 are microtwins lying on inclined {111} planes within the layer. These twins lie at 60° to <110> cleaved edges and have a maximum length of ~100μm and width of 10μm.

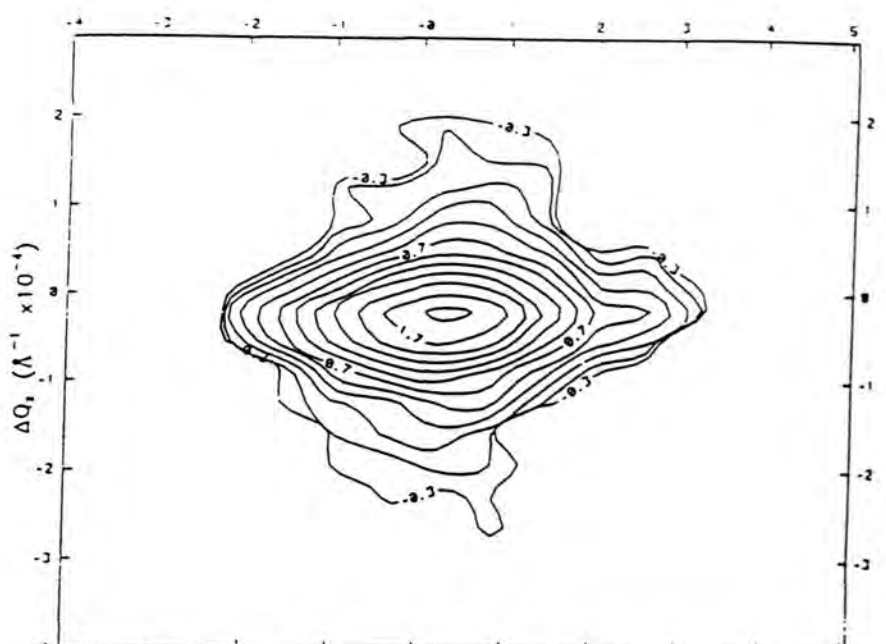

(a)

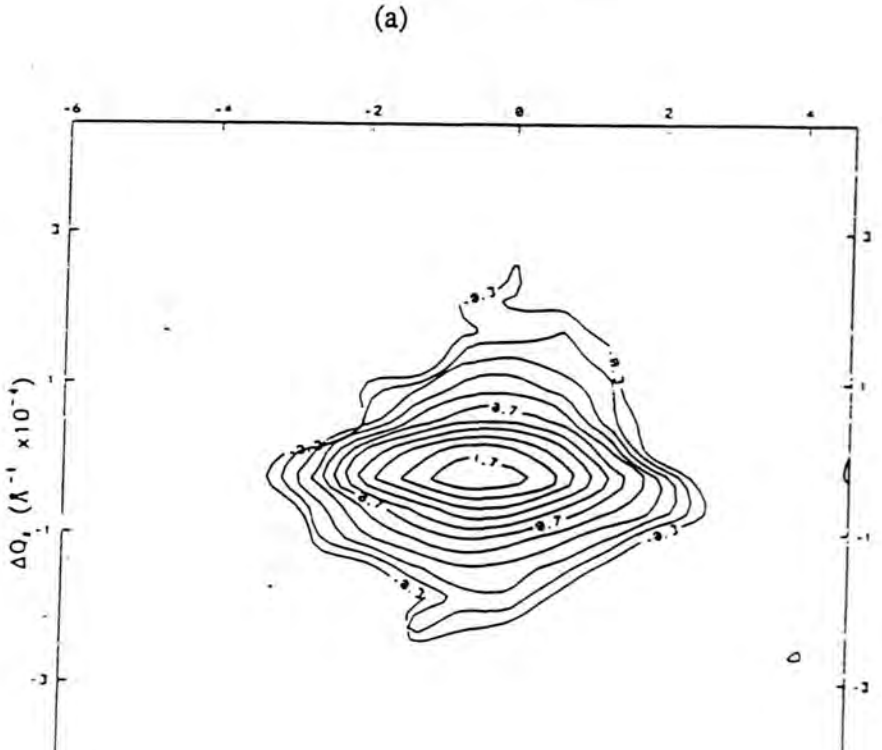

(b)

Figure 7.6 Triple axis X-ray diffraction reciprocal space maps for $Cd_{0.24}Hg_{0.76}Te$ / CdTe at layer thicknesses of (a) 10μm and (b) 2μm .

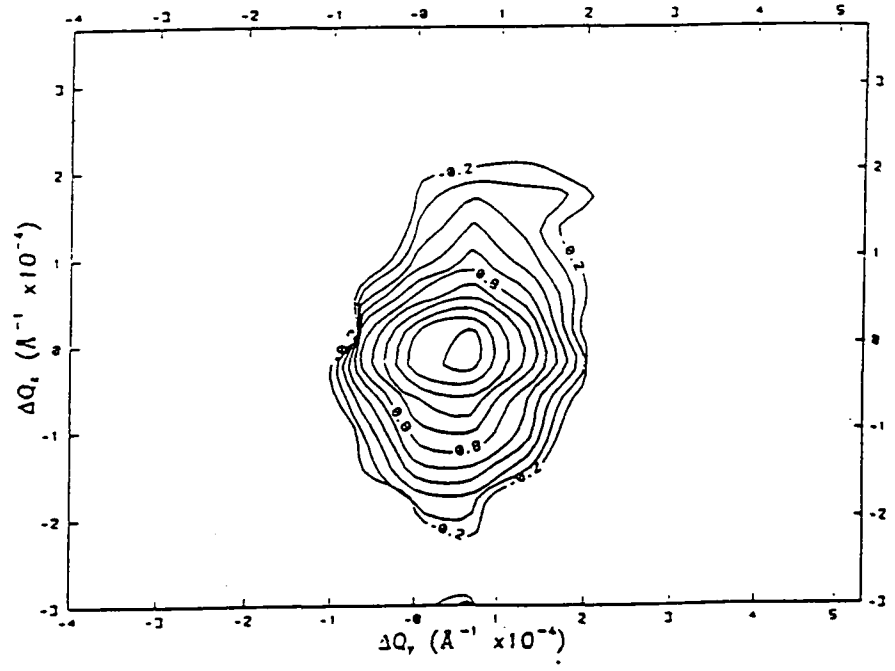

(a)

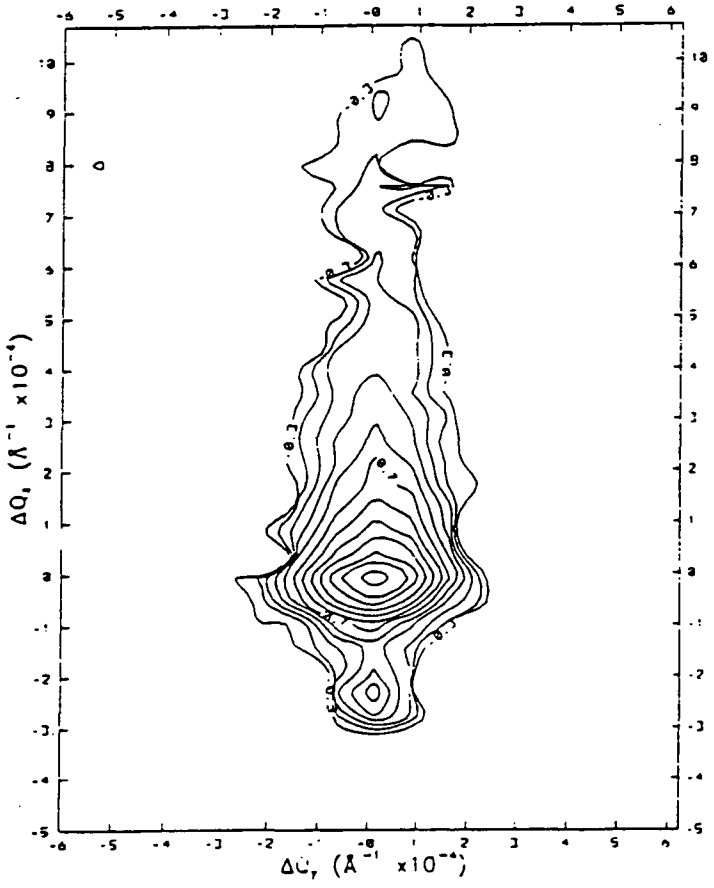

(b)

Figure 7.7 Triple axis X-ray diffraction reciprocal space maps for $Cd_{0.24}Hg_{0.76}Te$ / $Cd_{0.96}Zn_{0.04}Te$ at layer thicknesses of (a) 12μm and (b) 5μm.

7.5 Discussion

Defect etching of bevelled $Cd_{0.24}Hg_{0.76}Te$ epilayers has revealed a decrease in the threading dislocation density with increasing film thickness. It can be seen however from figures 7.1 and 7.3 that the threading dislocation density does not continue to fall indefinitely with increasing thickness but reaches a constant lower level or 'background' level at a thickness of ≥5-6μm. For layers grown on CdTe and $Cd_{0.96}Zn_{0.04}Te$ the background dislocation densities were calculated as 3×10^5 and 9×10^4 cm^{-2} respectively. The average 'background' dislocation density of 9×10^4 cm^{-2} in $Cd_{0.24}Hg_{0.76}Te$ / $Cd_{0.96}Zn_{0.04}Te$ was also confirmed by ferric chloride etching, as shown in figure 7.4b. These 'background' values are significantly higher than the ~ 3×10^4 cm^{-2} dislocation density measured in both the corresponding CdTe and $Cd_{0.96}Zn_{0.04}Te$ substrates and hence it may be concluded that the background dislocation density in the epilayers examined in this work, irrespective of the substrate, is higher than the substrate dislocation density. A similar conclusion is implicit from the spread of mosaic tilts calculated using the triple axis X-ray diffraction technique. The mosaic tilt FWHM's in Table 7.1 for film thicknesses corresponding to the background dislocation density (i.e > 5-6μm) are significantly higher those that measured in the corresponding substrate, therefore also indicating that the substrate dislocation density is not preserved in the corresponding epitaxial layer.

The defect etching and triple axis X-ray results also reveal in layers of comparable thickness a higher dislocation density in epilayers grown on CdTe compared with those grown on $Cd_{0.96}Zn_{0.04}Te$. This increased dislocation density is obvious on comparison of the background etch pit densities in figures 7.1 and 7.3 (i.e 3×10^5 cm^{-2} compared to 9×10^4 cm^{-2}), and is also revealed in Table 7.1 by the increased mosaic tilt FWHM in the layer grown on CdTe, i.e a tilt FWHM of 39 arcseconds for 10μm $Cd_{0.24}Hg_{0.76}Te$ / CdTe compared with a tilt FWHM of 29 arcseconds for 12μm $Cd_{0.24}Hg_{0.76}Te$ / $Cd_{0.96}Zn_{0.04}Te$. These values may be interpreted as dislocation densities using the well known Gay formula [2],

$$D(h) = \frac{B^2-\beta^2}{9b^2}$$

where D(h) is the threading dislocation density (cm^{-2}), B is the (tilt) rocking curve FWHM in radians, β is the rocking curve width with no broadening due to defects

(assumed to be ~ 10") and b is the dislocation Burgers vector. The dislocations are assumed to be 60° type, i.e b = a/2<110>. Application to quantitative X-ray results obtained in this work gives dislocation densities approximately an order of magnitude higher than those calculated after defect etching. For example the background dislocation density of 3×10^5 cm^{-2} for the $Cd_{0.24}Hg_{0.76}Te$ / CdTe layer in figure 7.1 compares unfavourably to the X-ray dislocation density of 1.8×10^6 cm^{-2} obtained using the corresponding tilt rocking curve value of 39 arcseconds (i.e for a 10μm thick layer) in Table 7.1. This discrepancy might cast some doubt on either (or both) the applicability of Gay's mosaic model to the epitaxial systems examined in this work, or the assumption of there being 60° dislocations only. Nevertheless the decrease in the tilt FWHM's with increasing layer thickness for the epilayers in Table 7.1, is consistent with a reduction in mosaic spread and hence confirms the decrease in dislocation density with increasing layer thickness shown by defect etching.

In section 2.3.2.1 the mechanisms for lattice relaxation in epitaxial films were discussed, with the Matthews-Blakeslee model [3] and the half-loop mechanisms [4] both being introduced. The former assumes that lattice relaxation is obtained by the bending over of threading dislocations, propagating into an epitaxial layer from the substrate, to produce misfit dislocations in the interfacial plane. In such a process the substrate dislocation density is preserved in the layer if the dislocations bend out of the interfacial plane and thread through the epilayer. The half-loop mechanism however considers the nucleation of a dislocation loop at the layer surface, which glides to the interface giving two threading dislocations linked by a misfit segment. Thus for each interfacial misfit segment two threading dislocations are introduced and hence the epilayer contains an increased dislocation density compared to that in its substrate. From the observation in this work of a higher background density in epitaxial $Cd_{0.24}Hg_{0.76}Te$ compared to that in both CdTe and $Cd_{0.96}Zn_{0.04}Te$ substrates, it is implicit that lattice relaxation is at least partly accounted for by the half-loop mechanism (in the absence of any other relaxation or multiplication mechanism). The increase in the dislocation density in thick epilayers is contrary to the commonly reported result of an identical dislocation density in thick layers of LPE (Cd,Hg)Te and their corresponding CdTe or (Cd,Zn)Te substrate [5-9]. It is of note however that the majority of these results are for substrates containing a dislocation density of $>10^5$ cm^{-2}, i.e higher than that in substrates used in this work. If there are sufficient dislocations, threading from the substrate into the layer, to relieve all the misfit strain, the need for the formation of half-loops is removed, and the layer dislocation density will shadow the dislocation

density in the substrate. Thus it is possible in the case of epitaxial growth on poorer quality substrates that the epilayer dislocation density will match the substrate dislocation density. Hence a critical substrate dislocation density may exist. For substrate dislocation densities above this value there are sufficient dislocations to remove all the misfit strain and hence the dislocation density in the layer is comparable to the substrate density. Below the critical value however, dislocation half-loops are required and the 'background' dislocation density in the layer exceeds the substrate dislocation density.

The difference in background dislocation density, for layers grown on $Cd_{0.96}Zn_{0.04}Te$ and CdTe substrates having the same dislocation densities, may be accounted for by the increase in lattice mismatch. For example the misfit in the $Cd_{0.24}Hg_{0.76}Te$ / $Cd_{0.96}Zn_{0.04}Te$ system is <0.01% whereas the mismatch in the $Cd_{0.24}Hg_{0.76}Te$ / CdTe system is 0.3%. If it is assumed that not all the misfit strain is relieved by threading (substrate) dislocations then a greater number of dislocation half-loops are likely to be required in $Cd_{0.24}Hg_{0.76}Te$ / CdTe epilayers compared to $Cd_{0.24}Hg_{0.76}Te$ / $Cd_{0.96}Zn_{0.04}Te$, therefore accounting for the higher dislocation density revealed in this work. The higher misfit in the $Cd_{0.24}Hg_{0.76}Te$ / CdTe system also accounts for the higher interface (misfit) dislocation density of 1×10^7 cm^{-2} shown in figure 7.1 compared to the maximum dislocation density of 1×10^6 cm^{-2} for a similar layer grown on $Cd_{0.96}Zn_{0.04}Te$ shown in figure 7.3. It may be therefore concluded that the density of threading dislocations in the layers examined in this work is determined by the lattice mismatch, rather than the substrate dislocation density. This is contrary to the result reported by Yoshikawa [5], who concludes that the threading dislocation density is independent of the magnitude of the mismatch and proportional to the substrate dislocation density. More extensive work on substrates with low dislocation densities would be desirable in order to confirm these findings.

In Table 7.1 the mosaic tilt in $Cd_{0.24}Hg_{0.76}Te$ / CdTe is shown to be greater than that of $Cd_{0.24}Hg_{0.76}Te$ / $Cd_{0.96}Zn_{0.04}Te$, for comparable layer thicknesses. Furthermore the tilt FWHM for thick layers (i.e in the background dislocation density region) in both systems is larger than that in the corresponding substrate. These X-ray results are qualitatively confirmed by the EBIC micrographs in figures 7.9 and 7.10. Both micrographs show a 5μm thick $Cd_{0.24}Hg_{0.76}Te$ film however a sub-grain network of smaller cells is visible in the layer grown on CdTe compared with that grown on $Cd_{0.96}Zn_{0.04}Te$. This observation is a result of the greater misfit and hence increased threading dislocation density previously discussed in the

$Cd_{0.24}Hg_{0.76}Te$ / CdTe system. In figures 7.9 and 7.10 average cell sizes of 30μm and 75μm are visible for layers grown on CdTe and $Cd_{0.96}Zn_{0.04}Te$ respectively. These values are smaller than the cell sizes observed in the corresponding substrates (i.e 60μm and 150μm, in section 6.2.1) thus indicating the formation of a tighter sub-grain network and therefore an increased mosaic tilt in epitaxial (Cd,Hg)Te. Tilts in epitaxial layers have been analysed by Durose [10], and for the CdTe / GaAs system an increase in the epilayer tilt over that already present in the substrates is shown to be due to the partial cooperative alignment of interfacial dislocation components.

The elongated nature of the triple axis reciprocal space maps shown in figures 7.6 and 7.7, clearly show the higher contribution of tilt to the total (i.e double crystal) rocking curve FWHM measured in the epitaxial layers, compared to the contribution from lattice dilation. This is confirmed quantitatively by the values given in Table 7.1, e.g for a 12μm thickness in $Cd_{0.24}Hg_{0.76}Te$ / $Cd_{0.96}Zn_{0.04}Te$ (with a double crystal rocking curve width of 35 arcseconds) the tilt FWHM is 29 arcseconds compared to the lattice dilation FWHM of 12 arcseconds. The size of the lattice dilation in (Cd,Hg)Te gives an indication of the compositional uniformity in the epilayers. For (Cd,Hg)Te layers grown on both substrates the compositional uniformity in the X-ray sampling depth (~1μm) is greater by about 1 arsecond at distances of less than ~ 5μm from the interface compared with that for thicker layers. This can also be seen by the greater elongation in the ΔQ_z axis of figure 7.7b compared to figure 7.7a. (However in comparing these figures it should be noticed that the scale and contour values used are different.) To characterise this effect more fully however, a larger number of differing layer thicknesses are required.

The defect etching and X-ray results presented in this chapter both indicate a fall in dislocation density with increasing film thickness (see figures 7.1, 7.3 and Table 7.1), although only the etching results reveal that this decrease in confined to layer thicknesses of ≤ 5-6μm. The observation of a constant background dislocation density for larger layer thicknesses is consistent with TEM [6] and etching results reported elsewhere [5]. In section 2.3.2.1 the Durose and Tatsuoka [11] model, which predicts the lowering of dislocation densities in epitaxial films as a function of increasing thickness, was described. In this phenomenological model sufficient threading dislocations are invoked as is necessary to remove the residual strain in an epilayer. The dislocation density decreases with increasing depth as threading dislocations annihilate one another and the model predicts a relationship of the form;

ln (D(h) - D(∞)) ∝ layer thickness , where D(h) is the dislocation density at a film thickness h and D(∞) is the dislocation density at an infinite thickness, i.e the background dislocation density. The graph of the dislocation density variation in a $Cd_{0.24}Hg_{0.76}Te$ / CdTe layer, i.e figure 7.1, is replotted using this strain relief model in figure 7.11. The data points in figure 7.11 show a strongly linear relationship and hence indicate a good fit to the Durose and Tatsuoka model. The intercept gives the interfacial dislocation density, and from figure 7.11 this may be calculated to be 1.5×10^7 cm^{-2}.

The data in figure 7.1 was also replotted using Ayers (half-loop) model [12] (section 2.3.2.1), which predicts a relationship of the form; dislocation density ∝ thickness $^{-1}$. A replot of the data in figure 7.1 on such axes is shown in figure 7.12. Whereas in figure 7.11 the data shows an excellent fit to the Durose and Tatsuoka model, the agreement between the data in figure 7.12 and the linear plot predicted by the Ayers model is less convincing. The Ayers model however assumes a highly mismatched system, therefore the low mismatch in the systems examined in this work may account for this discrepancy. Also the model is not expected to be linear for thin layers [12] and has been found to account poorly for the observation of constant dislocation densities in thick layers [11].

On comparison of the etch pit density variations shown in figures 7.1 and 7.3 it is apparent that whereas the peak dislocation density in the $Cd_{0.24}Hg_{0.76}Te$ / CdTe system is located at the chemical interface, the peak dislocation density in the $Cd_{0.24}Hg_{0.76}Te$ / $Cd_{0.96}Zn_{0.04}Te$ system lies ~0.6μm within the layer. This displacement is also clearly shown in figure 7.5. The movement of misfit dislocations from the chemical interface has been reviewed by Matthews [13]. Nouruzi - Khorasani et al [6] describe the movement of the misfit dislocations as the resultant of two forces. The first of these is misfit strain, which occurs if the misfit dislocations do not take up all the strain in the system. In this case, in the early stages of diffusion (of material across the interface) where the diffusion distance is less than the epilayer thickness, the force will always be in such a direction as to make the dislocations move away from the interface and into the substrate. The second force is due to the Kirkendall effect. This effect refers to the climb force exerted on misfit dislocations by the vacancy excess induced by the non-equilibrium diffusion of species across a boundary. At a $Cd_{0.24}Hg_{0.76}Te$ / CdTe (or $Cd_{0.96}Zn_{0.04}Te$) interface, the extra half plane of atoms at a 60° dislocation lies within the (Cd,Hg)Te thus the vacancy excess induced pushes the

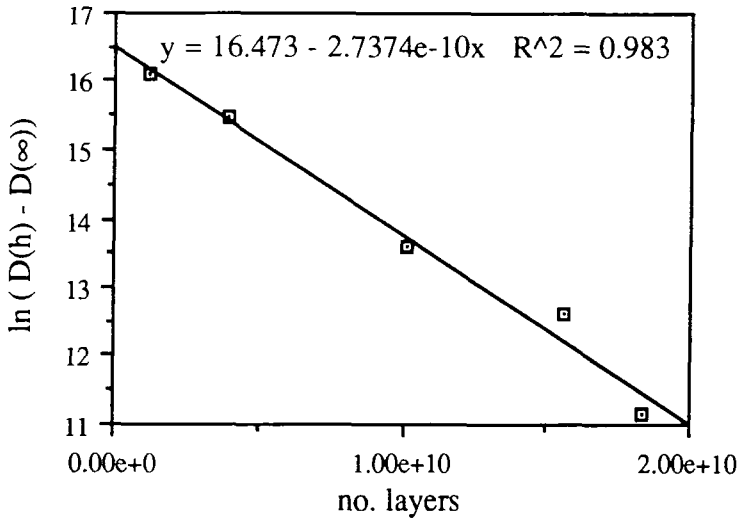

Figure 7.11 Dislocation density variation in $Cd_{0.24}Hg_{0.76}Te$ / CdTe plotted using the Durose strain relief model [11].

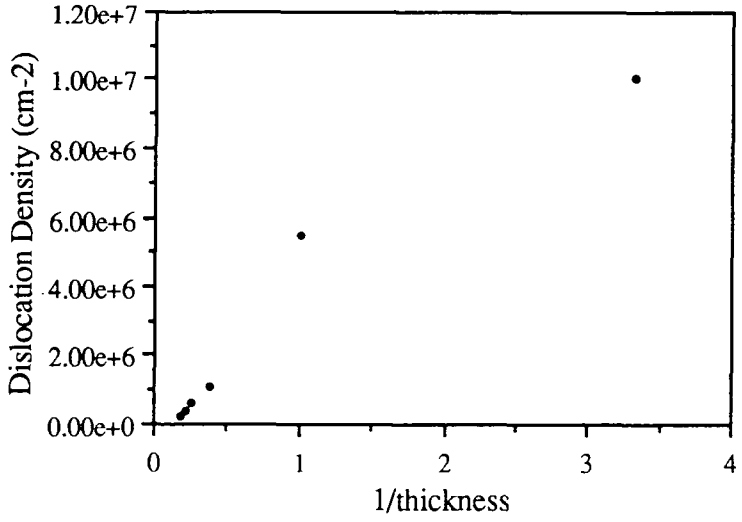

Figure 7.12 Dislocation density variation in $Cd_{0.24}Hg_{0.76}Te$ / CdTe plotted using the Ayers half loop model [12].

misfit dislocations into the epilayer. The lattice misfit in $Cd_{0.24}Hg_{0.76}Te$ / CdTe is larger than that in $Cd_{0.24}Hg_{0.76}Te$ / $Cd_{0.96}Zn_{0.04}Te$ and thus the misfit strain is likely to be greater in the former. Therefore at the $Cd_{0.24}Hg_{0.76}Te$ / CdTe interface the misfit strain and Kirkendall effect are likely to cancel out with the result that there is no net displacement of the misfit dislocations, however in the $Cd_{0.24}Hg_{0.76}Te$ / $Cd_{0.96}Zn_{0.04}Te$ system the Kirkendall effect is likely to be dominant and hence the misfit dislocations are forced into the layer.

7.6 Conclusions

From both defect etching and triple axis X-ray analysis of LPE (Cd,Hg)Te the threading dislocation density in LPE (Cd,Hg)Te has been shown to decrease with increasing epilayer thickness. However for layer thicknesses of $\geq 5\mu m$ a constant, or 'background' dislocation density is achieved. The observation of a higher value for this background dislocation density in $Cd_{0.24}Hg_{0.76}Te$ epilayers (i.e $> 9 \times 10^4$ cm $^{-2}$) compared with both CdTe and $Cd_{0.96}Zn_{0.04}Te$ substrates ($\sim 3 \times 10^4$ cm^{-2}) indicates that the lattice relaxation in the layer may not be entirely achieved by the bending over of threading substrate dislocations (i.e the Matthews-Blakeslee model). Instead the relaxation of the layers must at least partly be accounted for by the formation of dislocation half-loops. Therefore it may be concluded that for LPE growth on high quality substrates with a low dislocation density ($< 5 \times 10^4$ cm^{-2}) there are insufficient substrate dislocations to relieve the misfit strain and therefore the substrate dislocation density is not preserved in the layer. These results are contrary to the widely reported result in the literature that the dislocation density in thick LPE (Cd,Hg)Te shadows the substrate dislocation density. These results however were generally based on substrates with a dislocation density of $> 10^5$ cm^{-2} (i.e higher than that of the substrates used in this work). This contradiction may be therefore accounted for by the existence of a critical substrate dislocation density. For substrates with a dislocation density above this value, sufficient dislocations thread from the substrate to relieve all the misfit strain in the layers and hence the substrate dislocation density is preserved. For substrates with a dislocation density below the critical value however, the formation of dislocation half-loops is also required and hence an increased background dislocation density results in the epilayers. Other relaxation mechanisms and dislocation multiplication mechanisms have not been considered here.

The lower etch pit density in $Cd_{0.24}Hg_{0.76}Te$ / $Cd_{0.96}Zn_{0.04}Te$ (9×10^4 cm^{-2}) compared to $Cd_{0.24}Hg_{0.76}Te$ / CdTe (3×10^5 cm^{-2}), for similar substrate

dislocation densities, and the reduction in tilt and total rocking curve FWHM values indicates the influence of a lower misfit. The misfit in the former is 0.01% whereas the lattice misfit in the latter is 0.3%. Hence the background dislocation density in the $Cd_{0.24}Hg_{0.76}Te$ epilayers examined in this work would appear to be dependent on the lattice mismatch as well as the substrate dislocation density.

The increased tilt FWHM in epitaxial (Cd,Hg)Te and the observation of a tighter sub-grain network in EBIC micrographs, compared to similar observations in the corresponding CdTe and $Cd_{0.96}Zn_{0.04}Te$ substrates indicate a higher mosaic tilt in the layers. This increase in epilayer tilt may be accounted for by the presence of dislocations.

The elongation of triple axis reciprocal space maps in the tilt axis for large epilayer thicknesses, compared to the small elongation in the dilation axis, indicates the low contribution of lattice dilation to the total (or double crystal) rocking curve width. This is shown quantitatively by the low (e.g 12 arcseconds) lattice dilation FWHM.

The fall in etch pit density with increasing film thickness in the $Cd_{0.24}Hg_{0.76}Te$ / CdTe examined, shows an excellent fit to that predicted by the Durose strain relief model [11]. The dislocation densities measured decreased with increasing layer thickness presumably until the residual strain was eliminated. It is therefore likely that this model is more appropriate to the (small lattice mismatched) (Cd,Hg)Te / CdTe system than the Ayers model [12] which requires a continuing decrease in dislocation density with increasing thickness. The Ayers model assumes a large lattice mismatch, and the experimental results obtained in this work showed only an approximate fit to this half-loop theory.

Examination of the variation in dislocation density with layer thickness in $Cd_{0.24}Hg_{0.76}Te$ / $Cd_{0.96}Zn_{0.04}Te$ revealed the peak dislocation density to be displaced ~0.6μm into the layer. This is contrary to the situation in layers grown on CdTe, in which case the maximum dislocation density was observed at the interface. Such a displacement is assumed to be a consequence of the opposing forces induced on misfit dislocations by the presence of both misfit strain and the Kirkendall (dislocation climb) effect. In the $Cd_{0.24}Hg_{0.76}Te$ / CdTe system the two cancel out and thus there is no net displacement of the dislocations. However due to the lower misfit in $Cd_{0.24}Hg_{0.76}Te$ / $Cd_{0.96}Zn_{0.04}Te$ the Kirkendall effect is dominant and hence the misfit dislocations are forced into the layer.

REFERENCES FOR CHAPTER SEVEN

1. I. Hähnert and M. Schenk, J. Crystal growth **101** (1990) 251.
2. P. Gay, P.B. Hirsch and A. Kelly, Acta. Metallurgica **1** (1953) 315.
3. J.W. Matthews and A.E. Blakeslee, J. Crystal Growth **27** (1974) 118.
4. E.A. Fitzgerald, G.P. Watson, R.E. Proano, D.G. Ast, P.D. Kirchener, G.D. Pettit and J.M. Woodall, J. Appl. Phys. **65** (1989) 2220.
5. M. Yoshikawa, J. Appl. Phys. **63** (1987) 1533.
6. A. Nouruzi-Khorasani, I.P. Jones, P.S. Dobson, D.J. Williams and M.G. Astles, J. Crystal Growth **96** (1989) 348.
7 S. Bernardi, C. Bocchi, C. Ferrari, P. Franzosi and L. Lazzarini, J. Crystal Growth **113** (1991) 53.
8. H. Takigawa, M. Yoshikawa and T. Maekawa, J. Crystal Growth **86** (1988) 446.
9. D. Chandra, J.H. Tregilgas and M.W. Goodwin, J. Vac. Sci. Technol. **B9** (1991) 1852.
10. K. Durose, A. Turnbull and P.D. Brown, Mats.Sci. Eng. **B**16 (1993) 96.
11. K. Durose and H. Tatsuoka, in : Microscopy of Semiconducting Materials 1993, Inst. Phys. Conf. Ser., in press.
12. J.E. Ayers, L.J. Schowalter and S.K. Ghandhi, Mat. Res. Soc. Symp. Proc. **220** (1991) 661.
13. J.W. Matthews (Ed.), Epitaxial Growth Part B, (Academic Press, New York, 1975), p.598.

CHAPTER EIGHT

Summary of Conclusions

The aim of this thesis has been to examine the occurrence and nature of structural defects in CdTe, (Cd,Zn)Te and (Cd,Hg)Te and to investigate appropriate characterisation methods. The driving force behind this project being the use of (Cd,Hg)Te as an infra-red detector material. To this end the experimental work presented herein is in three main parts, these being;

1. Validation of the CL microscopy and ferric chloride defect etching techniques for the qualitative and quantitative characterisation of structural defects in bulk CdTe and (Cd,Zn)Te.
2. Comparison of structural defect content in substrates cut from boules of ACRT CdTe and non-ACRT CdTe and $Cd_{0.96}Zn_{0.04}Te$.
3. Investigation of the influence of substrate quality and type on LPE (Cd,Hg)Te film quality.

Cathodoluminescence microscopy has been shown in chapter 4 to be an excellent technique for the observation of extended defects in boules of CdTe and (Cd,Zn)Te. It provides a non destructive technique without the requirement of fabricating contacts (c.f EBIC) and defines electrically active defects as areas of non-radiative (dark) contrast. By correlation with defect etching CL features representing dislocations, sub-grain and twin boundaries and precipitates have been identified. This work also establishes the technique of CL temperature dependent contrast.

By comparing the temperature dependence of the contrast representing precipitates and dislocations, the qualitatively similar contrast of these two types of defect (i.e localised dark spots) has been quantitatively distinguished. All the precipitates examined showed high contrast at low temperatures (up to 150K) which decreased with increasing sample temperature. At all the dislocations examined however, the contrast increased from a low value (at low temperatures), reached a peak (in the region of 150K) before finally decreasing. The high contrast (at low temperatures) at Te precipitates has been accounted for by considering these defects to have an infinite recombination velocity (and hence an infinite recombination strength) [1] and by also considering their occupation of a fraction of the generation volume. The

variation in the CL contrast at these defects with increasing temperature remains unclear however it may be accounted for by both an increase in the minority carrier diffusion length and a decrease in the CdTe / Te (interface) barrier height. The temperature dependence of the dislocation contrast is consistent with the variation in EBIC contrast at dislocations in Si, modelled theoretically (and observed experimentally), by Wilshaw et al [2]. The Wilshaw model is based on the band bending induced at dislocation cores in semiconductors. However from the results presented in this work the validity of the Wilshaw model to the CL contrast at dislocations in CdTe remains unproven.

In order to gain a thorough understanding of the CL recombination process in CdTe more reproducible graphs of the temperature dependent contrast are required. Furthermore in order to determine the validity of the Wilshaw EBIC contrast model for CL the beam current contrast dependence would also be valuable and the temperature dependence of physical parameters in the recombination process (e.g the minority carrier recombination length) are also needed. Firstly however, to ensure the Wilshaw model is applicable to CdTe, the temperature dependent EBIC contrast at dislocations in CdTe requires examination. A more complete set of experimental results however was unobtainable due to serious equipment failure.

The ability of an aqueous ferric chloride solution to reproducibly develop etch pits on the $(\bar{1}\bar{1}\bar{1})$B surface of CdTe [3] is of special technological importance. Few etching solutions are reported to develop pits on this LPE growth surface, and none have had their action on this surface correlated with complementary characterisation techniques. From correlations (in chapter 5) with both CL and IR microscopy, ferric chloride etching has been shown to be capable of revealing individual twins, dislocations and precipitates on $(\bar{1}\bar{1}\bar{1})$B CdTe and (Cd,Zn)Te. The etchant was also observed to reliably develop pits on (111)A, {110}, {511}, {5 7 13} and polycrystalline CdTe. Comparisons between ferric chloride etching and CL microscopy results, indicate the former to have the greater resolution whereas the latter reveals a greater number of defects. Such a result is expected due to the penetration of the electron beam in the CL technique and its intrinsic resolution. The etch was also found to be effective on $(\bar{1}\bar{1}\bar{1})$B (Cd,Hg)Te which enables the simultaneous measurement of dislocation densities in both an epilayer and its substrate. The etching solution has a background etch rate of ~2μm min^{-1} on both $(\bar{1}\bar{1}\bar{1})$B CdTe and $Cd_{0.96}Zn_{0.04}Te$ which also enables the profiling of defects and the calculation of volume defect densities.

In chapter 6, by use of CL microscopy, ferric chloride defect etching and other characterisation techniques, such as triple axis X-ray diffraction and IR microscopy, the structural quality of boules of Bridgman grown ACRT CdTe [4] has been compared with boules of non-ACRT CdTe (grown under similar growth conditions) and boules of non-ACRT $Cd_{0.96}Zn_{0.04}Te$ (grown under a Cd overpressure). Comparisons between boules of ACRT and non-ACRT CdTe indicated a lower dislocation and precipitate density in the former. The ACRT material also had a better crystallinity, which was revealed by the observation of larger sub-grain cells in CL micrographs and by a lower mosaic tilt. A similar comparison between ACRT CdTe and non-ACRT $Cd_{0.96}Zn_{0.04}Te$ revealed a comparable dislocation density and a significantly lower precipitate density in the CdTe. The similarity in the dislocation densities in ACRT CdTe and (non-ACRT) $Cd_{0.96}Zn_{0.04}Te$ is testimony to the effectiveness of the ACRT growth method. Bridgman growth of CdTe without the ACRT modification typically results in a dislocation density higher than that in boules of $Cd_{0.96}Zn_{0.04}Te$ [4,5], and this is also shown in chapter 6. The lowering of the dislocation density in ACRT boules is likely to be a result of the enhanced stirring reducing the temperature gradient in the growing crystal, which lowers the dislocation density arising from thermal stress. By inhibiting the formation of Te droplets, the reduction of the precipitate density (on solidification) in ACRT CdTe, is also thought to be a result of the enhanced stirring in the ACRT growth process.

Although both the ACRT CdTe and non-ACRT (Cd,Zn)Te boules examined contained a similar dislocation density, the CdTe crystals contained a more fully developed sub-grain structure. This was revealed by both a higher density of dislocations in sub-grain boundaries in CL micrographs, and a higher (tilt) X-ray rocking curve FWHM (i.e 25 arcseconds in ACRT CdTe compared with 8 arcseconds for $Cd_{0.96}Zn_{0.04}Te$). The less defined sub-grain structure in (Cd,Zn)Te boules is thought to be a result of solution hardening, i.e the incorporation of 4% Zn into the lattice inhibits the motion of dislocations and increases the critical resolved shear stress. From the elongation of triple axis reciprocal space maps in the ΔQ_y (tilt) axis and the subsequent measurement of low lattice dilation rocking curves widths in both $Cd_{0.96}Zn_{0.04}Te$ and ACRT CdTe, the stoichiometric inhomogenity in both materials is seen to be small.

In boules of ACRT CdTe grown from a 0.5% Cd excess dislocation rosettes have been observed by CL and ferric chloride etching. These rosettes are consistent with punch out dislocations observed when CdTe is stressed by a micro-indentor. By

the growth temperature) induces a tensile stress in the CdTe lattice close to that at which the spontaneous nucleation of dislocations is theoretically predicted. The presence of Cd inclusions at the centre of such rosettes is confirmed by EDAX.

Boules of CdTe grown from the vapour phase by the 'Durham' technique showed an equilibriated defect distribution. CL microscopy revealed a close packed sub-grain network, containing cells with an average size of ~30μm and the dislocations forming the boundaries being unresolvable. This indicates a dislocation separation of ≤ 1μm in the boundaries, from which a sub-grain misorientation of 3'-30' has previously been calculated [6]. As a comparison the dislocation separation in sub-grain boundaries in the ACRT CdTe and the (Cd,Zn)Te boules examined in this work were 5 μm and 15 μm respectively. Te precipitates in the vapour material were typically 20 -30 μm in size and invariably located on twin boundaries. The Te precipitate size in melt grown material was <10μm. Despite the poorer crystal quality of vapour grown CdTe, compared with melt grown material, revealed in this work vapour growth is remains attractive due to its lower growth temperature. The critical resolved shear stress of a material decreases with increasing temperature hence growth at lower temperatures may inhibit the nucleation of dislocations [7].

Defect etching and triple axis X-ray diffraction have been used in chapter 7 to examine the structural quality of LPE (Cd,Hg)Te, grown on CdTe and $Cd_{0.96}Zn_{0.04}Te$ substrates, as a function of layer thickness. Both techniques show a decrease in the threading dislocation density with increasing thickness up to ~5-6μm, after which a constant background dislocation density is obtained. The decrease in the dislocation density with increasing layer thickness in the $Cd_{0.24}Hg_{0.76}Te$ / CdTe system shows an excellent fit to the decrease predicted by the Durose strain relief model [8]. This model is able to account for the constant dislocation density observed in thick layers by assuming that at these thicknesses all the residual strain in the layer has been removed. The Ayers model however requires a falling dislocation density for all thicknesses and hence the same results show a poorer agreement when plotted using the Ayers half-loop theory [9] . Hence for CdTe / (Cd,Hg)Te epitaxial systems the strain relief model would appear to be more applicable for predicting the functional depth dependence of the dislocation density.

The displacement of the peak dislocation density into the layer in $Cd_{0.24}Hg_{0.76}Te$ / $Cd_{0.96}Zn_{0.04}Te$ has been accounted for by considering the relative sizes of the forces induced on misfit dislocations by both the misfit strain and the Kirkendall

forces induced on misfit dislocations by both the misfit strain and the Kirkendall effect. The Kirkendall effect is the climb force exerted on misfit dislocations by the vacancy excess induced by the non-equilibrium diffusion of species across a boundary. For growth on nearly latticed matched $Cd_{0.96}Zn_{0.04}Te$ the Kirkendall effect is dominant and hence the misfit dislocations are forced into the layer. However, for growth on CdTe the two forces cancel out and hence the peak dislocation density is observed at the interface.

Comparisons made between films of $Cd_{0.24}Hg_{0.76}Te$ grown on CdTe and $Cd_{0.96}Zn_{0.04}Te$ substrates, both containing a similar dislocation density, have indicated a lower background dislocation density in epilayers grown on the latter. Furthermore epitaxial growth on both materials results in a background layer dislocation density higher than that in the corresponding substrate. The lower dislocation density in $Cd_{0.24}Hg_{0.76}Te$ / $Cd_{0.96}Zn_{0.04}Te$ compared to $Cd_{0.24}Hg_{0.76}Te$ / CdTe indicates the influence of a lower misfit, and hence the dislocation density in these layers is seen to be dependent on the lattice mismatch as well as the substrate dislocation density. The observation of a higher dislocation density in the epilayers compared with both CdTe and $Cd_{0.96}Zn_{0.04}Te$ substrates indicates that relaxation takes place at least partly by the formation of dislocation half-loops within these layers. It may be therefore concluded that for LPE growth on substrates examined in this work, with dislocation densities $< 5 \times 10^4$ cm^{-2}, there are insufficient substrate dislocations to relieve all the misfit strain in the epilayers via the Matthews-Blakeslee mechanism [10]. For LPE growth on substrates with higher dislocation densities than those used in this work the epilayer dislocation density has been reported to match that in the substrate [11], and this indicates the possibility of the existence of a critical substrate dislocation density. At or above this critical value, there are sufficient substrate dislocations to relieve the misfit strain and hence the layer dislocation density shadows the substrate density. However for substrate dislocation densities below this value, the requirement of the formation of dislocation half-loops leads to an increase in the corresponding layer dislocation density.

In summary, although CdTe substrates of comparable structural quality to (Cd,Zn)Te may be grown, (as shown in chapter 6), the highest quality LPE (Cd,Hg)Te layers are grown on lattice matched $Cd_{0.96}Zn_{0.04}Te$. The observation of a dependence in the epilayer dislocation density on misfit and the dominance of half-loop relaxation when the substrate dislocation density is low, leads to the conclusion that a lowering of the misfit and strain induced during growth is equally

important as the lowering of the substrate dislocation density, in the reduction of the dislocation density in LPE (Cd,Hg)Te.

REFERENCES FOR CHAPTER EIGHT

1. C.C.R. Watson and K. Durose, J. Crystal Growth **126** (1993) 325.
2. see for example : P.R. Wilshaw, T.S. Fell and G.R. Booker, in : 'Point and Extended Defects in Semiconductors', (Eds.) G. Benedek, A. Cavallini and W. Schroter (Plenum, New York, 1989), p. 243.
3. C.C.R. Watson, K. Durose, A.J. Banister , E. O'Keefe and S.K. Bains, Mat. Sci. Eng. **B16** (1993) 113.
4. P. Capper, J.E. Harris, E. O'Keefe, C.L. Jones, C.K. Ard, P. Mackett and D. Dutton, Mats. Sci. Eng. **B16** (1993) 29.
5. C.J. Johnson, SPIE **1106** (1989) 56.
6. K. Durose, Ph.D Thesis, University of Durham, 1986.
7. K. Durose, A. Turnbull and P.B. Brown, Mats. Sci. Eng. **B16** (1993) 96.
8. K. Duose and H. Tatsuoka, in : Microscopy of Semiconducting Materials 1993, Inst. Phys. Conf. Ser., in press.
9. J.E. Ayers, L.J. Schowalter and S.K. Ghandhi, Mat. Res. Soc. Symp. Proc. **220** (1991) 661.
10. J.W. Matthews and A.E. Blakeslee, J. Crystal Growth **27** (1974) 118.
11. M. Yoshikawa, J. Appl. Phys. **63** (1987) 1533.